ESCUELA POLITÉCNICA NACIONAL

FACULTAD DE INGENIERÍA MECÁNICA

TECHNO ECONOMIC ASSESSMENT OF UNMANNED AEROSPACE PLATFORMS FOR ENVIRONMENTAL MONITORING WITH A VISUAL SPECTRUM CAMERA

TRABAJO DE TITULACIÓN PREVIO A LA OBTENCIÓN DEL TÍTULO DE MAGISTER EN DISEÑO y SIMULACIÓN

VERA HENSIEK DANIEL JAVIER

daniel.verah@epn.edu.ec

DIRECTOR: Ing. Valencia, Esteban, PhD

esteban.valecia@epn.edu.ec

CO-DIRECTOR: López, Ericson, PhD

ericsson.lopez@epn.edu.ec

15 junio, 2020

CERTIFICACIÓN

Certifico que el presente trabajo fue desarrollado por el **ING. DANIEL JAVIER VERA HENSIEK**, bajo nuestra supervisión.

_____

Esteban Valencia, PhD

DIRECTOR DE PROYECTO

_____

Ericson López. PhD

CODIRECTOR DE PROYECTO

DECLARACIÓN

Yo, **Daniel Javier Vera Hensiek**, declaro bajo juramento que el trabajo aquí descrito es de mi autoría; que no ha sido previamente presentado para ningún grado o calificación profesional; y, que he consultado las referencias bibliográficas que se incluyen en este documento.

A través de la presente declaración cedo mis derechos de propiedad intelectual correspondiente a este trabajo, a la Escuela Politécnica Nacional, según lo establecido por la Ley de Propiedad Intelectual, por su Reglamento y por la normativa institucional vigente.

_____

Autor

DEDICATORIA

A mi amada esposa, Vanessa por su apoyo incondicional. A mi hija Amelia que vino al mundo iniciando la maestría y a mi hija Antonia que nació durante su culminación.

AGRADECIMIENTO

Agradezco a mi esposa y mis hijas por estar conmigo durante esta etapa de mi vida. A mi papá y mamá por darme apoyo moral. A todos los profesores que me entregaron parte de su sabiduría, experiencia y conocimiento. Al grupo de investigación ATA, en especial Darío y al grupo de investigación del OAQ por brindarme apoyo para el desarrollo de esta tesis. Y a todos los profesores y compañeros que fueron parte de esta experiencia.

INDEX

LIST OF FIGURES

LIST OF TABLES

GLOSSARY AND SYMBOLS

GLOSARY (in apathetical order)

ACQ	Acquisition cost
ADCS	Attitude Determination and Control
AMPR	Aeronautical manufacturers planning report
asl	Above sea level
ASTRA	Atmospheric Science Through Robotic Aircraft
ATA	Aerodynamic and Applied Thermo-fluids Group
CCD	Charge-coupled device
CMOS	Active-pixel sensor
COESA	Committee on Extension to the Standard Atmosphere
COMS	Communication System
COTS	Commercial of the shelf
C&DH	Command and Data Handling (C&DH)
CUSF	Cambridge University Space Flight
DISP	Disposal cost
ECI	Earth centered inertial reference system
EPS	Expanded Polystyrene / Electric Power System
FOV	Field of view
GMAT	General Mission Analysis tool
GSO	Geosynchronous orbit
GUI	Graphical user interface
HEO	Highly elliptical orbit
HWM	Horizontal Wind Model
ISS	International space station
JEM	Japanese Experimental Module
JPL	Jet propulsion laboratory
J-SSOD	JEM small satellite deployer
LCC	Life cycle cost
LEO	Low Earth orbit
LLT	Lifting line theory
MEO	Medium Earth orbit
NASA	Nacional Aeronautics and Space Administration
OAQ	Observatorio Astronómico de Quito
OPS	Operational cost
PL	Payload
PLA	Polylactic acid thermo-plastic polyester

RGB	Red-green-blue
RDTE	Research, development, test and evaluation cost
SNMB	National Forest Monitoring System
SRP	Solar Radiation Pressure
SSM	Specific Site Management
STK	Satellite tool kit
S&M	Structure and Mechanisms
TAI	International atomic time
TEA	Techno economic analysis
ThC	Thermal Control
UAS	Unmanned Aerial System
UTC	Coordinated Universal time

Symbols

Optical system and RGB camera

D_A	Aperture diameter	[mm]
f_e	Effective focal length	[mm]
d_{object}	Object distance	[m]
d_{image}	Image distance	[mm]
M_F	Image magnification factor	-
Ω_{FOV}	Solid angle FOV	[sr / degrees^2]
θ_x	Along track FOV	[rad / degrees]
θ_y	Across track FOV	[rad / degrees]
x	Detector x dimension	[mm]
y	Detector y dimension	[mm]
IFOV	Instantaneous field of view	[m^2]
X	IFOV x dimension	[m]
Y	IFOV y dimension	[m]
GSD	Ground sample distance	[rad]
m	Number of pixels in the x dimension	[#]
n	Number of pixels in the y dimension	[#]
Ω_{pixel}	FOV of an individual pixel	[sr / degrees^2]
$IFOV_{pixel}$	IFOV of an individual pixel	[m]
θ_{min}	Object´s minimum angular separation	[rad]
λ	Signal´s wavelength	[nm]
R_{frame}	Frame rate	[fps]

T_{sample}	Sample time	[s]
T_{int}	Integration time	[s]
C_{duty}	Duty cycle	-
S	Signal	[N/A]
N	Noise	[N/A]
S_F	Signal factor	-

Weather balloon

M_N	Mach number	-
M_{total}	Total mass of the balloon system	[kg]
F	Force	[N]
W	Weight	[N]
g_o	Gravitational acceleration constant	[m/s^2]
C_D	Drag Coefficient	-
ρ	Density	[kg/m^3]
M_L	Lifting mass control variable	[kg]
B	Buoyancy factor	-
acc	Acceleration	[m/s^2]
A_{bal}	Area of the balloon system	[m^2]
Vol	Volume of the balloon	[m^3]
Err	Lifting factor error	-
Ve	Velocity	[m/s]
d	Distance	[m]

Sub index (weather balloon)

i	Time index identifier
o	Sea level
*a*ir	Air
h	Helium
L	Lift
D	Drag
V	Vertical plane
H	Horizontal plane

Nanosatellite

G	Gravitational constant (6.67×10^{-11})	[Nm^2kg^{-2}]
M	bigger mass	[kg]
m	smaller mass	[kg]

r	distance from the center of the earth to orbiting mass	[km]
p	parameter of semi-latus rectum	[km
e	eccentricity	-
a	semi-mayor axis	[km]
μ	gravitational parameter	[m^3/s^{-2}]
i	Inclination	[degrees]
Ω	Right ascension	[degrees]
ω	Argument of periapsis	[degrees]
θ	True anomaly	[degrees]

Fixed Wing UAV

W/S	Wing loading	[N/m^2]
W/P	Weight to power ratio	[N/W]
C_L	Lift Coefficient	-
C_D	Drag Coefficient	-
S	Planform area	[m^2]
b	span	[m]
D_f	Maximum fuselage diameter	[m]
AR	Aspect ratio	-
V	speed	[m/s]
l_o	tail arm	[m]
mac	mean aerodynamic cord	[m]
V_H	horizontal tail volume coefficient	-
V_V	Vertical tail volume coefficient	-
C_{m_α}	Static longitudinal stability	[1/rad]
C_{L_α}	Lift slope	[1/rad]
h	non-dimensional locations of the gravity center	-
h_o	non-dimensional locations of the aerodynamic center	-
η_h	Tail efficiency	-
C_{l_α}	2D airfoil lift slope	[1/rad]
$C_{D_{ff}}$	Friction drag coefficient	-
C_f	Skin friction coefficient	-
f_{tc}	Thickness to chord form factor	-
f_M	Mach number correction	-
S_{wet}	Wetted area	[m^2]
$C_{d_{min}}$	2D airfoil drag coefficient	-
$C_{D_{of}}$	Zero-lift / parasite drag coefficient	-

λ_{LD}	Fuselage fineness ratio	-
t/c	thickness to chord ratio	-
L_f/D_f	Length to diameter ratio (fuselage)	-
W	weight	[N]
P	Power required	[W]
T	Thrust	[N]
L	Lift	[N]
D	Drag	[N]
λ	Taper ratio	-
$\Lambda_{c/4}$	Sweep angle at 25% chord	[degrees]
η	efficiency	-
ROD	Rate of descent	[m/s]
GS	ground speed	[NM/h]
Kv	Electric motor gain factor constant	[RPM/V]

Sub index (fixed wing UAV)

h	Horizontal tail
v	Vertical tail
f	fuselage
Req	required
stall	Stall speed
Dmin	Minimum drag
c	cruise
p	propeller
m	electric motor
t	total
es	electric system power required
ps	propulsion system power required
P	Payload
TO	take-off

Power and Energy (All)

P	Power	[W]
V_o	Battery voltage	[V]
I	Current	[A; Ah]
L_b	Life of the battery	[s]
Bc	Battery capacity	[mAh]
P_F	Power factor	-

Rad_{X+}	Radiation in the x+ face of the nanosatellite	[W/m^2]
Rad_{Z+}	Radiation in the z+ face of the nanosatellite	[W/m^2]
Rad_{X-}	Radiation in the x- face of the nanosatellite	[W/m^2]
P_{aft}	Total power required by the UAV	[W]
R	UAV rage	[km]
P_{bat}	Battery power	[W]
E	UAV endurance	[s]
$\widehat{P}$	Specific power	[W/kg]

Sub index (power and energy)

Req	Required
t	total

Life cycle cost

C	Cost	[$ (USD)]
MHR	Engineering man hour	[hours]
W_{AMPR}	structure weight ratio to rest of components	[lbs.]
V_{max}	maximum velocity rating (propulsion system)	[knots]
N	number of units	[#]
N_{rr}	production rate (units per month)	[#/month]
F	Weighting factor	-
R	man hour rating	[$/hour]
CEF	normalized cost escalation factor	-
PM	profit margin	-
DOC	direct operational cost	[$ (USD)]
P	cost per unit	[$ (USD)]

Sub index (life cycle cost)

LCC	Life cycle cost
RDTE, r	Research, development, test and evaluation
ACQ, a	Manufacturing and acquisition
OPS	Operation
DISP	Disposal
ed	Engineering and design cost
diff	difficulty of the aerospace system
cad	CAD skill of the people involved
dst	Development, support and testing

tp	Test prototypes
comp	components
man	manufacturing
mat	materials
tool	tooling
qc	quality control
to	test operation
st	static prototypes
tsf_r	test and simulation facilities (RDTE)
tsf	facility adjustment factor
pro	profit
fin	financing
program	units produced during the program
pp	program production cost
p	entire aerospace system program
flt	flight
maint	maintenance
dpr	depreciation
f-t	fees and taxes
unit	initial unit cost
salvage	perceived salvage value and end of life

RESUMEN

El presente documento propone una metodología basada en un análisis tecno económico para seleccionar la plataforma aeroespacial con mejor rendimiento para una misión de monitoreo ambiental usando una cámara de color. Las plataformas en este estudio son: un globo meteorológico diseñado en el proyecto PIS-15-10, un nanosatélite, diseñado para el proyecto PIMI-15-01, y una aeronave de ala fija no tripulada diseñada en el contexto del proyecto PIJ-15-11. Los tres proyectos pertenecen a la Escuela Politécnica Nacional y el trabajo previamente realizado para los mismos se utilizó en la presente tesis. El estudio tecno-económico se basa en cuatro ejes principales; tres que evalúan la parte técnica, siendo estos la autonomía de vuelo, área de operación, y capacidad de carga, mientras que para la parte económica se evalúa el costo de ciclo de vida de la plataforma en el contexto de un programa de un año. Los resultados obtenidos no se alejan mucho de la que la experiencia hubiera propuesto, siendo el avión no tripulado de ala fija la mejor opción para esta labor. Sin embargo, los resultados proponen que cada plataforma tiene sus debilidades y fortalezas. Esto da lugar al origen de una metodología para evaluar el uso de diferentes plataformas aeroespaciales en el contexto de misiones diferentes. Los indicadores presentados en esta tesis permiten una evaluación cuantitativa en el contexto de misiones aeroespaciales, proporcionando de esta manera parámetros medibles, útiles para el diseño preliminar y la selección del vehículo aeroespacial más apropiado.

Palabras clave: análisis tecno-económico**,** globo meteorológico, nanosatélite, avión no tripulado de ala fija, evaluación cuantitativa de plataformas aeroespaciales.

ABSTRACT

This document proposes a methodology based on a techno-economic analysis to select the best performing aerospace platform for an environmental monitoring mission using a color camera. The platforms in this study are: a weather balloon designed in the PIS-15-10 project, a nanosatellite, designed for the PIMI-15-01 project, and an unmanned fixed-wing aircraft designed in the context of the PIJ-15-11 project. The three projects belong to the National Polytechnic School; the work previously completed for them was used in this thesis. The techno-economic study is based on four main indicators; three that evaluate the technical part, these being the flight autonomy, area of operation, and payload capacity, while the economic part is evaluated by considering the life cycle cost of the platform in the context of a one-year program. The results obtained do not deviate much from what experience would have proposed, with the unmanned fixed-wing aircraft being the best option for this task. Nevertheless, the results propose that each platform has its weaknesses and strengths. This is the foundation of a methodology that can be used to evaluate the use of different aerospace platforms in the context of different missions. The indicators presented in this thesis allow a quantitative assessment in the context of aerospace missions, thus providing measurable parameters useful in early design and selection of the most suitable aerospace vehicle.

Keywords: techno-economic analysis, weather balloon, nanosatellite, unmanned fixed-wing aircraft, quantitative assessment of aerospace platforms.

TECHNO ECONOMIC ASSESSMENT OF UNMANNED AEROSPACE PLATFORMS FOR ENVIRONMENTAL MONITORING WITH A VISUAL SPECTRUM CAMERA

INTRODUCTION

It is of public interest the preservation of the environment, conservation of ecosystems, biodiversity, and the integrity of the genetic heritage [1]. Environmental preservation is a complex problem that requires the effort of several public and private actors with different responsibilities, such as monitoring. Monitoring provides the necessary data to assess the base situation and for the creation of emergency action plans. In Ecuador there are some initiatives such as the National Forest Monitoring System, which uses data obtained through satellite images [2], and other private and higher education initiatives that implement copter type unmanned aerial vehicles (UAVs).

The two most common environmental monitoring practices are: on-site with ground tools and remote sensing [3]. Remote sensing requires aerospace platforms to carry the appropriate sensors. Worldwide aerospace technological advancement has resulted in access to low-cost UAVs, which can be adapted to do missions that are different from their original design; resulting in reduced efficiency [3]. With the quadcopter boom, dispersed initiatives have taken place for remote sensing of the environment, obtaining mixed results. However, like satellite images, quadcopters have some limitations, consequently it is important to develop a methodology that allow us to identify the ideal platform according to the monitoring need. The purpose of this work is to develop such methodology by conducting a techno-economic analysis (TEA) using an RGB (red-green-blue) camera as the common payload of three different aerial vehicles: weather balloons, fixed wing UAVs, and nano-satellites. The data obtained with an RGB camera must have the appropriate spatial and temporal resolution to be able to do the pertinent studies [4]. These image parameters depend a lot on the aerospace platform carrying the camera. In this context, the Escuela Politécnica Nacional is involved with three projects that deal with the creation of performance evaluation codes, mathematical models, simulations, and the design of three aerospace platforms. The projects involved are: PIS-15-10, which deals with the design and implementation of weather balloons; PIMI-15-01, whose engineering objective is the design and manufacture of a miniature satellite; and PIJ-15-11 whose purpose is to review the design of fixed-wings UAVs using mathematical codes and models. These

projects have different objectives; nevertheless, they present a great opportunity to do a techno-economic study to compare the three platforms and determine the best alternative for environmental monitoring with an RGB camera.

The TEA is a top view analysis to find environmentally friendly, and economically sustainable processes [5]. Lauer [6], argues that the TEA uses different methods according to the approach and results that are to be obtained; however, there are two components always present: the cost and the benefic. The cost should consider the life cycle of the system, while the benefit looks at the technical characteristics of each platform in the context of environmental monitoring. The TEA study depends a lot on the indicators that are used, so it is important to develop a methodology with the appropriate indicators according to the objectives [7]. Four indicators were identified and form the building block of this study: area of operation, flight autonomy, load capacity, and life cycle cost. The area of operation has a direct impact on the design criteria of each aerospace platform and has direct relationship with the temporal and spatial resolution [4] of the RGB camera. Flight autonomy lets us know how long the aerospace system can stay in flight to perform its main function, this depends mainly on the energy consumption of each platform. The load capacity is a direct indicator of the type of instrument that can be carried, generally a heavier and larger instrument can be related with better performance [8]. Furthermore, it is directly linked to autonomy since increasing the load capacity means reducing it [9]. The life cycle cost is linked to the above technical indicators since an improvement increases the cost regardless of the type of UAV. There are four main components that add up to the life cycle cost of an aerospace system [9]: research, development, and evaluation; acquisition, including manufacturing; operation; and disposal. These indicators form the basis of the methodology here presented that can be applied to future projects in this field.

Research question

Can a tecno-economic assessment of three aerospace platforms used for environmental monitoring evolve into a methodology for selecting the most appropriate platform for this specific mission.

General Objective

Technical and economic analysis of three unmanned aerospace platforms for environmental monitoring with an RGB camera.

Specific objectives

- Create and refine parametric models.
- Develop the figures of merit using the results obtained from the models and the design characteristics of each aerospace platform.
- Develop a methodology to choose the best aerospace platform according to its mission.

Hypothesis

The methodology and the figures of merit developed through this project will enable the evaluation of the feasibility and relevance of different aerospace platforms for a given specific application.

1. THEORETICAL FRAMEWORK

1.1. Environmental monitoring with an RGB camera

This study looks at three different aerospace vehicles with the intention of determining a selection methodology for choosing the best alternative for a given mission: a fixed wing UAV, a weather balloon, and a nano-satellite. These three platforms can be used for remote sensing, which is the central common point for assessment. Furthermore, to help narrow down the method this work will look at the use of a red, green, and blue (RGB) camera for environmental monitoring as the main payload of each platform. An RGB camera operates in the visual spectrum specifically with the red, green, and blue colors. Additionally, it is necessary to point out that there are four main parameters that measure the quality of an image for remote sensing [10]: spatial, spectral, temporal, and radiometric resolution. Spatial resolution refers to the ability to distinguish small adjacent objects in an image [11]. Spectral resolution refers to the wavelengths that the camera can capture. Temporal resolution is the ability to see change over time of the same location [12]. Radiometric resolution is the contrast in intensity between the object of interest and its background [12].

The RGB camera can be defined as a system composed of three main parts: the collector, the detector and the processing module. Each of these components have different performance parameters that provide information about the quality of the data gathered by the camera. The collector refers to the optics, whose function is to gather as much energy as possible and to direct that energy to a detector. The detector is generally a metal-oxide-semiconductor, either a CMOS or CEE sensor that converts that energy to interpretable data [13]. The processing module oversees packaging, storing, and handling the data. For the case of the collector and detector size maters, so they have a direct correlation with the available space and carry weight capacity of each platform. Additionally, the collector and detector size are dependent of each other, because of what is known as the image circle from the collector. If the detector area is bigger than the image circle from the collector, then the detector sensor is oversized and inefficient. On the other hand, advances in microprocessors and electronics allows to save space and weight for powerful processing modules so in this study the processing module characteristics will be ignored; however, the energy consumption needed for data acquisition will be considered. The energy consumption of each platform is an important parameter that needs to be evaluated because it is one of the factors that determine how much data can be acquired.

Is important to get familiar with the optical system main terms and properties. For the collector we have the aperture and the focal length. The aperture are the linear dimensions of the first optical element in a collector through which the energy is gathered; generally, this parameter is expressed in diameter assuming that the aperture is circular. The bigger the aperture the more energy can be collected. The aperture generally has a lens to help redirect the light to the detector. The effective focal length refers to the physical dimension required by the collector to gather and redirect incident energy onto the detector [10]. The image gets formed further down the line from the effective focal length, known as image distance. There is an important relationship between the distance of the object being captured, the focal length, and the image distance (1.1.1). The larger the object´s distance the closer the image distance is to the focal length, effectively making the focal length the same as the image distance which is particularly true for satellites. The effective focal length needed to create an image is achieved by moving the internal lenses and mirrors in the collector, the lens focus length determines the maximum effective focal distance for the system. Additionally, the object distance and image distance can give us the magnification factor (1.1.2). Figure 1.1 shows the main relationship between the object distance, image distance and effective focal distance. Knowing the image distance as in the case of this study can help determine the effective focal length according to the object´s distance.

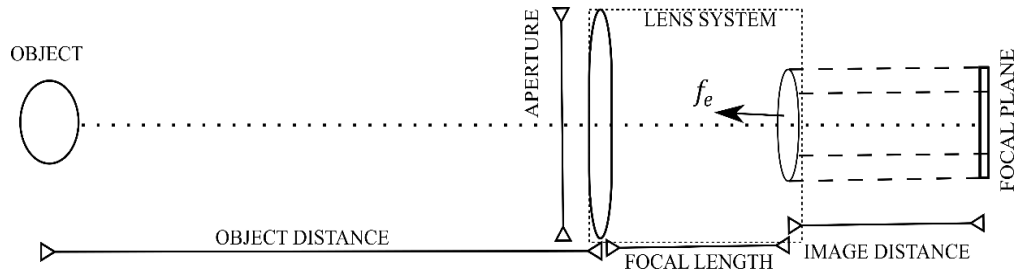

Figure 1.1. Description of distances in the lens equation
(Source: own)

The detector needs to be placed at the receiving end of the image distance known as the focal plane. For the detector, the main properties are physical dimensions, number of pixels, and size of each pixel. The actual size of the detector and the focal length of the optics gives us the Field of view (FOV) of the system, which is the solid angle through which energy is collected (1.1.3). The imaginary line passing through the center of the FOV is known as boresight. The FOV has a direct relationship with the instantaneous field of view IFOV, which is the actual area on the ground that the camera can see (1.1.4). Finally, another

important parameter is the ground sample distance (GSD), which is the IFOV of one pixel given in linear dimension along track (x) and cross track (y). Furthermore, for remote sensing is necessary to consider the angle at which the boresight is located with respect to the ground being sampled. Nevertheless, for this study is not necessary to get into that detail so it will only be considered nadir viewing scenarios (i.e. the boresight aligns with the object being imaged).

$$\frac{1}{f_e} = \frac{1}{d_{object}} + \frac{1}{d_{image}} \tag{1.1.1}$$

$$M_F = \frac{d_{image}}{d_{object}} \tag{1.1.2}$$

$$\Omega_{FOV} = \theta_x \theta_y = \frac{xy}{f_e^2} \tag{1.1.3}$$

$$IFOV = XY = {d_{object}}^2 \theta_x \theta_y = d_{object}^2 \Omega_{FOV} \tag{1.1.4}$$

$$GSD_X = \frac{X}{m} \tag{1.1.5}$$

$$GSD_Y = \frac{Y}{n} \tag{1.1.6}$$

$$\Omega_{pixel} = \frac{\Omega_{FOV}}{m\,n} \tag{1.1.7}$$

$$IFOV_{pixel} = \frac{IFOV}{m\,n} \tag{1.1.8}$$

Spatial resolution

As previously mentioned in aerial and space photography spatial resolution refers to the ability to distinguish small adjacent objects [11]. The GSD does not necessarily imply that two objects located that distance apart can be distinguished, the Rayleigh and Nyquist criterion must be considered [13]. The Rayleigh spatial resolution criterion states that the maximum signal from an object cannot overlap the maximum of another, as a minimum it can overlap the minimum of the second object. The minimum angular separation between two identifiable objects according to Rayleigh can be calculated using the wavelength and aperture, (1.1.9). On the other hand, the Nyquist criterion states that the sample rate used by the camera must be twice the frequency of the object to spatially resolve it. Nevertheless, the Nyquist criterion is only applicable if the Rayleigh criterion is resolved first, and if there are enough pixels that caught the image. This study will not get into changing the sample rate to accommodate every single object that the camera may try to capture. Instead, it will

focus on the minimum angular separation required between two identifiable objects and compare it to the angular GSD of the camera in each platform.

$$\theta_{min} = 1.22 \frac{\lambda}{D_A} \tag{1.1.9}$$

Spectral resolution

This refers to the electromagnetic spectrum range that the camera system can detect and capture. The optical system is designed from its collector to its detector to work with specific wavelengths of the spectra. In this study we are using an RGB camera, which clearly states that it can capture visible light in the green, blue and red spectrum. Most CMOS and CEE sensors can work with the near infrared signatures because of its proximity to the red. All cameras used in this study will operate in the same electromagnetic spectrum for all three aerospace platforms. Nevertheless, it is important to consider that clouds generate a problem at these wavelengths because they absorb and scatter visible light. This study does not get into the scattering and absorption phenomenon of clouds, instead it will focus on the amount of cloud coverage and the typical altitude of clouds. According to the meteorology department at the Astronomical observatory of Quito [14], the lowest clouds around Quito can be between 1 to 2 km from the surface. Figure 1.2 shows the daily average of sunlight collected with ground equipment during the entire year of 2017, was created using data provided by the meteorology unit of the Astronomical Observatory of Quito [14]. This information is useful when analyzing the chances of taking surface pictures using aerospace platforms at altitudes higher than 1 to 2 km from the surface.

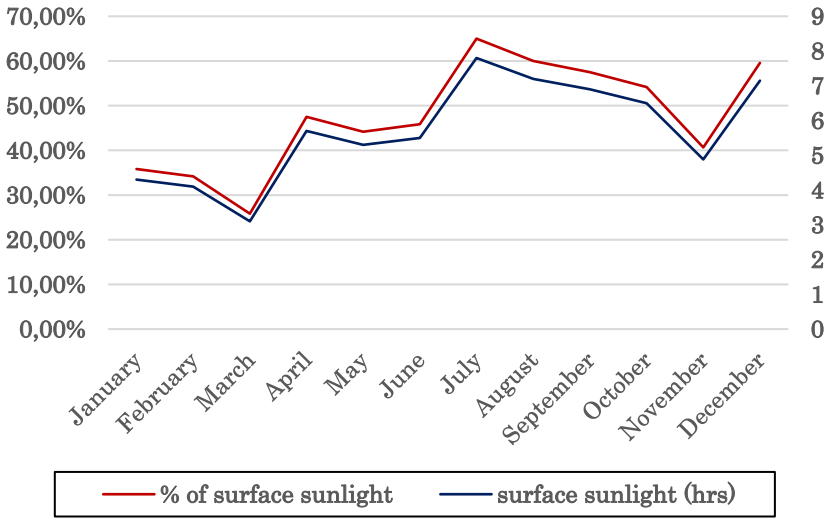

Figure 1.2. Yearly sunlight in Quito, 2017
(Source: Reference [14])

Temporal resolution

Analysis and results from remote sensing are greatly amplified if there is an element of time associated with it. Temporal resolution refers to the ability to see change over time. The collection time in analysis plays an important role depending on the main objectives with remote sensing. For example, if monitoring an area is important then it is necessary to take images of the same area several times during an extended period. If it is important to see a moving object, then it is necessary to take many samples during the duration of the movement of the object. For the later one is important to have a fast frame rate (1.1.10), that allows multiple samples collection to detect movement. The continuous collection period of the RGB camera in this case is known as integration time (1.1.11). The integration time together with the sample time can be used to calculate the duty cycle. A higher duty cycle can detect movement since it refers to the number of samples associated with it. Multiple duty cycles over the same area at different times will help detect change over time. CMOS sensors can increase the frame rate by utilizing less pixels in their array. This technique is known as windowing capabilities of the sensors, generally provided by the manufacturer [15]. However, using less pixels will diminish the resolution of the image.

$$R_{frame} = \frac{1}{T_{sample}} \tag{1.1.10}$$

$$C_{duty} = \frac{T_{int}}{T_{sample}} \tag{1.1.11}$$

Radiometric resolution

There is a background noise associated with every image, and the ability of distinguish different objects in the image will depend on its level. This study will not get into noise suppression techniques because the same techniques can be used for all three cases. Nevertheless, is important to mention that the level of energy signal (emissivity) (S) from an object decreases with a larger distance. The energy of the noise (N) will also decrease, but the ratio will remain, (1.1.12) [10]. K being a value determined from many more parameters outside the scope of this study, such as the actual interference of the atmosphere. The intensity of the object (I) enters in the equation, but we will ignore it since we can assume that we are looking at the same object with the three platforms. In this context, we can create a signal factor due to the distance (in meters) of the object, (1.1.13).

$$\frac{S}{N} = \frac{K\, I_{\lambda}}{N} \frac{1}{\mathrm{d}^2_{\mathrm{object}}} \tag{1.1.12}$$

$$S_F = \frac{1}{d^2_{object}} \tag{1.1.13}$$

Technical features of the payload used in this study

Actual payload selection is not important in this study; instead, the most important parameter for the payload in this study is the ratio between its mass to the total platform mass. This metric is important because combined with other performance parameters can give an interesting picture of the capability of each platform to carry bigger and better cameras. Nevertheless, a common RGB camera is used in all three platforms to have the same technical features when determining the resolution metrics previously explained. Since the actual camera selection is not the focus of this study the camera selected for the nanosatellite was used in all three platforms. The main reason for this is because there are not many options for cameras that are approved for space. Detail of the calculation and results of the different resolution metrics are provided in the methodology and result sections.

As mentioned at the beginning of this chapter, there are three main components in the camera system: the collector, the detector and the processing module. The basic design of the camera payload designed for the nano-satellite is presented in Figure 1.3 [16]. The design is for the harsh environments of space, that is why there is a Heat/EMI shield. Its main function is to prevent over heating of the sensor and magnetic interference for a small weight and volume increase. For this reason, it will be included in all three platforms. The lens is the Xenon-RUBY 2.2/25 from Schneider Optische Werke GmbH [17], shown in Figure 1.4. The detector is the MT9T031 CMOS sensor manufactured by Micron [15]. The processing module uses a high-performance power-efficient ARM cortex-A5 chip (Atmel SAMA5D35). Additionally, it has 512 MB of DDR2, 4GB eMMC flash memory, 64 MB NOR flash memory, and 32 KB of F-RAM memory. All the main components of the printed computer board (PCB) are shown in Figure 1.5. Table 1.1 summarizes the most important technical parameters for this camera system.

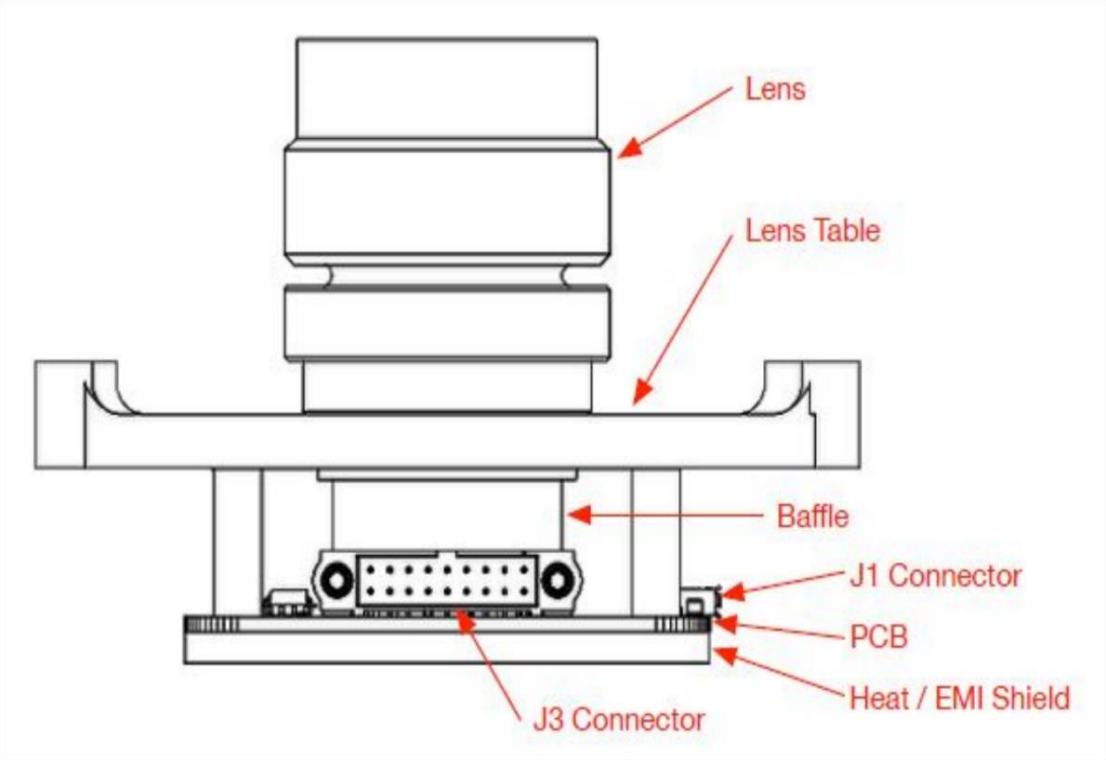

Figure 1.3. RGB camera payload
(Source: Reference [16])

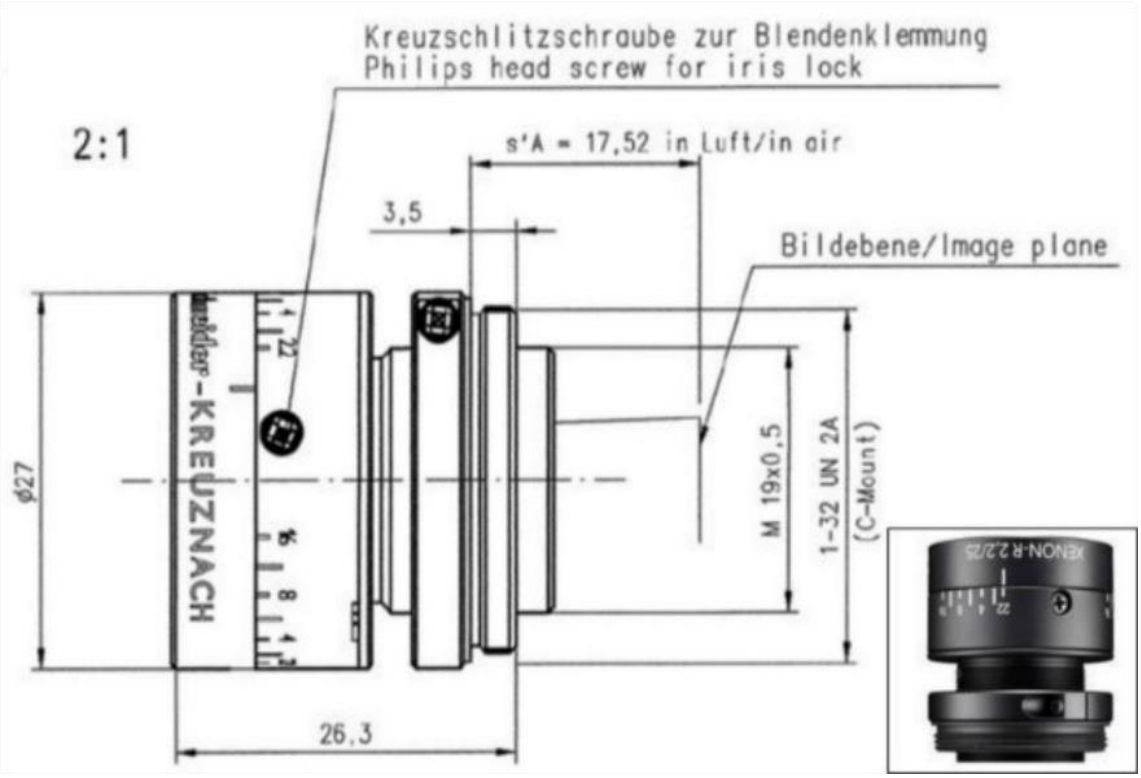

Figure 1.4. Xenon-RUBY 2.2/25 Lens
(Source: Reference [17])

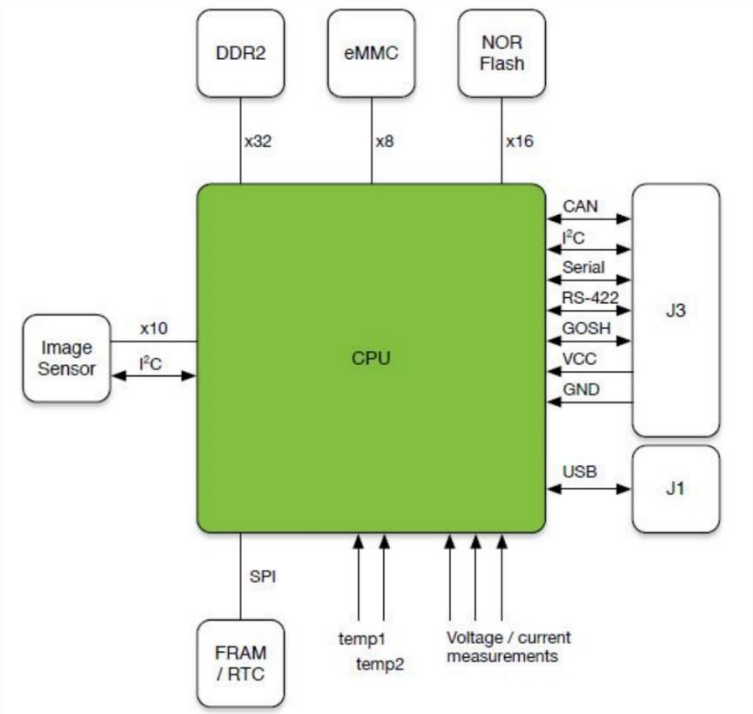

Figure 1.5. RGB camera payload schematic
(Source: Reference [18])

Table 1.1. RGB camera main characteristics.

Collector (Xenon-RUBY 2.2/25)	
Material	Industrial lens and robust metal body
Focusing mechanism	Internal M25.5 x 0.5 thread with a robust locking mechanism
Image distance	17.52 mm back focal distance for image plane
Image circle	9 mm
Mass	29 grams
Total external dimensions	Maximum diameter of 27 mm and maximum length of 40.32 mm including c-mount and its back focal length
Electromagnetic spectrum	400 nm to 1000 nm blue ~ 450 nm Green ~ 550 nm Red ~ 650 nm Near IR ~750 nm
Aperture diameter	25.5 mm
Detector (MT9T031 CMOS)	
Sensor size	6.55 mm by 4.92 mm
Color sensor	10-bit RGGB Bayer pattern
Number of pixels	2048 x 1536 (3 megapixel)
Pixel size	3.125 um x 3.125 um

Frame Rate all pixels (2048 X 1536)	12 fps
Image acquisition response time	5 s
Processing module (PCB)	
size	54.7 mm by 54.7 and 5.6 mm thick including the heat/EMI shield
Mass	77 grams
Atmel SAMA5D35 processor	High performance ARM processor Cortex-A5
RAM	512 MB DDR2
Storage	4GB (2GB for image storage)
Independent system boot	Dedicated 64MB NOR flash memory
Image processing response time	10 s

(Source: Reference [17] [18])

The MT9T031 CMOS sensor has windowing capabilities as previously mentioned. The different frame rates and corresponding resolutions are listed in Table 1.2. This information is used for the RGB camera payload analysis.

Table 1.2. RGB camera windowing capabilities.

Resolution	Frame Rate (fps)	Column Size (pixel #)	Row Size (pixel #)
2048 x 1536 QXGA	12	2047	1535
1600 x 1200 UXGA	20	1599	1199
1280 x 1024 SXGA	27	1279	1023
1024 x 768 XGA	43	1023	767
800 x 600 SVGA	65	799	599
640 x 480 VGA	93	639	479
1920 x 1080 HDTV1	18	1919	1079
1280 x 720 HDTV2	39	1279	719

(Source: Refernce [15])

1.2. Weather balloons

The use of balloons for science and meteorology is wide and well documented. Many authors would argue several advantages regarding low costs [19] [20] and the spatial and temporal resolution of the collected data [21]. There are two basic types of balloons, an open system also known as zero-pressure that allows gas to flow out and a closed system that keeps gas in also known as pressure balloon. Generally, the zero-pressure balloons

are used for science missions up to the stratosphere [21]; while, the smaller pressure balloons are used as weather probes, which is the focus of this study.

A disadvantage of weather balloons, compared to other aerospace platforms, is that their trajectories are arbitrary and difficult to predict as they depend on the atmospheric conditions at the launch site and at different altitudes. For this reason, several authors have created tools to predict the possible trajectories that balloons might take. One such tool is ASTRA (Atmospheric Science Through Robotic Aircraft) [22]; which, is based on a stochastic model delivered from thousands of radiosonde flights and uses a Monte Carlo framework to incorporate sources of uncertainty and estimate errors. The balloon trajectory model presented for this study is built from physical theories concerning the dynamics of the balloon. This model is used to determine parameters that help study the performance of the RGB camera mounted in the balloon. The ASTRA model and the CUSF model [23] were used to validate this mathematical model as shown latter on in this thesis.

Weather balloon dynamics

The following figure simplify the forces acting on the balloon. This simplification looks at vertical forces and horizontal forces as (x, y, z) components. The horizontal forces are the x and y components of drag on the balloon system caused by the air flow over it. The flow of air at any given time throughout the balloon flight is considered steady, incompressible, and non-viscous. According to Muirhead and Downing [24] steady flow is constant according to an specific observer; incompressible, as flow with no change in density in the flow field; and air for the most part can be considered non-viscous; expect for the boundary layer. In real life there is no incompressible flow when an object is in motion; however, considering a flow as incompressible simplifies the model here presented. Considering the flow as incompressible is standard practice for most aerospace applications with a Mach number (M_N) less than 0.3 [24]. As shown later in this document the air speed of the balloon system will be less than 0.1 M_N at any time during the flight. Additionally, it is important to clarify that the flow is steady at a specific point of the model as observed by the balloon system; however, the model takes into consideration the changing atmospheric and wind conditions with a time step of one second. The viscosity of the air will also depend of the atmospheric condition of the exact position of the balloon system, which depends on the altitude.

There are three forces that act in the vertical direction. These forces can be related with the following dynamic equation of equilibrium (1.2.1).

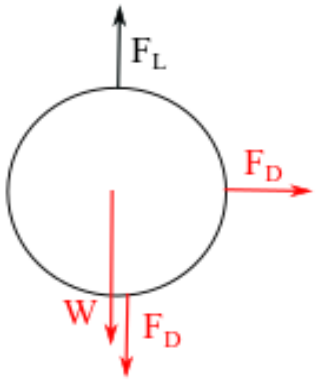

Figure 1.6. Forces acting on the balloon
(Source: Own)

$$M_{total} acc_V = F_L - W - F_{D_V} \quad (1.2.1)$$

$$W = M_{total} * g_o \quad (1.2.2)$$

$$F_{D_V} = \frac{1}{2} C_D \, \rho {V_{e_V}}^2 A_{bal} \quad (1.2.3)$$

$$F_L = M_L * g_o \quad (1.2.4)$$

The lifting force depends on the type of gas that is used, in the case of this work the chosen gas is helium. Archimedes principle states that the buoyant force is equal to the weight of the displaced fluid. This allows us to find a relationship between the mass and the volume of gas (eq. 1.2.5), where the buoyancy lifting factor (B_i) (eq. 1.2.6) is a density relation between the gas and air. The error is calculated as 0.803, a value that corresponds to the purity of the gas (assumed at 95%), times back pressure consideration (0.995) [25], and times a correction factor of 0.85 because experience says that gross static lift should exceed load by 15% [26]. The lifting mass (M_L) is a control variable that determines the rate of accent of the balloon since it is directly related to the volume of gas and not the actual total weight, in fact is the total mass plus and additional 'lifting mass'.

$$M_L = B_i \, Vol_i \quad (1.2.5)$$

$$B_i = \frac{\rho_{air_i}}{\rho_{air_o}} B_o \, Err \quad (1.2.6)$$

$$B_o = \rho_{air_o} - \rho_{h_o} \quad (1.2.7)$$

The model implements this principle as a control variable as shown latter on. Furthermore, is important to understand that the atmospheric conditions change constantly as the balloon climbs. To simulate the changing conditions, the simulation implements the COESA 1976 model [27]. The changing atmospheric conditions result in the change of the balloon size and volume affecting its drag dynamics, which is considered in the balloon trajectory model.

In addition, As seen in figure 1.6. there is a force acting in the horizontal direction. This force is due to the drag of the wind on the balloon system. Equation (1.2.3.) can be used to find this force for the x and y components, where the velocity is the relative velocity of the wind to the balloon system. The wind direction and velocity changes constantly so it is necessary to implement a wind model in the horizontal trajectory simulation, the HWM model [28] was used for this purpose. Here, it is also necessary to give the following dynamic equation of equilibrium, which is the building block for the model that will be discussed latter. Equation (1.2.3) can also be used to calculate the drag in the horizontal plane.

$$M_{total} * acc_H^2 = F_{D_H} \tag{1.2.8}$$

Weather balloon power requirements

The power and energy consumption calculation for the weather balloon is straight forward using as basis the electric power (1.5.1) [29]. For this calculation it is necessary to get the electrical characteristics for the electronic components used in the platforms. Energy given in Watt-hour determines how much power is consumed as a function of time (1.5.2). The most important parameter is the power requirement for the electronic component to function normally. All three platforms use batteries to store energy needed to power the electronic components. The main parameter used to determine the life of batteries is the battery capacity (1.5.3). The battery capacity represents the maximum amount of energy that can be extracted from the battery under specified conditions [30]. The charging and discharging rates affect the capacity of the battery, typically higher current draws increase the discharge rate lowering the capacity. Additionally, the temperature also affects the capacity with lower temperatures reducing the capacity of the battery [30].

$$P = VI \tag{1.5.1}$$

$$E = P\Delta t \tag{1.5.2}$$

$$L_b = \frac{B_c}{\Sigma I} \tag{1.5.3}$$

This work uses the three main equations presented above to estimate the battery current consumption of the weather balloon in this study and from that determine the life of the

battery in seconds for the different cases presented in the methodology section. These are estimated calculations that do not consider temperature effects on the batteries.

Technical features of the weather balloons used in this study

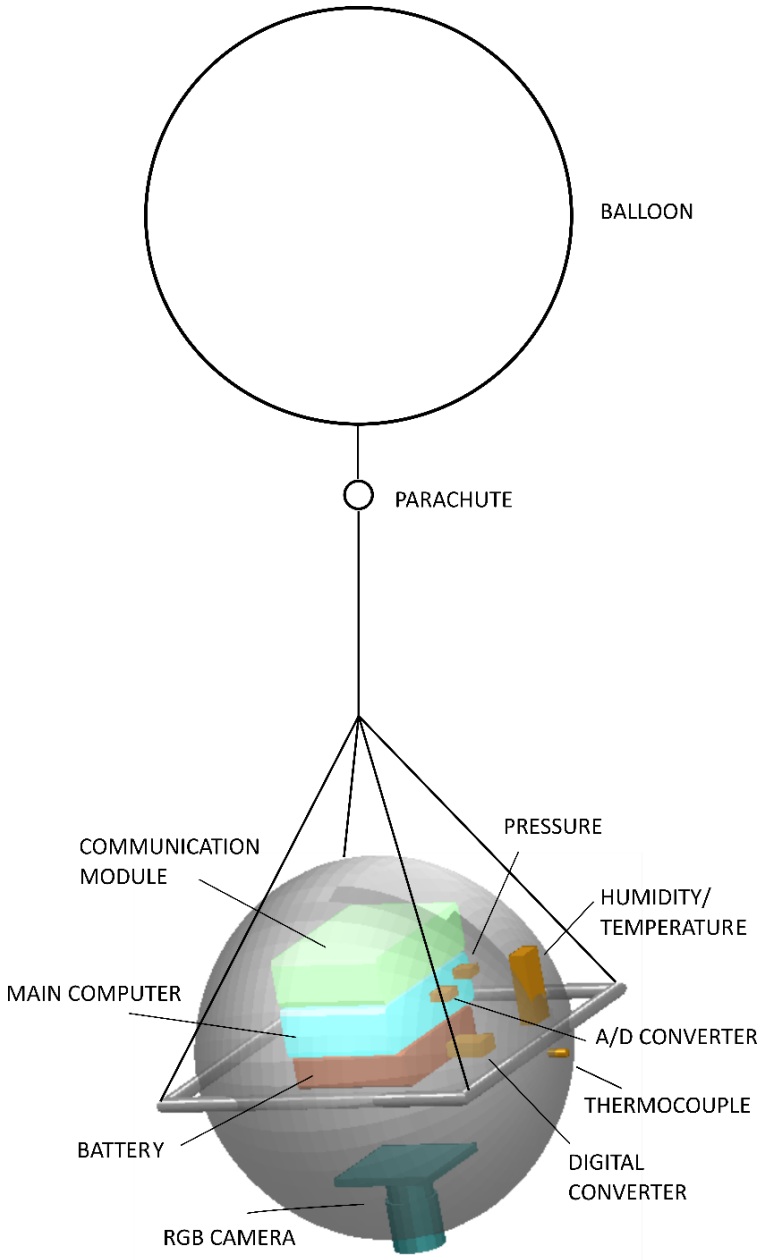

Figure 1.7. Weather balloon conceptual design
(Source: own)

Project PIS-15-10 of the Escuela Politécnica Nacional involved the design and development of weather balloons, Figure 1.7. The weather balloons are designed to carry typical atmospheric sensors as well as a camera. For this study, the power system model incorporates all the atmospheric sensors in addition to the camera for energy consumption

estimation because they are a minimum requirement for weather balloons. Weather balloons have three main components: the balloon, the radiosonde, and the parachute. The balloon is made of highly flexible latex and its main technical parameter is its mass. Higher mass balloons can carry heavier loads and can reach higher altitudes. The radiosonde carries all the sensors, electronics, and communication equipment. Its main structure is made of aluminum, while the outside structure or fuselage is an expanded polystyrene (EPS) sphere with a diameter of 200 mm. Supporting structures to hold the components in place are made of PLS using additive manufacturing. Additionally, a 3-axis gimbal stabilizer for the camera payload will need to be considered since the radiosonde will have strong unpredicted moves. Figure 1.8, shows and example of such gimbal equipment adding additional cost and weight to the system. The additional weight added in this case is 230 grams. The parachute is needed for a safe landing of the radiosonde and the safety of any life or property on land. A good landing speed range is 5 m/s to 7 m/s, less than 5 m/s would prolong the descent and the wind would take it a longer distance and greater than 7 m/s is dangerous [31]. The weight of the weather probe suggest that a 1.5 m parachute is needed.

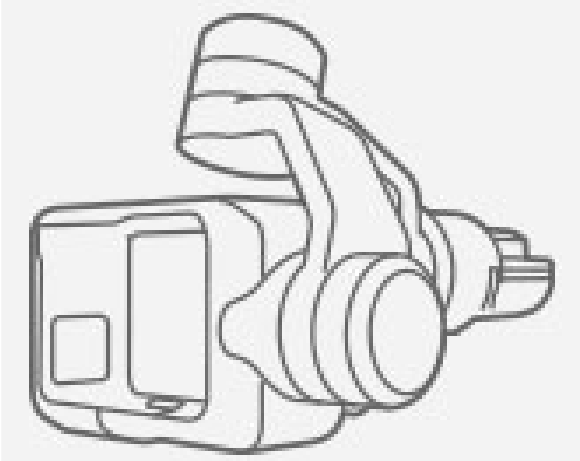

Figure 1.8. Gimbal stabilizer for cameras (3-axis)
(Source: Reference [32])

The weather balloon system is lifted as previously explained because of the buoyancy principle, and while airborne it will adapt a trajectory according to the velocity and direction of the wind. This trajectory is hard to control, and any control methods are outside of the scope of this work. Additionally, the possibility of collecting camera data on the decent with the parachute is also ruled out because the landing location could be any random place. Table 1.3 summarizes the main balloon system parameters according to the design that were used in this study. The burst altitude is given by experience data from High Altitude Science [31]. As it can be seen there are two balloon sizes (A and B) used in this study that

climb at the same rate and a third case study using a balloon of the same size as A, but with a faster climb rate. An important figure of merit that can be determined from the design specifications of each platform is the payload to platform mass ratio. Additionally, the structure to overall radiosonde mass ratio is 63%, which is an important figure for this study. The power comes from four lithium ion cells rated at 2.7 V and 2500 mAh each. Two cells are connected in parallel to increase their life (ensure a minimum of 2500 mAh) and each pair of cells are connected in series to double the voltage supply to 5.4 V. Table 1.4 shows the power parameters used for the weather balloon power requirement analysis

Table 1.3. Balloon system parameters used in this study

Parameter	Value	Units
Balloon A		
Mass	0.35	kg
Burst altitude	26 to 29	km
Balloon B		
Mass	0.6	kg
Burst altitude	29 to 32	km
Balloon C		
Mass	0.35	kg
Burst altitude	26 to 29	km
Radiosonde		
Mass	1.596	kg
Structure mass ratio	49,88	%
Max supply voltage	5.4	V
Battery capacity (minimum)	2500	mAh
Available payload volume	50	%
Payload to platform mass ratio	21.05	%
Parachute (1.5 m)		
Mass	0.19	kg
Landing speed	5.32	m/s

(Source: Reference [31])

Table 1.4. Parameters used in the balloon power requirements calculation

Components	Function	Response time (s)	Power Rating (W)
Main Computer	Control and command	~	3.5
Sensors	Humidity / Temperature	2	0.0033
	Pressure	0.02	0.0357

	A/D Converter	0.02	0.0033
	Thermocouple to digital converter	0.22	0.00825
Com Module	Communication and Navigation		1.05
RGB Camera	Boot	15	1.3
	Idle	~	0.38
	Image acquisition	5	0.8
	Image processing	10	0.8
	Computation (other)	~	0.85

(Source: Reference [33] [34] [35] [36] [37] [18])

1.3. Nanosatellite

Orbital dynamics

Dynamics of a satellite's orbit around the earth can be simplified using the laws of Kepler and Newton, and by adopting a two-mass model system [38]. In any number mass model, the masses rotate around a common point referred as barycenter, which is the center of mass for the system. Nevertheless, it is regular practice in orbit mechanics for a two-mass system in which one mass is significantly larger than the other one (i.e. the Earth and an orbiting satellite) to use the center of the bigger mass as the center of the system. For the scope of this research this theoretical framework is adequate for orbit simulation.

Classical mechanics from Newton is one of the pillars in orbital dynamics revealing the behavior of two masses in space. The first law tells us that a mass will remain at rest or constant movement and/or rotation until it experiences an external force and/or torque. This law defines the moment of inertia of a mass, which can be explained as the resistance of a mass to change its state. The second law give us relationships between force, mass, and acceleration (1.3.1) and between torque, moment of inertia, and angular velocity (1.3.2). Further exploration of this law reveals that there are two types of external forces and torques that can act on a mass: direct contact forces and torques and those caused by the mass of distant objects. The third law tells us that forces and torques come in pairs because for every force or torque there is an equal reaction force and torque.

Figure *1.9* shows the two main forces that act on a satellite through its orbit. A direct consequence of this principle is the law of momentum conservation, which is the most fundamental principle in orbit control. Finally, Newton also gave us the law of universal

gravitation (1.3.3.), where (G) is the gravitational constant. This equation represents a two-mass system; however, the universe is a multi-mass system, but the two-mass approximation works perfectly for modeling satellites orbiting the earth. Two masses interacting together will rotate about a common center known as the barycenter; it is also a common practice to consider the center of the bigger mass as the center of the system, this is especially true when one of the masses is significantly bigger, as is the case of the Earth and a satellite.

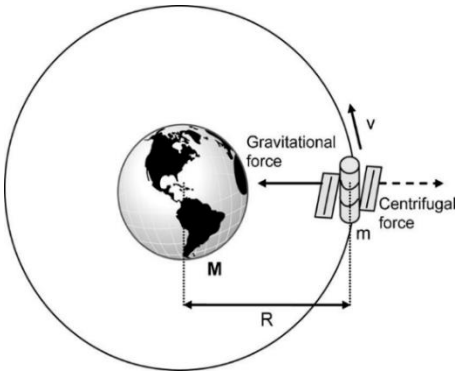

Figure 1.9. Gravitational and centrifugal forces acting on masses orbiting Earth
(Source: Reference [39])

$$F = ma \tag{1.3.1}$$

$$\tau = \frac{I}{\alpha} \tag{1.3.2}$$

$$F = \frac{G*M*m}{R^2} \tag{1.3.3}$$

Johannes Kepler (1571-1630) was a German astronomer that conducted research on the dynamics of the planets around the sun. His first law says that all orbits in space follow conical trajectories, [40], Figure 1.10 and he stablished a geometrical relationship to represent these orbits (1.3.4). His second law reinforces the law of momentum conservation. This is particularly important in orbit dynamics because it states that the linear momentum and angular momentum will be conserved (will be the same) throughout its orbit. The third law is also known as the law of periods [39] and gives us a direct relationship between the semi-mayor axis and the orbit's period for elliptical orbits (1.3.5).

$$r = \frac{p}{1+e\ cos\theta} \tag{1.3.4}$$

$$T = \left(\frac{2\pi}{\sqrt{\mu}}\right) a^{3/2} \tag{1.3.5}$$

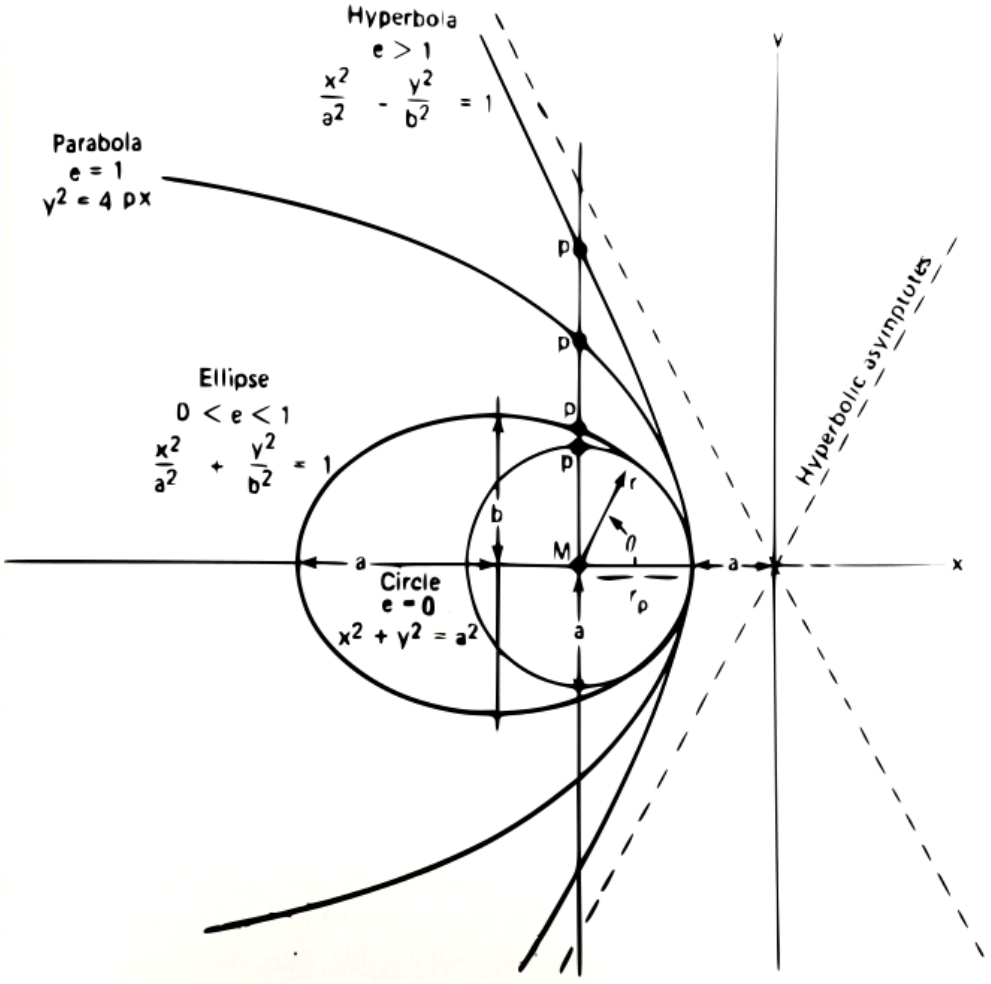

Figure 1.10. Geometrical properties of orbits in space
(Source: Reference [40])

Summing up, Newton and Kepler help determine three main conclusions that form the basis in orbit mechanics:

- The center of mass (barycenter) of a two-mass system does not have acceleration, consequently it serves as the origin of an inertial reference plane.
- The angular momentum of the system is constant, consequently the movement of the masses is perpendicular to the angular momentum vector.
- The mases will follow conical trajectories in relation to the inertial reference plane.

The shape of the orbit is determined by Kepler's first law (1.3.4) and it uses a bidimensional polar coordinate system (distance and angle) to express the main orbital parameters. There are four types of conics that model the trajectories in space. However, the circular orbit, which has an eccentricity of 0 is a special case that requires perfect conditions, impossible to have in real life; therefore, the orbits of satellites around the Earth are all elliptical with eccentricities greater than 0 but less than 1.

Each orbit is in its own plane perpendicular to the angular momentum of the mass and generally is expressed with reference to the inertial plane using polar coordinates [38]. The most common inertial reference plane used for earth satellite orbits is the Earth Centered Inertial system (ECI), which is a Cartesian system, horizontal plane in Figure 1.11. The origin of the ECI is the vernal equinox, when the north and south pole are aligned such that their distance to the sun is the same, making this the x-axis of the plane. The z-axis is perpendicular to the x-axis and points to the north, while the y-axis follows the right-hand rule and it points perpendicular to the hand palm, being the four finger the x-axis. There are six Keplerian elements that can easily define an orbit´s shape, size and location with respect to the ECI, Table 1.5. It is important to mention that the location of the satellite´s orbit that is closest to the barycenter is known as periapsis or perigee, while the furthest distance is known as apoapsis or apogee.

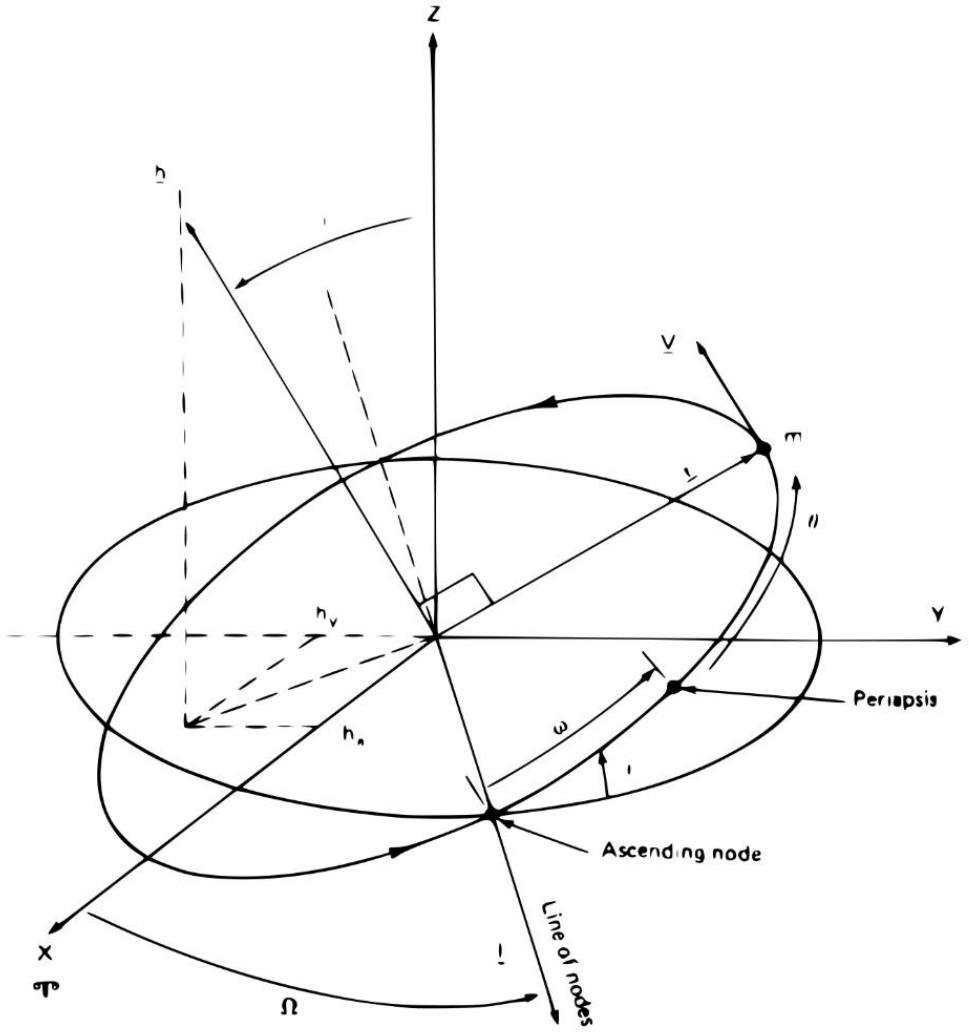

Figure 1.11. Orbital plane with Keplerian elements
(Source: Reference [40])

Table 1.5. Keplerian orbital elements.

Symbol	Description	Units
a	Semi-mayor axis measured from the center of the Earth	km
e	Eccentricity: defines the shape of the conic	-
i	Inclination of the satellite´s plane to the ECI plane	degrees / radians
Ω	Right ascension of the ascending node, measured from the x-axis of the ECI	degrees / radians
ω	Argument of periapsis, measured counterclockwise from the ascending node in the orbit plane	degrees / radians
θ	True anomaly at epoch or time of relevant periapsis passage	degrees / radians

Source (Reference [38])

Orbit mechanics near Earth (i.e. earth satellite orbits) usually uses the time as defined by Newton as another orbital element [38]. The time according to Newton moves forward with well-defined beginning and end, in which events occur. The origin of time, also referred as Epoch for many astronomical applications including celestial mechanics is Julian year cero (1st of January, 4713 AC), established as the International Atomic Time (TAI) the 1st of January, 1958 [38]. The TAI uses the sidereal time to measure time, being this the real time that the earth takes to rotate around its axis (23 hours, 56 minutes, 4.0905 seconds).

There are four main types of earth orbits, Figure 1.12. Low Earth Orbits (LEO) are located at altitudes of 160 km to 1500 km from the surface of the Earth and have typical inclinations of 0^{o} (equatorial) to 90^{o} (polar). There are ambient conditions that will eventually cause satellites in these orbits to decay. The Medium Earth Orbits (MEO) are located at altitudes of 2000 km to 35000 km. The Geosynchronous Orbits (GSO) are orbits that are synchronies to the rotation of the Earth to have constant coverage of a specific area. To achieve these orbits the following conditions must be met: altitude = 35786 km, and inclination = 0^{o}. The highly elliptical orbits (HEO) are orbits with high eccentricity and are used to have better coverage of specific areas of the Earth. The HEOs have a significant contrast between apogee and perigee. Additionally, the orbits can be classified in two groups according to their direction of travel [39]. Orbits with an inclination of 0^{o} to 90^{o} travel in the same direction as the rotation of Earth and are known as prograde, while orbits with an inclination of 90^{o} to 180^{o} travel in the opposite direction of the rotation of Earth and are known as retrograde orbits. In LEO orbits there is a special type of retrograde orbit known as sun-synchronous orbit with an inclination between 96^{o} and 104^{o} that is in constant contact with the sun.

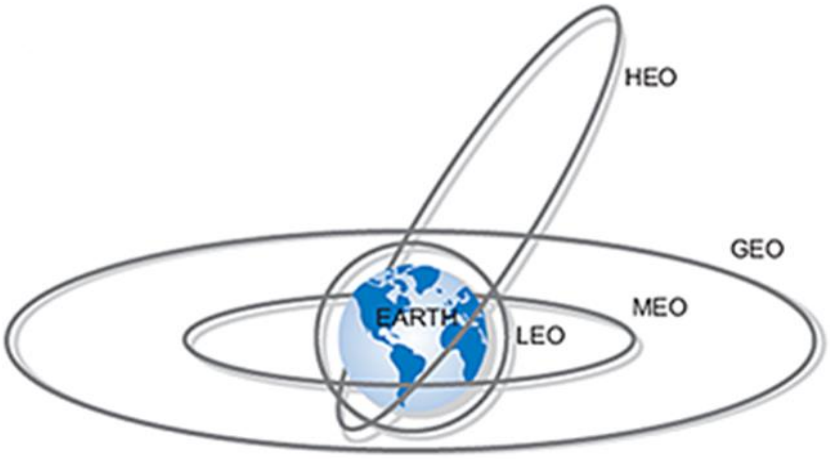

Figure 1.12. Types of Erath orbits
(Source: Reference [38])

Furthermore, earth's atmosphere is considered homogeneous until approximately 86 km of altitude, above this height, dissociation of its particles take place [41], and the environment can be referred as mostly plasma. The main environmental considerations at LEO orbits are: the density, charged particles, solar radiation pressure (SRP), solar wind, Earth´s magnetic field, other radiation sources, orbital debris, and micrometeoroids. Of this the two that mostly affect the trajectory of the orbit are density and SRP. The atmospheric density at LEO orbits is very small, but still significant to create drag forces that contribute towards an eventual decay of the satellite. In fact, satellites at altitudes less than 200 km tend to decay quickly [38]. On the other hand, solar radiation carries momentum, and this results in a force acting against the satellite [41]. With respect to temperature, the only heat exchange mechanism is through radiation, being the sun the main source of heating [41]. Forces caused by this environment are referred as perturbations and affect orbits and attitude of the satellites. High fidelity models such as the one used in this study include these perturbations.

Nanosatellite power requirements

The equations introduced for the weather balloon are also used to determine the power consumption of the nanosatellite. Nevertheless, the nanosatellite incorporates solar panels bringing a charging capacity to the batteries that need to be considered. The Power generated by the solar panels depend on the efficiency of the solar panels and the orbital dynamics as discussed in section 1.3. Sanchez, [42] performed an analysis to determine the power generated by solar panels in a LEO orbit and how this determines the charging behavior of the batteries. For this they used a 3U nanosatellite and studied three scenarios: free rotating, sun pointing, and nadir pointing. The last scenario being of interest in this

study since as mention latter on in this document the nanosatellite in this study will also point at nadir. For nadir pointing satellites they concluded that four faces are exposed to sunlight and exhibit a sinusoidal behavior of radiation. LOE nanosatellites in a near polar orbit will receive sunlight for approximately 63.36 % of its period as shown by Figure 1.13. From this information they calculated how much radiation can be harvested, Figure 1.14. On the other hand, Figure 1.15 shows how much radiation can be harvested by one face always pointing directly at the sun [42].

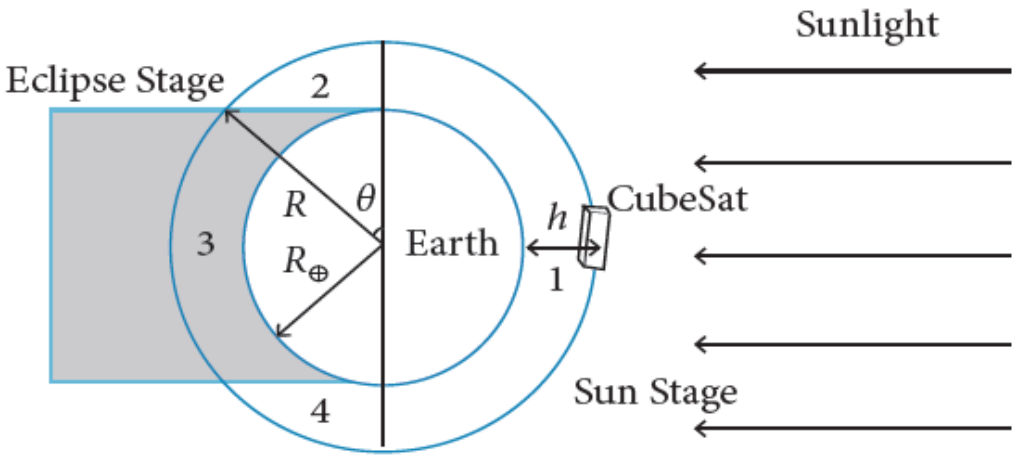

Figure 1.13. Sunlight in near polar LEO orbits
(Source: Reference [42])

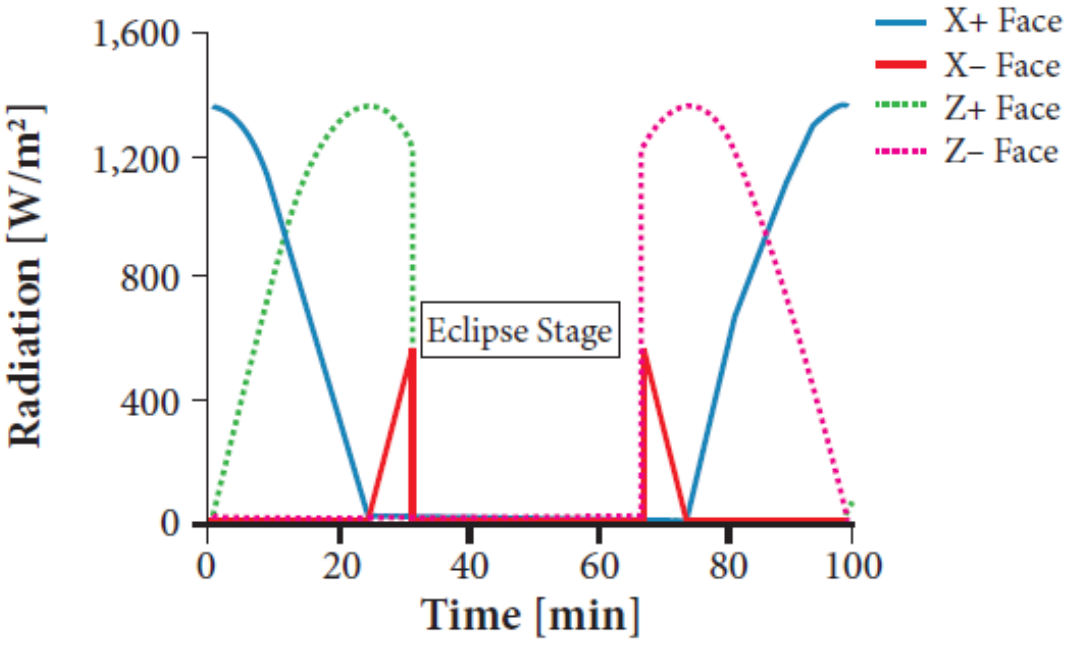

Figure 1.14. Harvested radiation in a LEO orbit
(Source: Reference [42])

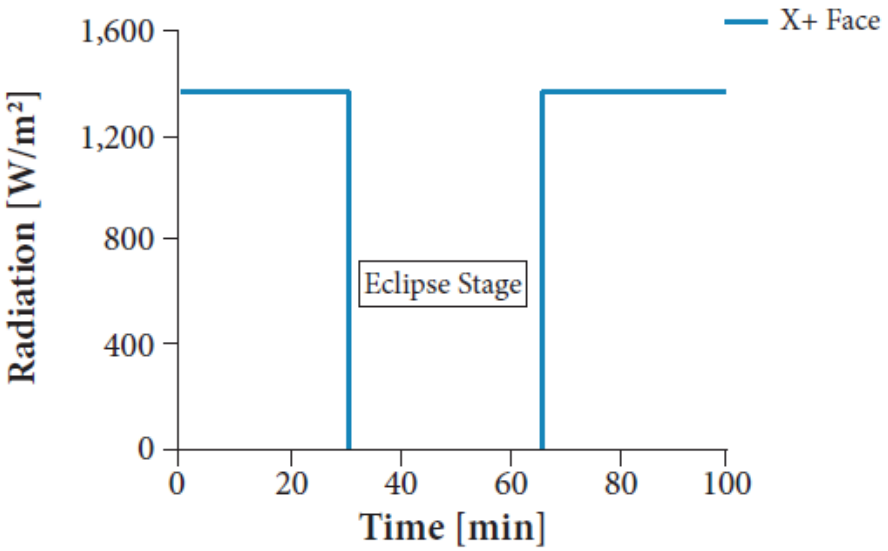

Figure 1.15. Radiation received with one face pointing constantly at the sun
(Source: Reference [42])

This thesis will use a modeling and simulation software called General Mission Analysis tool (GMAT) [43] to determine the sun and eclipse stages according to each orbit scenarios. While, Figure 1.14 can be used to determine a percentage of power that can be generated by the solar panels by finding the area under each curve and comparing them to the curve in Figure 1.15. Data points from Figure 1.14 were plotted to calculate the function of each curve presented next. Note that the same function as Z+ face can be used to calculate the Z- face.

$$Rad_{X+} = 0.112x^3 - 5.5x^2 + 18.8x + 1360 \quad (1.5.4)$$

$$Rad_{Z+} = -0.00002x^6 + 0.0022x^5 - 0.09x^4 + 1.58x^3 - 12.47x^2 + 114.58x \quad (1.5.5)$$

$$Rad_{X-} = 72.5x \quad (1.5.6)$$

The above functions can be integrated over the corresponding time period to find the percentage of power generation, Table 1.6. Since, each orbit has a different period, the percentage of power generated per period will work for any orbit scenario. This information is cross-referenced with the manufacturer's information about the solar panel optimum power generation to determine de real power generated during the sun radiation stage of the orbit. The GMAT model takes care of determining the orbit period and duration of each sun radiation stage. Figure 1.14 reveals that during the sun radiation stage there are a total of three faces exposed regularly, and since we have a percentage value we can add the

power of each face as presented in Table 1.6 to arrive at a total power of 2922 mW (X+, X-, Z+ or Z-) generated at any time during sun contact.

Table 1.6. Solar power generation per nanosatellite face

Face	Area under de curve	Percentage	Power (mW)
Sun pointing	42160	100%	2400
X+	2320	5.5%	132
X-	21507.4	51%	1224
Z+	27501.1	65.23%	1566
Z-	27501.1	65.23%	1566

(Source: own)

Technical features of the nanosatellites used in this study

Project PIMI-15-01 of the Escuela Politécnica Nacional contemplates the design and development of a nanosatellite, named after the university (BuhoSat) [16]. The California Polytechnic State University started the CubeSat program in 1999 to facilitate access to space for university students [44]. The CubeSats are nanosatellites (1 to 10 kg) whose shape are cubes. One unit is one cube of approximately 10 x 10 x 10 mm, and cubes can be staked to increase the overall size of the nanosatellite. The CubeSat program has design specifications [45] that need to be obeyed to qualify for space deployment opportunities. One such opportunity is deployment from the international space station (ISS) through the Japanese Experimental Module (JEM) small satellite orbital deployer (J-SSOD) [46]. Nanosatellites may be of other shapes and sizes, but that would present cost problems for launch opportunities. The CubeSat program has made space accessible for these smaller satellites by standardizing launchers that can go on traditional rockets. The common practice is to take CubeSats as a secondary payload on the rockets intended for bigger satellites. This reduces significantly the launch cost for the nanosatellite's developers and operators. Nevertheless, the drawback is that there is little choice of the type of orbit for the nanosatellite.

The CubeSat that is used in this study is one unit (1U) and is designed under CDS guidelines [CDS] [45] and J-SSOD integration requirements [J-SSOD] [46]. The overall components cost increased by approximately 5.5% to make it J-SSOD compatible, but this can generate saving in the launch costs [47]. The BuhoSat was designed for a main mission different than that of this study: to capture synchrotron emissions. However, the secondary mission uses an RGB camera; which is the focus of this study; in fact, the camera described

in section 1.1 is the one used in this design. The other main components of the BuhoSat can be seen in Figure 1.16 and are listed in Table 1.7. As it can be seen most of the components are COTS and come from the same manufacturer this was considered to improve the chances of success [47]. Table 1.8 summarizes the main design performance characteristics that are used as inputs in the models created. It is important to note that the maximum power available is a combination of the solar panels with the battery power.

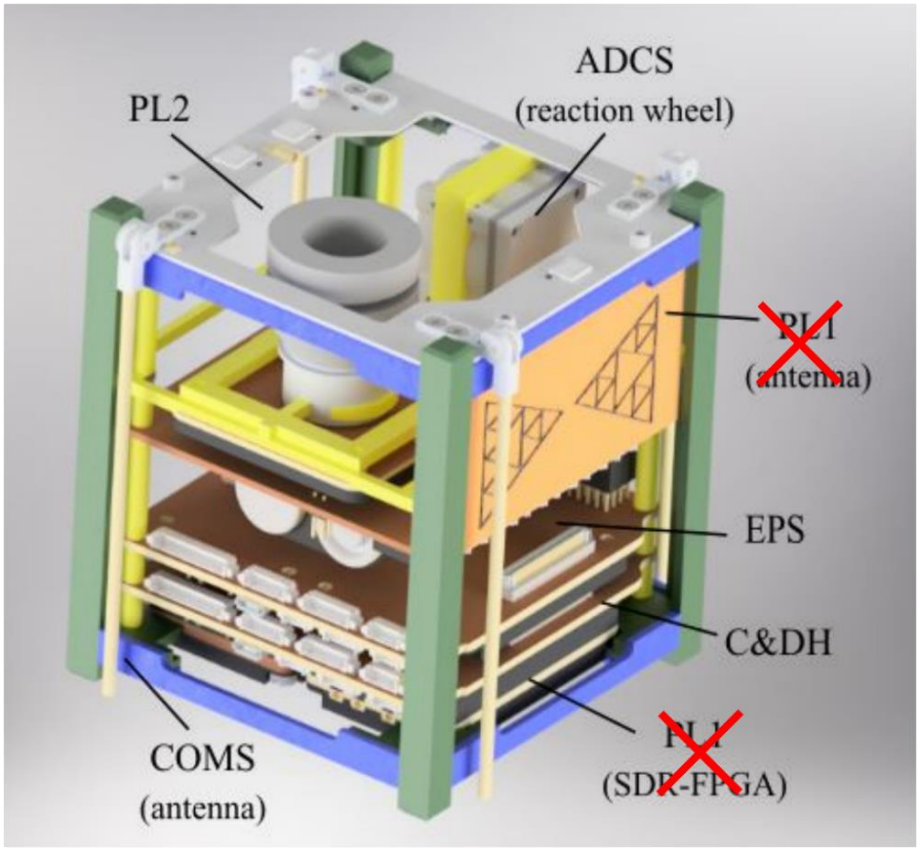

Figure 1.16. BuhoSat conceptual design; PL1 is not considered in the thesis
(Source: Reference [47])

Table 1.7. Nanosatellite components

Main Component	Sub-Components	
	Component name	**Provider**
Structure and Mechanisms (S&M)	- Main Structure - Internal Structure	Local
	- Antenna release - Deployment switches - Remove before flight pin	GOMspace
Thermal Control (ThC)	- Batter heater (active) - Heat/EMI shield (passive)	GOMspace

	- Mylar (passive) - Apiezon grease (passive) -Teflon covered glass/polyamide plate for the z+ face cover (passive)	Local
Electric Power System (EPS)	- Solar panels - Battery cell - PCB module	GOMspace
Communication System (COMS)	- PCB module - Antenna	GOMspace
Attitude Determination and Control (ADCS)	- Coarse sun sensors - Gyroscope Magnetometer - Magnetic Torquers	GOMspace
	- Reaction wheel	Cube Space
Scientific Payload (PL1)	- FPGA module	GOMspace
	- Antenna	Local
Secondary Payload (PL2)	- PCB module - Detector - Collector	GOMspace
Command and data handling (C & DH)	- Main PCB module - Monitoring sensors - Interfaces	GOMspace

(Source: Reference [47])

Table 1.8. Nanosatellite main design parameters

Parameter	Value	Unit
Mass	1.05	Kg
Structure mass	0.303	Kg
Structure mass ratio	28.86	%
Available power from solar panels	2922 (see section 2.5)	mW
Voltage from solar panels	4.74 V	
Power buses	3.3 V @ 5A 5 V @ 4A 8.4 V @ 4A (V-BAT)	V
V-BAT (raw battery voltage)	8.4	V
P31U power module Voltage output	3.3 5 8.4	V
Battery capacity	2600	mAh

Battery current charge at 3.7 V	1000	mA
Battery current discharge at 3.7 V	1000	mA

(Source: Reference [16])

The following table summarizes the power requirements for each component. This information is used to determine the overall power consumption and power requirement per orbit as discussed in the methodology section.

Table 1.9. Nanosatellite component power requirements

Component	Voltage (V)	Power (W)
Battery heater	8.4	3
EPS module	3.3	0.16
Magnetorquer	3.3	0.162
Reaction wheel	8.4	0.12
Camera (boot)	3.3	1.3
Camera (idle)	3.3	0.38
Camera (op)	3.3	1.65
Main computer	3.3	0.37
Interface PCB	3.3	0.132
Electric knifes	3.3	3.528
Antenna	3.3	0.6
Comm module (Rx)	3.3	0.182
Comm module (Tx)	3.3	2.64

(Source: Reference [16])

1.4. Fixed wing UAV

For the UAV concepts, this work builds on the research done by the ATA group from the mechanical engineering department at Escuela Politécnica Nacional. Specifically, on the work for UAV preliminary design for site specific management, SSM [48]. The main objective of this work is to arrive at a preliminary design of a UAV tailored for specific tasks and environments. The successful sizing of an aircraft requires a good trade-off between a variety of properties such as weight, aero-dynamics, performance, mechanical behavior and propulsion [48],Figure 1.17. This trade-off study is carried out using a constraint analysis

using the wing loading (W/S) and thrust to weight to power ratio (W/P) as the main boundaries that help define the design starting point [48]. The models require initial parameters to operate correctly, given in Table 1.10.

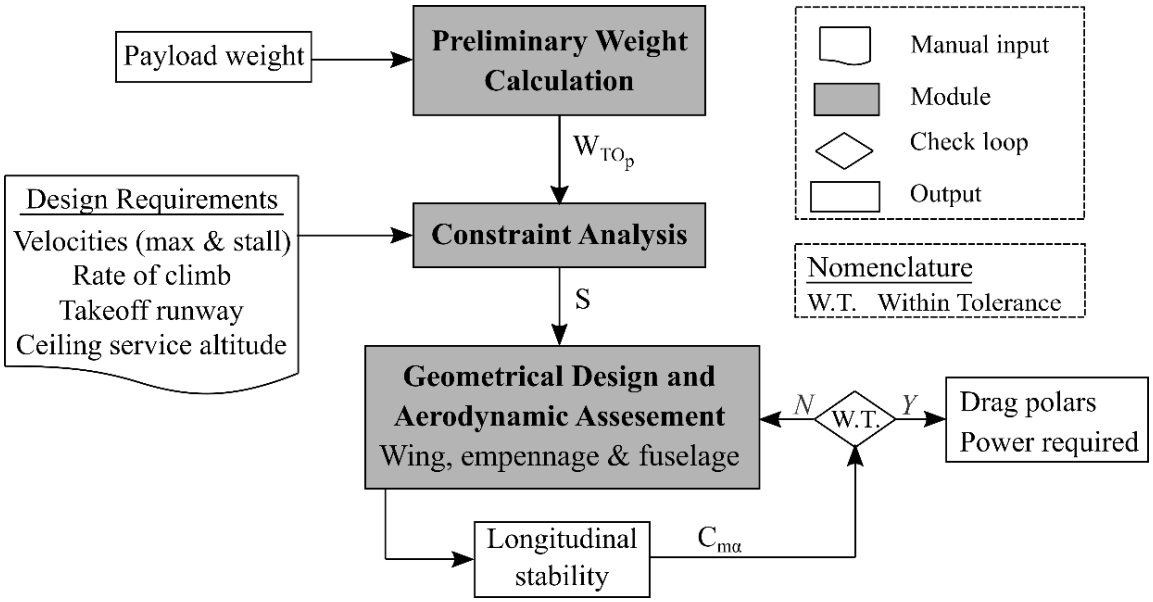

Figure 1.17. UAV weight, geometry and aerodynamic assessment models
(Source: Reference [48])

Table 1.10. Initial parameters for the UAV geometry and aerodynamic assessment models

Geometry	Wing	Stabilizer	Rudder
Mac (m)	0.25	-	-
AR	8.5	2.8	1.6
λ	1	1	0.6
$\Lambda_{c/4}$	0	0	14
Volume coefficient	-	0.7	0.035

(Source: Reference [48])

Geometry, weight, and aerodynamic properties

The methodology proposed by Valencia et al [48] uses as the starting point the preliminary weight calculation using semi-empirical correlations for a battery powered fixed wing UAV (1.4.1), using as sole input the mass of the payload. Then, the geometrical and aerodynamic parameters are determined by means of parametric models that require initial preliminary inputs. Reference [49] propose a model to calculate the Lift coefficient with a correction factor based on actual aircraft data (1.4.2). Where, the weight is determined using the

preliminary take-off mass (M_{TO}). Furthermore, equation (1.4.2) can be used to determine the wing planform area (S) in an interactive way as explained in the methodology section. Furthermore, reference [50] provides the equations for the tail preliminary sizing, used in this study (1.4.3), (1.4.4), and (1.4.5). K_c is a correction factor to the assumption that aft fuselage length is equal to that of the tail arm and was set to 1.1 [50]. Furthermore, to ensure the longitudinal stability, it was verified that the resulting C_{m_α} in equation (1.4.6) is between -0.3 and -1.5. This is a function of the stabilizer setting angle, which is modified until a matching is obtained [48].

$$m_{TO} = 5.147\, m_p^{0.849} \tag{1.4.1}$$

$$C_L = \frac{2W}{\rho V^2 S\, 0.855} \tag{1.4.2}$$

$$l_o = K_c \sqrt{\frac{4macSV_H}{\pi D_f}} \tag{1.4.3}$$

$$S_h = \frac{macSV_H}{l_o} \tag{1.4.4}$$

$$S_v = \frac{bSV_V}{l_o} \tag{1.4.5}$$

$$C_{m_\alpha} = C_{L_{\alpha,w}}(h - h_o) - C_{L_{\alpha,h}} \eta_h \left(\frac{S_h}{S}\right)\left(\frac{l_o}{mac} - h\right)\left(1 - \frac{2C_{L_\alpha}}{\pi AR}\right) \tag{1.4.6}$$

Where,

$$C_{L_\alpha} = \frac{C_{l_\alpha}}{1 + \frac{C_{l_\alpha}}{\pi AR}} \tag{1.4.7}$$

In addition, it is necessary to characterize to calculate the required thrust needed to fly at the required speeds. There are four main types of drag that add up to the total drag: Induced, interference, friction, and wave. However, in the cases presented in this work the wave drag is ignored since it is negligible at low speeds, i.e. subsonic flight (M<0.3). The induced drag is a direct result of the generated lift by the lifting surfaces (wings and tail), given by equation (1.4.8), were e_o represents the Oswald efficiency factor [50]. The friction drag refers to the friction of air with respect to the skin of the aircraft, for these three main parts of the aircraft were analyzed: wing, tail, (1.4.10) and fuselage (1.4.11). The friction coefficient depends on the Reynolds number, (1,4.12) where, L represents the fuselage length or the mac in the case of the wing and tail. The friction coefficient is given by equation

(1.4.13) for the case of turbulent flow and equation (1.4.14) for the case of laminar flow, [51]. Additionally, the thickness to chord form factor is given by equation (1.4.15), while the fuselage fitness ratio by equation (1.4.16). Finally, the Mach number correction is given by equation (1.4.17), [51].

$$C_{Di} = \frac{C_L^2}{\pi A R e_o} \tag{1.4.8}$$

$$e_o = 1.78(1 - 0.045AR^{0.68}) - 0.64 \tag{1.4.9}$$

$$C_{D_{ff_{w,t}}} = C_{f_{w,t}} f_{tc_{w,t}} f_M \left(\frac{S_{wet_{w,t}}}{S}\right)\left(\frac{C_{d_{min_{w,t}}}}{0.004}\right)^{0.4} \tag{1.4.10}$$

$$C_{D_{of}} = C_f \lambda_{LD} f_M \frac{S_{wet_f}}{S} \tag{1.4.11}$$

$$Re = \frac{\rho V L}{\mu} \tag{1.4.12}$$

$$C_f = \frac{0.455}{[log_{10}(Re)]^{2.58}} \tag{1.4.13}$$

$$C_f = \frac{1.327}{\sqrt{Re}} \tag{1.4.14}$$

$$f_{tc} = 1 + 2.7\left(\frac{t}{c}\right)_{max} + 100\left(\frac{t}{c}\right)^4_{max} \tag{1.4.15}$$

$$\lambda_{LD} = 1 + \frac{60}{\left(L_f/D_f\right)^3} + 0.0025\left(\frac{L_f}{D_f}\right) \tag{1.4.16}$$

$$f_M = 1 - 0.08M^{1.45} \tag{1.4.17}$$

On the other hand, interference drag, refers to the drag generated by the change of flow from one component such as the fuselage to that of the wing. This work only takes into account wing-fuselage, and tail-fuselage interactions to calculate the interference drag of the aircraft. To calculate this type of drag interpolation techniques are primarily used, using coefficients from models developed by Tétrault and Hoerner [50]. The interpolation is performed using the thickness to chord ratios of the required airfoils [50].

Fixed Wing UAV power requirements

This thesis follows the work by [52], [48] and [53]. The total power required is divided in two subsections, avionics and propulsion (1.5.7). The total power required by the avionics and payload can be determined using the equations presented for the weather balloon. On the other hand, the power required by the propulsion system (ps) is given by equation (1.4.22). From this the range can be calculated using equation (1.5.8) and the endurance (flight duration) from equation (1.5.10). The specific power of the battery ($\hat{P}$) depends on the selected cells for the propulsion system; which, depends on the available weight for batteries after preliminary design.

$$P_{aft} = P_{es} + P_{ps} \tag{1.5.7}$$

$$R = 3.6\frac{Vm_{bat}\hat{P}}{P_{bat}} \tag{1.5.8}$$

Where,

$$P_{bat} = \frac{P_{aft}}{\eta_{ps}} \tag{1.5.9}$$

$$E = \frac{R}{V} \tag{1.5.10}$$

Furthermore, it is important to estimate an adequate rate of descent (ROD) to better assert the real time that the UAV has to collect data. For this a good rule used by pilots is presented in equation (1.5.11); which, includes the conversion factors to get the answer in m/s. The formula takes in consideration the ground speed in nautical miles per hour (GS), which is determined together with the flight speed and the wind speed; nevertheless, to simplify and since this work is preliminary it only uses the flight speed for reference.

$$ROD = 0.0254\,GS \tag{1.5.11}$$

The propulsion system used in the fixed wing UAV presented in this work is fully electrical using batteries as the energy source and an electric motor to drive the propeller that provides the thrust to operate the UAV at the desired speeds. The thrust required can be related to the power required using a simple relationship of the flight speed and the propeller efficiency, namely equation (1.4.18) [53]. The flight velocity can be calculated using equation (1.4.19), using the 2D CL results obtained from XFOIL [54]. Lift and drag are calculated with equations (1.4.20) and 1.4.21) respectively. While the power required can

be calculated from equation (1.4.22). Next section discusses how the total power consumption is determined. The power required is needed to determine the two main performance characteristics that are used in this study: range and endurance that are also discussed in the power and energy section.

$$T = \frac{P\eta_p}{V} \tag{1.4.18}$$

$$V = \frac{\sqrt{2W}}{S\rho C_L} \tag{1.4.19}$$

$$L = \frac{1}{2}\rho V^2 S C_L \tag{1.4.20}$$

$$D = \frac{C_D}{C_L} W \tag{1.4.21}$$

$$P_{Req} = \frac{W\sqrt{(2WC_D^2}}{S\rho C_L^3} \tag{1.4.22}$$

The preliminary weight calculation plays a fundamental part in the propulsion system components selection such as the electric motor, propeller and battery cells. After determining the weight of the other components of the aircraft, the difference between m_{TO} and the aircraft components give the maximum weight for the propulsion system. Furthermore, the electric motor selection needs to be according to the propeller selection and the propeller selection is influenced by the operation altitude. For the electric motor and propeller selection a database is generally used and a matching can be done using the methodology proposed by reference [53].The remaining available weight is reserved for the battery cells. If there is more available weight then the UAV may have more cells, as discussed latter on.

Technical features of the fixed wing UAV used in this study

The work done by ATA for fix wing UAVs support preliminary design for specific site management [48]. This section presents some of the results obtained from running the models as described in section 2.4. This is necessary to mention now since they form part of the information needed to carry out the technoeconomic analysis presented in the results section. In this context, there are three design cases for specific altitudes that are considered in this thesis: sea level, high altitude, and altitude for Quito and its surroundings.

Nevertheless, Figure 1.18 shows the UAV conceptual design, the models presented in the methodology section latter on in the thesis are used to determine the corresponding dimensions for the lifting surfaces presented in Table 1.11, using the theory previously presented. The fuselage for all three cases has the same diameter of 0.10 m, enough to house the payload analyzed in this work. Furthermore, Table 1.12 shows the main components of the weight breakdown for the preliminary design of each case. The structure weight ratio is 0.304 for UAV A, 0.370 for UAV B, and 0.399 for UAV C. The weight of the propulsion system is given after selecting into components by running the propulsion power model to go through databases to select the electric motor and propeller combinations. The payload weight includes the same gimbal (230 grams) used for the weather balloon to ensure better image acquisition. The size and number of battery cells is determined after determining the available weight by adding all the other components.

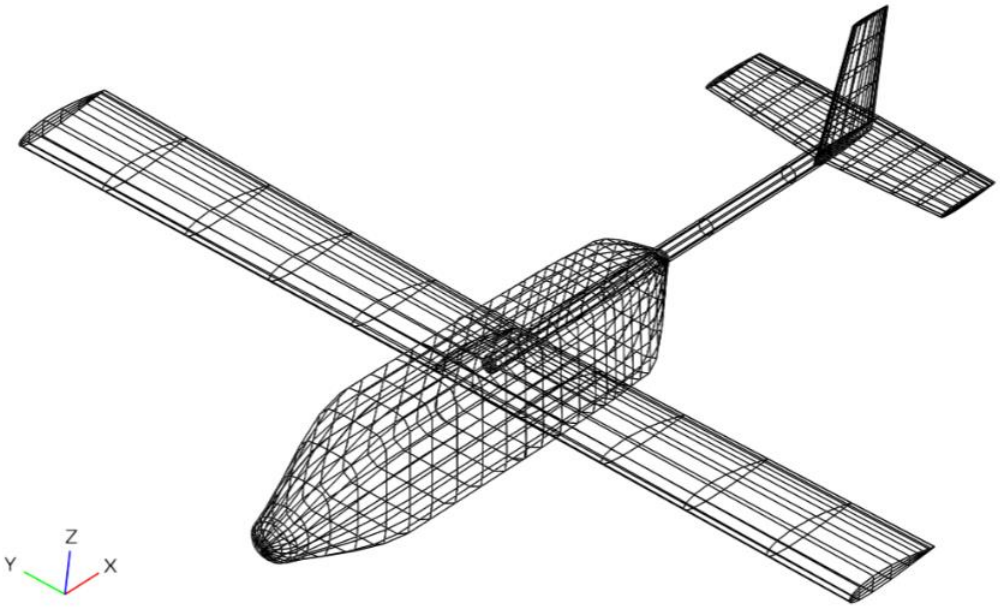

Figure 1.18. UAV conceptual design
(Source: Reference [48])

Table 1.11. Geometrical parameters of the UAV conceptual designs

Parameter	UAV A	UAV B	UAV C
Wing			
S (m^2)	0.4256	0.5264	0.5715
b (m)	1.9020	2.1152	2.2040
mac (m)	0.2238	0.2489	0.2593
Setting angle	1.2	1.6	1.8
AR	8.5	8.5	8.5
tr	1	1	1

LE	0	0	0
Airfoil	SD7032	Eppler 214	Eppler 214
Horizontal tail			
S (m^2)	0.0658	0.0771	0.0821
b (m)	0.6105	0.6612	0.6819
mac (m)	0.1077	0.1167	0.1203
Setting angle	-0.2255	-0.3671	-0.1705
AR	5.6667	5.6667	5.6667
tr	1	1	1
LE	0	0	0
Airfoil	NACA 0009	NACA 0009	NACA 0009
Vertical tail			
S (m^2)	0.0280	0.0328	0.0349
b (m)	0.2115	0.2290	0.2362
mac (m)	0.1322	0.1432	0.1476
Setting angle	N/A	N/A	N/A
AR	1.6	1.6	1.6
tr	0.6	0.6	0.6
LE	14.0362	14.0362	14.0362
Airfoil	NACA 0009	NACA 0009	NACA 0009
Fuselage			
Diameter	0.1	0.1	0.1
Length	0.7601	0.8914	0.9481

(Source: own, Reference [55])

Table 1.12. UAV conceptual designs weight breakdown by main components

Component	UAV A	UAV B	UAV C
Fuselage (grams)	145	170	181
Wing (grams)	437	541	587
Horizontal tail (grams)	25	30	32
Vertical tail (grams)	12	14	14
Propeller (grams)	15	20	20
Motor (grams)	108	107	107
ESC (grams)	50	50	50
Avionics (grams)	120	120	120
Camera with gimbal (grams)	336	336	336
Battery max weight (grams)	791	651	592
Total (grams)	2039	2039	2039

(Source: own, Reference [55])

The electric motor selected is the same model with slight variations for each UAV case. The propulsion system components with their corresponding main parameters for each case scenario are given in Table 1.13. Notice that the model selected a different propeller size for each case scenario due to the operating altitude. The propulsion system together with the electronic components are used to determine the power requirements of the fixed wing UAV using the information from Table 1.14.

Table 1.13. Propulsion system

Parameter	UAV A	UAV B	UAV C
Electric Motor: AT 2814 long Shaft (version Kv 900 for A) and (Kv 1050 for B & C)			
Max power (W)	650	700	700
Peak Current (A)	45	50	50
Rated Voltage (V) (3-4 S)	(11.1-14.8 V)	(11.1-14.8 V)	(11.1-14.8 V)
Idle Current (A)	1.2	1.5	1.5
Internal Resistance ($m\Omega$)	82	35	35
Kv (RPM/V)	900	1050	1050
Propeller: carbon fiber material			
Size (in)	11x5	11x7	12x6
Battery: Zippy compact (A), Turnigy High Capacity (B), Zippy (C)			
Voltage (V)	14.8	14.8	14.8
Capacity (mAh)	8000	6600	5800
Weight (g)	740	598	562
$\hat{P}$ (W/kg)	400	400	400

(Source: own, References [56] [57] [58] [55])

Table 1.14. Parameters used in the fixed wing UAV power requirements calculation

Component	Function	Response time (s)	Power Rating (W)
Avionics	Control and command	~	16
RGB Camera	Boot	15	1.3
	Idle	~	0.38
	Image acquisition	5	0.8
	Image processing	10	0.8
	Computation (other)	~	0.85

(Source: References [18] [59])

1.5. Life Cycle Costs

The life cycle cost (LCC) estimation for each aerospace platform used in this study follows the method and criteria from Roskam [9]. He created a series of estimation models based on real data compiled from several civilian, military and experimental aircraft programs. These models are adapted to fit the study platforms as shown in this study; however, the fundamental concepts are kept intact. These criteria follow an aerospace program of six phases [9], Figure 1.19. There are four main cost groups that add to the overall life cycle cost (1.7.1):

- Research, development, test and evaluation (RDTE)
- Acquisition (ACQ)
- Operation (OPS)
- Disposal (DISP)

$$LCC = C_{RDTE} + C_{ACQ} + C_{OPS} + C_{DISP} \tag{1.7.1}$$

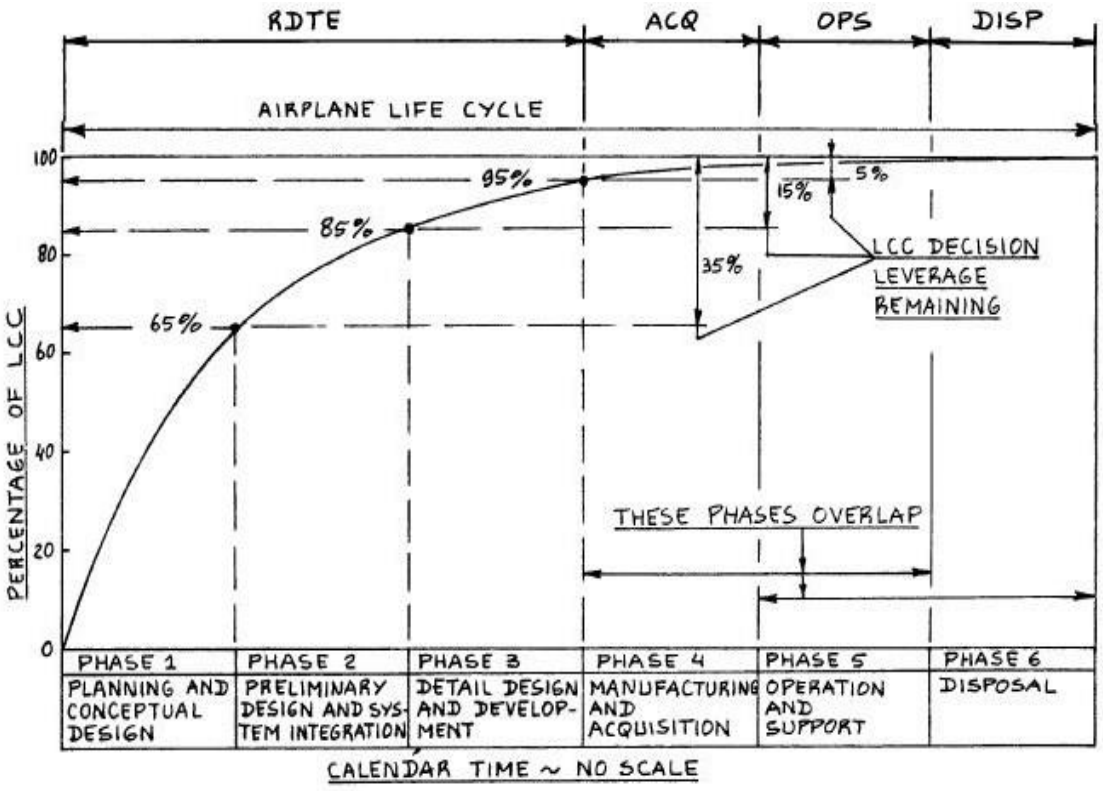

Figure 1.19. Aerospace program with six phases
(Source: Reference [9])

Research, development, test, and evaluation cost

This cost covers phase 1 through 3 of aerospace programs and there are 7 main categories to consider:

$$C_{RDTE} = C_{ed_r} + C_{dst_r} + C_{tp_r} + C_{to_r} + C_{tsf_r} + C_{pro_r} + C_{fin_r} \quad (1.7.2)$$

1. Engineering and design (C_{ed_r})

This refers to all the cost associated with planning, concept development, preliminary design and system integration studies, mock-ups and models, design of test facilities, detailed design and development, drawings with specifications, and administration costs. Roskam [9] proposes a function to calculate the total engineering man hour (MHR_{ed_r}) required using the aeronautical manufacturers planning report weight (W_{AMPR}) (1.7.3). The AMPR weight relates the structural weight to the rest of the components, a higher component weight will reflect in a lower man hour rating. The reason for this is because components are assumed to be bought directly from a manufacturer and not designed or built. Equation (1.7.3) also incorporates a propulsion complexity component measured with the maximum velocity rating, the number of units created during this phase (including for static and fly testing), a difficulty factor between 1 and 2 with 2 being the highest difficulty, and a CAD factor between 0.8 and 1.2 depending on the CAD skill of the people involved, with less being better. Finally, the engineering and design cost is given by multiplying the resulting (MHR_{ed_r}) to the engineering man hour rate (R_{e_r}), (1.7.4).

$$MHR_{ed_r} = 0.0396(W_{AMPR})^{0.791}(V_{max})^{1.526}(N_{rdte})^{0.183}\left(F_{diff}\right)(F_{cad}) \quad (1.7.3)$$

$$C_{ed_r} = MHR_{ed_r}R_{ed_r} \quad (1.7.4)$$

2. Development, support and testing (C_{dst_r})

This refers to physical tests performed on ground and to different components such as system testing, structural testing, propulsion testing, and simulation. This cost can be estimated with the following function were CEF is the cost escalation factor. The data that was used to create this function is from 1965 to 1988, so the correction factor is used based on the consumer price index [9]. Roskam´s models used a normalized CEF, setting the value of one (1) as the 1970 consumer price index. By taking into account the consumer price index of latter years [60] the CEF factor can be calculated for any given year after 1970, as shown in Figure 1.20.

$$C_{dst_r} = 0.008325(W_{AMPR})^{0.873}(V_{max})^{1.89}(N_{rdte})^{0.346}(CEF)\left(F_{diff}\right) \quad (1.7.5)$$

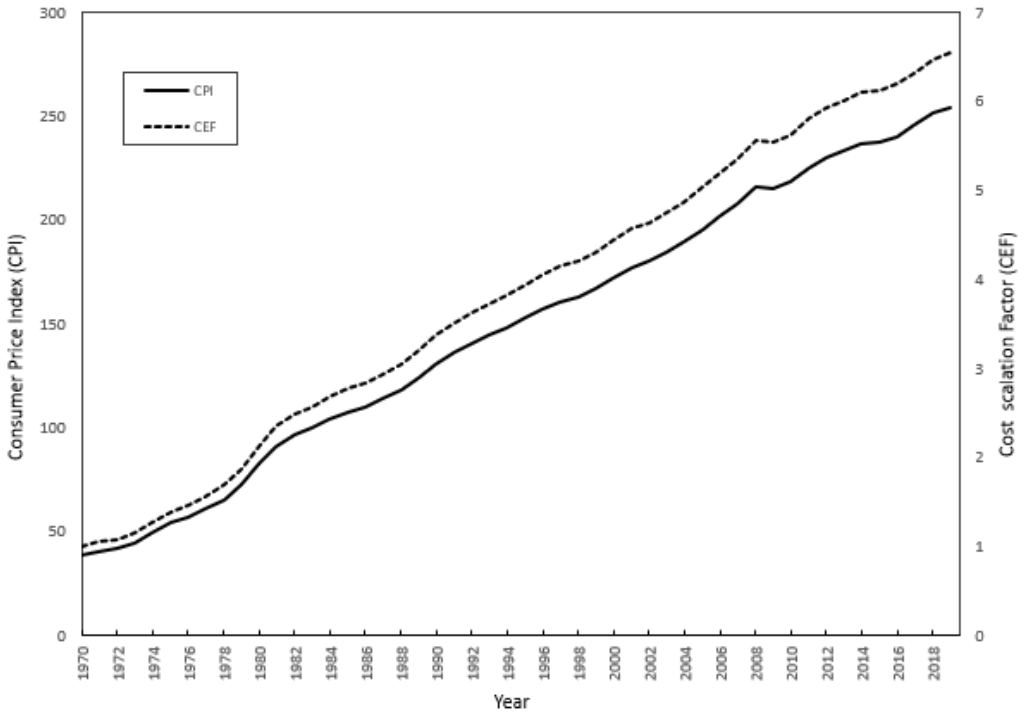

Figure 1.20. CEF according to consumer price index
(Source: own)

3. Test prototypes (C_{tp_r})

This cost refers to the components, manufacturing labor, materials, tooling costs, and quality control costs required to make a fly ready prototype (1.7.6). The manufacturing labor costs can be calculated by multiplying the manufacturing man hours for this phase with the manufacturing rate (1.7.7), where the MHR_{man_r} is given by (1.7.8). Tooling costs refer to the tooling of some components, given by multiplying the tooling man hour required with this labor rate (1.7.9). The quality control cost (C_{qc_r}) is generally 13 % of the manufacturing cost (C_{man_r}) [9].

$$C_{tp_r} = C_{comp_r} + C_{man_r} + C_{mat_r} + C_{tool_r} + C_{qc_r} \quad (1.7.6)$$

$$C_{man_r} = MHR_{man_r} R_{man_r} \quad (1.7.7)$$

$$MHR_{man_r} = 28.984(W_{AMPR})^{0.740}(V_{max})^{0.543}(N_{rdte})^{0.524}(F_{diff}) \quad (1.7.8)$$

$$C_{tool_r} = MHR_{tool_r} R_{tool_r} \quad (1.7.9)$$

$$MHR_{tool_r} = 4.0127(W_{AMPR})^{0.764}(V_{max})^{0.899}(N_{rdte})^{0.178}(N_{r_r})(F_{diff}) \quad (1.7.10)$$

4. Test operation (C_{to_r})

This includes actual physical tests and simulation costs, given by equation (1.7.11), which only considers the fly-capable units. As previously mentioned, N_{rdte} includes all prototypes created during RDTE, static and fly capable.

$$C_{to_r} = 0.001244(W_{AMPR})^{1.16}(V_{max})^{1.371}(N_{rdte} - N_{st})^{1.281}(CEF)(F_{diff}) \quad (1.7.11)$$

5. Test and simulation facilities (C_{tsf_r})

Test and simulation facilities cost are additional costs associated to the building of new test facilities and or specialized test equipment. There is not enough data to predict this type of costs so the project manager should estimate this cost through the facility adjustment factor,F_{tsf}, (1.7.12). The recommended factor rage is 0 if no extra facilities are required to 0.2 if there is a need for extensive testing and simulation.

$$C_{tsf_r} = F_{tsf} C_{RDTE} \quad (1.7.12)$$

6. RDTE profit (C_{pro_r})

Generally, RDTE activities are performed thinking on a profit margin, especially if a for-profit organization is involved. This cost incorporates the concept of profit margin into the overall cost equation.

$$C_{pro_r} = PM_r \, C_{RDTE} \quad (1.7.13)$$

7. RDTE financing (C_{fin_r})

Some aerospace program require financing. This cost incorporates the concept of a financing expense factor, F_{fin_r}. This factor includes concepts outside the scope of this research such as payment terms, interest rates, amount of loan etc. so it will be ignored in the case studies but is included as theory for completeness.

$$C_{fin_r} = F_{fin_r} C_{RDTE} \tag{1.7.14}$$

Manufacturing and Acquisition cost

The acquisition cost is incurred during phase 4, figure 1.18. It contemplates the manufacturing cost C_{man_a} plus the profit C_{pro_a}. The profit margin depends of many factors not covered in this research, but an arbitrarily profit margin may be used, (1.7.13). The manufacturing cost has three main components (1.7.17). One, the engineering and design cost associated to the manufacturing phase such as engineering work for problems uncovered during phase 1 to 3, design changes, manuals and any other engineering support during the program, (1.7.18). The engineering man hours during this phase is calculated with equation (1.7.3), using the total number of vehicles produced during the program $N_{program}$, which includes the fly capable vehicles included in the RDTE cost and all units created during phase four. Two, program production cost (C_{pp_a}), including cost of components, materials, tooling, labor cost, and quality control (1.7.19). To determine the manufacturing cost (1.7.20), the manufacturing man hours needs to be calculated using equation (1.7.8) with $N_{program}$ instead of N_{rtde}. Similarly, the tooling cost (1.7.21), uses the tooling labor cost, equation (1.7.10) with $N_{program}$ instead of N_{rtde}. Third, the finance cost is included if there is a loan associated with the production.

$$C_{ACQ} = C_{man_a} + C_{pro_a} \tag{1.7.15}$$

$$C_{pro_a} = PM_a C_{man_a} \tag{1.7.16}$$

$$C_{man_a} = C_{ed_a} + C_{pp_a} + C_{fin_a} \tag{1.7.17}$$

$$C_{ed_a} = MHR_{ed_p} R_{ed_p} - C_{ed_r} \tag{1.7.18}$$

$$C_{pp_a} = C_{comp_a} + C_{man_p} + C_{mat_a} + C_{tool_a} + C_{qc_a} \tag{1.7.19}$$

$$C_{man_p} = MHR_{man_p} R_{man_p} - C_{mam_r} \tag{1.7.20}$$

$$C_{tool_a} = MHR_{tool_p} R_{tool_p} - C_{mam_r} \tag{1.7.21}$$

Operational cost

Roskam's methodology enters into a lot of detail for commercial and military aircraft [9]; nevertheless, the main cost components proposed are used in this study since the three platforms being compared vary significantly in terms of operation. There are two types of operational cost, direct and indirect. For this study indirect costs will not be considered. Direct cost has five components expressed in USD/km eq: flight cots (DOC_{flt}), maintenance (DOC_{maint}), depreciation (DOC_{dpr}), fees and taxes (DOC_{f-t}), and financing (DOC_{fin}). The flight cost includes items like fuel, oil and other consumables for power, pilot or operator wages, and insurance. The cost for maintenance includes labor cost, materials and spare parts. The depreciation cost needs as input the life span of the vehicle the initial cost per unit and the perceived salvage value at the end of its life (1.7.23). The fees and taxes refer to any air and or space usage taxes or fees, frequency fees, airport usage fees, etc. that may need to be paid to operate the aerospace vehicle. The finance cost represents any financing expense in case of loans.

$$DOC = DOC_{flt} + DOC_{maint} + DOC_{dpr} + DOC_{f-t} + DOC_{fin} \tag{1.7.22}$$

$$DOC_{dpr} = P_{unit} - P_{salvage} \tag{1.7.23}$$

$$P_{unit} = \frac{C_{RDTE}+C_{ACQ}}{N_{program}-N_{rdte}} \tag{1.7.24}$$

Disposal cost

The end of life of an aerospace vehicle may be due to damage beyond repairs or because it has reached the end of its useful life. These vehicles incur an additional cost known as disposal, and considers items like temporary storage, disposal of toxic materials and liquids, disassembly, recycling, environmental considerations, etc. This cost is complex to predict and so when appropriate this research uses the proposed factor [9].

$$C_{DISP} = 0.01(LCC) \tag{1.7.25.}$$

2. METHODOLOGY

2.1. Overview

As previously mentioned, this work looks into three different aerospace platforms to compare their overall performance and life cycle cost using as the basis of the study the collection of data with an RGB camera. To do this there are four main parameters that are considered as shown in Figure 2.1: flight autonomy, area of operation, cargo capacity and life cycle cost. Flight autonomy refers to the platform's capacity for prolonged flight, generally related to time airborne. As shown in the figure this depends on the energy source (i.e. power available and power required to perform its mission and sustain flight). The straight forward method to determine this is to know by means of modeling the orbit in case of a nanosatellite, the trajectory in case of a weather balloon and the flight envelope for the UAV. The flight envelop can be determined from the weight (geometry) of the UAV and by evaluating aerodynamic and propulsion performance. Furthermore, these models are also helpful for determining the area of operation for each platform, since this can be a determining factor when selecting a platform for specific missions. The other parameter to consider is the cargo capacity, which depends on the design specification of each platform, but is heavily influenced by de desired flight autonomy and area of operation. Finally, the life-cycle cost of each platform needs to consider the whole program according to the mission.

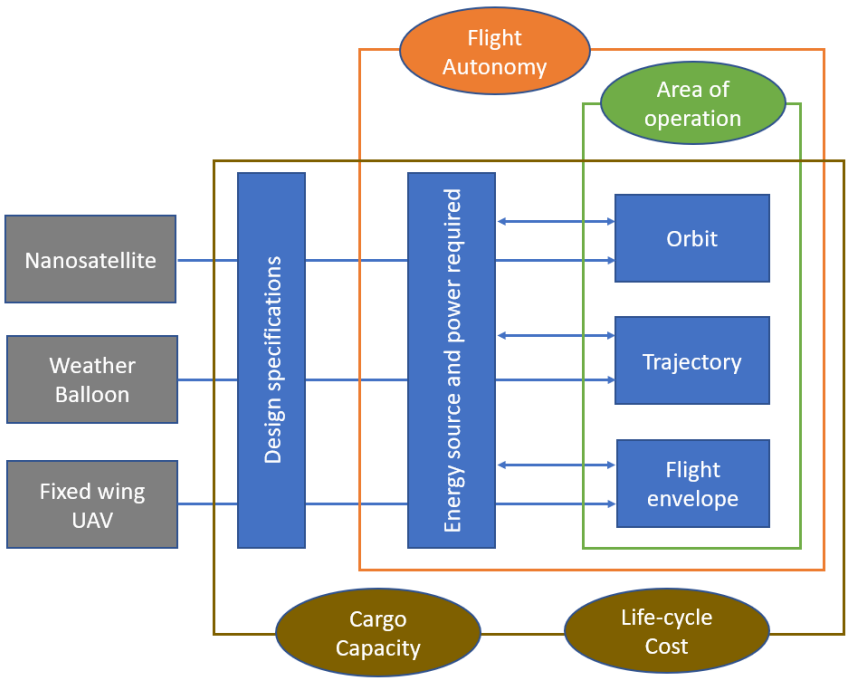

Figure 2.1. Methodology overview
(Source: own)

2.2. Weather balloons

Weather balloon dynamics

The balloon trajectory simulations use the theory presented in section 1.2 and are done with MATLAB. The simulations implement four separate models in a logical and sequential manner as illustrated in Figure 2.2. The vertical drag of the balloon system is calculated internally in the vertical dynamics model while other parameters required by the model are calculated with 3 custom functions using the theory presented in section 1.2 and a standard MATLAB function to call on the COESA 1976 atmosphere model [27]. This model is in the space domain; therefore, calculates all the parameters as a function of altitude. The main parameters that come out of this model are the vertical velocity, acceleration and forces; and, the flight time of the balloon to the simulated altitude. The parameters introduced in Table 2.2 (mass of the system and the lower limit of the burst altitude) were used as initial conditions of the vertical dynamics model to determine the three scenarios in this study together.

The horizontal dynamics model uses 3 custom functions and a standard MATLAB function to call on the horizontal wind model HWM model [28]. This model changes the space domain into the time domain using the flight duration calculated from the vertical dynamics model. The HWM determines the u and v components of the wind velocity as a function of time with one second intervals using the altitude time relationship determined form the vertical dynamics model. The relative wind functions determine the x and y components of relative wind as seen by the balloon. The drag function uses these results to determine the corresponding drag, which, is used to determine the acceleration using equation (1.2.3). The initial conditions for this model are the same as for the vertical dynamics model with the launch day and time, which is needed by the HWM model. The results are the horizontal velocity, acceleration, and distance as a function of time.

The building block for the two dynamics models are the basic equations of motion (2.1.1) (2.1.2). Where initial conditions for distance and velocity are set to zero. The initial acceleration in the vertical direction is given by equation (1.2.1), and in the horizontal direction by equation (1.2.8). The acceleration is key to calculate the corresponding velocities and distances as X, Y, and Z components. Since the model needs to calculate for the distance in reference from the origin; the distance with the corresponding place index needs to be added throughout the model. The distance components are then used to plot the trajectories as presented in the results section.

$$\delta d_i = d_i + Ve_i(t) + \frac{1}{2} acc_i(t^2) \quad (2.1.1)$$

$$\delta Ve_i = Ve_i + acc_i(t) \quad (2.1.2)$$

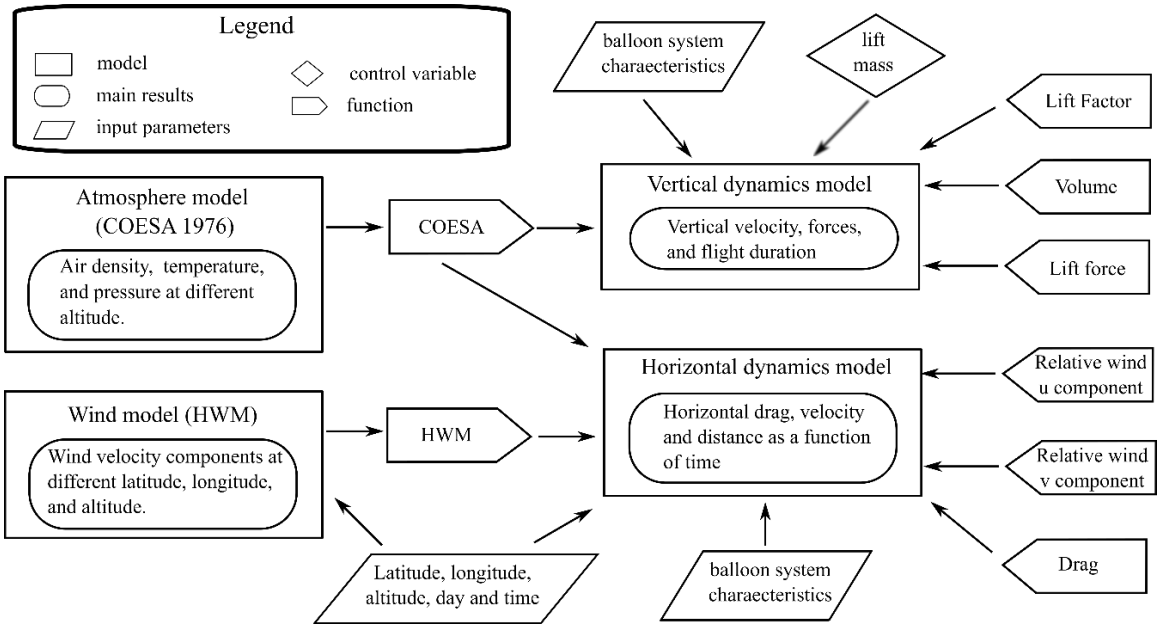

Figure 2.2. Model overview for the balloon trajectory simulation
(Source: own)

The model was validated by comparing the trajectory using two proven balloon trajectory predictors with their corresponding validation. One predictor was developed by Cambridge University in the UK, and named after their space flight program, CUSF [23]. It is one of the most commonly used predictors [61] and it uses a flight dynamics model as its basis, requiring some user input to run. The other model was developed by the University of Southampton in the UK as well, named as ASTRA [22]. ASTRA is a stochastic model based on empirical data from thousands of radiosonde flights [22]. Furthermore, it uses mote Carlo simulation to add an unpredictability factor for changing conditions that may take place along the balloon flight. Additionally, the vertical solutions can be checked with the HAS calculator [31]; which, is based on their performance assessment from their experience and actual flight data. In fact, this calculator was used to determine the burst altitude of each balloon according to the applied lift force and payload weight. Table 2.2, also shows input parameters used for the validation case, based on a weather balloon that was launched the same day of the simulation by the OAQ team. Unfortunately, the balloon was lost because of a communication failure with the ground station.

Energy and power requirements

Table 1.4 in section 1.2 show the main parameters used to calculate the power consumption using the theory previously presented. Annex A shows an example of how the energy required per flight was determined. A maximum power consumption case was also calculated to show the case scenario when the sensors are used at their maximum availability depending on their response and processing time. The Power supply provided by the batteries is 5.4 V for all components and is used to calculate the current used per hour, equation (1.5.2). Then the current per hour is latter changed back to amps by multiplying the flight duration in hours and equation (1.5.3) is used to determine the battery life. There are four strategies listed below that were used for this study.

1. MAX: the system uses full power all the time, number of samples depend on the response time of the sensor to collect and process the data.
2. High rate: high number of samples by collecting sensor data every 5 seconds and camera data every 15 seconds up to 2 km and then every 30 seconds after.
3. Mid rate: high number of samples by collecting sensor data every 10 seconds and camera data every 30 seconds up to 2 km and then every 60 seconds after.
4. Low rate: high number of samples by collecting sensor data every 15 seconds and camera data every 60 seconds up to 2 km and then every 300 seconds after.

2.3. Nanosatellite orbit simulations

Orbit dynamics

Orbit simulation of the nanosatellite is used to gather important geolocation data of the satellite along its orbit. It also allows the modeling of communication windows between the satellite and the ground station. Furthermore, it is also useful to simulate the periods of umbra (total darkness) and penumbra (partial darkness) during the orbit, which is important for the satellite power model. The program used to create these models is The General Mission Analysis Tool (GMAT) created by the National Aeronautics and Space Administration (NASA) on open source principles and written with C++ code [62]. It is a complicated system that takes a divide and conquer approach that uses simple components that combine to satisfy the needs of the system [62]. The elements of the model can be broken into four sub-packages, Figure 2.3:

- Environment: this sub-package provides all the background environmental data to model the solar system.
- Resources: are the model elements that do not require sequential ordering, and some can be personalized by the user.
- Commands: are the model elements that require sequential ordering and describe how the model should evolve over time according to the user´s needs.
- Parameters: are variables, arrays, or strings used to perform calculations of data useful for analysis purposes.

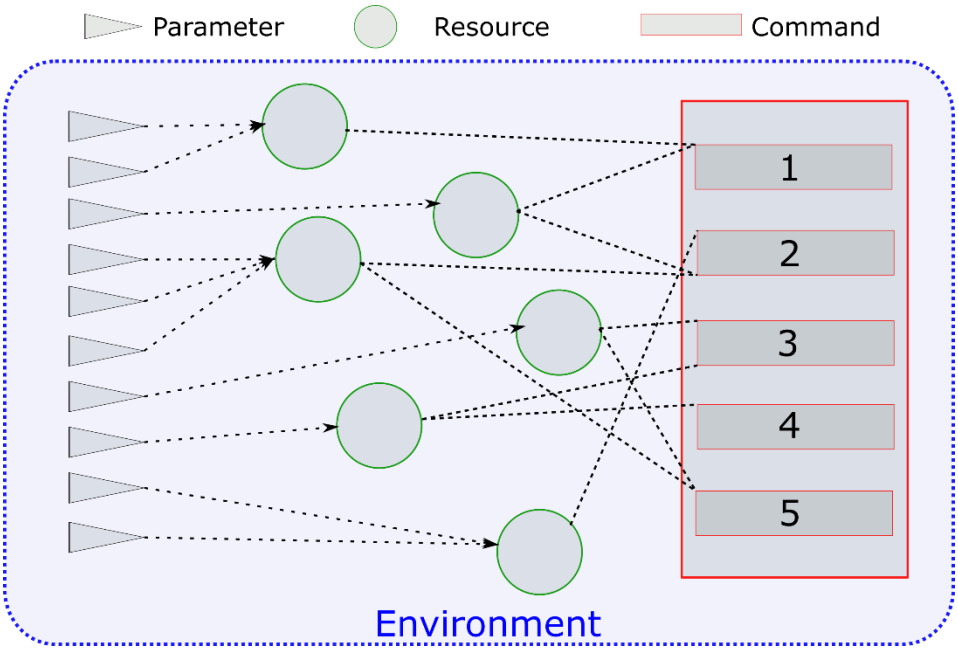

Figure 2.3. GMAT Architecture
(Source: own)

The model can be generated using the graphical user interface (GUI) or through the script interface. Both have their strengths and weaknesses and there are some aspects that can only be done in one of them; Nevertheless, they are interconnected, and a script can be created from the GUI commands and vice versa. The first step is to create or pick all the resources that will be used in the model. For a complete list of resources please refer to the GMAT user guide [43]. Annex B lists the resources and their corresponding parameters used in the orbital models created for this study. There are three orbits simulated for this study: Orbit A, is modeled according to the J-SSOD deployment parameters; Orbit B is modeled for an altitude to allow at least one year in orbit; and Orbit C is modeled at the same altitude as Orbit B, but at a near equatorial inclination. The next step is to create the commands that are needed to generate models and run the simulation, also in annex B.

An important parameter to consider is the download time required for the images since communication from the ground station to the nanosatellite depends on the orbit position. GMAT can model the contact times and duration using the ground station and the nanosatellite parameters described in Table 1.8. There are two preferred image formats: JPEG that has a compression rate of 10% and BMP with a 3 Bytes compression (One third of the raw image) [16]. The time that it takes to download these images is considered in this study as discussed latter on. For now, it is important to mention that one of the main outputs for the orbit models is the contact locator mentioned in annex B.

GMAT is considered a high-fidelity program used by NASA extensively for the design and optimization of space missions. It has gone through a rigorous verification and validation campaign with a team of 10 scientist and engineers lasting 18 months [63]. Furthermore, it has gone through several operational certification milestones to obtain the operational certification need to be used in maneuver planning of currently flying NASA missions such as the Advance Composition Explorer (ACE), launched in 1997 [64]. The verification and validation campaign started in 2012, 5 years after GMAT was available as beta software; since then versions 2013A and forward are considered high-fidelity space mission planning tools [63]. All the GMAT architecture, models, solvers, and artifacts in general were rigorously tested against other high-fidelity software such as STK and real data presenting really good congruence and results [63].

Energy and power requirements

As mentioned in section 1.3, there are two main power sources for the nanosatellite: the solar panels and the battery. For the case of the battery a similar calculation as the balloon can be done to determine current consumption and consequent battery life. Nevertheless, the solar panels add complexity to this otherwise straight forward calculation using the theory presented before. As previously mentioned, GMAT can be used to simulate each orbit scenario and can also be used to model the amount of sunlight that the nanosatellite receives as a function of distance from the sun. For the purpose of this analysis the standard GMAT solar function was used.

There are four operation modes considered in this study: initial, navigation, data, and communication. Soon after the nanosatellite is deployed it will turn on in a semi-navigation mode (No ADCS and COM) until fully charging the batteries. The initial mode marks the start of the satellite mission and it is performed after the batteries are fully charged. The

navigation mode refers to the regular flight control, monitoring and sending of telemetry data. It is recommended that the nanosatellite send status reports often even though it is not at the ground station proximity; every 5 minutes was picked for this purpose. Telemetry takes 0.4 minutes at 56 kbps to download; this comes into play to determine the power required per orbit [16]. The battery heaters are recommended to keep nominal operational temperature of the EPS. The umbra time according to [42] (36.64% of the total orbit) was considered for this calculation. The data acquisition mode refers to the operation of the RGB camera for capturing images. Images are heavy files and require time to download. The suggested formats are JPEG that weight approximately 607 KB and BMP weighting 2024 KB, having download times of 1.45 and 4.82 minutes respectively at 56 kbps [16]. Finally, the communication mode refers to stablishing contact with the ground station to send all the data.

The power and energy requirement are done as a per period basis. This is done to analyze how charge and discharge of the batteries behave during each orbit. For all cases of study there are 5 specific orbits to analyze: Initial power-on, non-collection and non-contact, non-collection and contact, collection and contact with JPG, collection and contact with BMP. The source of the power is divided into solar panels and battery and a similar procedure as the one done to calculate the energy consumption of the balloon was performed, but using the orbit period not the entire flight duration. Annex C presents an example on how this was done. The following assumptions and analysis cases are considered:

1. The initial time to fully charge the batteries after deployment is ignored in all cases.
2. Components that require 8.4 Volts use battery power since the solar panels do not provide enough voltage.
3. When there is no sunlight, the energy comes from the battery in all modes (36.64% of the orbit period [42].To simplify the calculation the average duration of the period is considered for all cases.
4. The percentages presented in Table 2.4 are used to calculate the amount of time in seconds that a component is powered on or performing a specific task. That time is split between sunlight and darkness, annex C.
5. For all cases assume telemetry transmission every 5 minutes. During contacts with the ground station, telemetry will always be downloaded if the contact window allows. Refer to Table 3.2 in the results section to see contact windows.
6. During the communication mode the satellite will be set to receive signal (Rx) during all the contact window, while transmission (Tx) lasts the download time for the corresponding format previously mentioned, plus telemetry. If the transmission time

is longer that the average contact window the transmission time is used in all cases since the contact window was previously screened.

Finally, GMAT is used to gather data needed to analyze how much power from the solar panels is available to recharge the batteries. For this, the power required from solar panels is used in the GMAT model together with the power that the solar panels can generate, Table 1.6. The amount of current charged is a straightforward calculation using (equation 1.5.1) with the power that is not used by the nanosatellite for other operations.

2.4. UAV weight geometry, and aerodynamic assessment models

Geometry, weight, and aerodynamic assessment models

The fixed wing UAV models use the theory presented in section 1.4 and are done with MATLAB. As shown in Figure 1.17. the first model solves for the preliminary weight using equation 1.4.1, then a constraint analysis is done taking into consideration design requirements specific for the operation of the UAV, Table 2.5 in section 2.7. The results of this constrain analysis presented in Figure 3.16, section 3.3 are used in the next model. The geometrical design model and the aerodynamic assessment model use XFOIL [54] as part of their tools to arrive at the best conceptual geometry and airfoil selection in an interactive way until longitudinal stability is achieved as explained in the theory section. XFOIL is used to calculate the 2D drag polars, namely sectional drag polars using an airfoil database. The model runs XFOIL through the geometry of the UAV in an interactive way using the LLT methodology [48]. The result is the conceptual geometry that is most appropriate for each application, given in Table 1.11, section 1.4 and the corresponding airfoil derived from the aerodynamic assessment. Nevertheless, these models require initial parameters to run properly, they are listed in Table 1.10. Notice that the stabilizer and rudder use NACA0009 as their default airfoil following the recommendation from reference [48]. Furthermore, the stabilizer and the rudder volume coefficients are also given by reference [48].

After the geometry has been determined and the propulsion system has been selected the weight breakdown can be completed, the results are shown in Table 1.12, section 1.4. The weight break-down takes into account the main components of the UAV, using the information that is readily available from the manufacturer of each component. For the structural components the dimensions from Table 1.11 are used to determine the weight by assuming that the construction material is of EPS, balsa wood, and fabric composite

material with a combined density of 60 kg/m^3 [55]. For the avionics the PIXhawak 4 control module [59] was used along with corresponding servos to manipulate lifting surfaces, their combined weight is 120 grams [55]. Subtracting the conceptual preliminary weight previously determined by the weight of the other components a weight threshold for the batteries can be determined. This weigh in turn is used to select the battery size and number of cells that can be used for each concept, Table 1.13 in section 1.4.

Energy and power requirements

As mentioned in section 1.4 there are two main components that are analyzed separately to get the total power required by the UAV, equation (1.5.7). The power rating for the avionics and the payload are given by the manufacturers and their power consumption is calculated in a similar fashion as it was done for the weather balloon. The avionics power rating is 15 W [59], while the same power parameters of the RGB camera applies for the UAV as well. The total power requirement is then used to calculate the range and endurance of each UAV concept as previously explained. The same four collection cases were analyzed for the UAV: MAX (image every 15 seconds), high rate (image every 30 seconds), mid rate (image every 60 seconds), low rate (image every 300 seconds). The results are presented latter on.

2.5. Lifecycle costs estimation

There are a few considerations that need to be included in this section. Starting with the validation of the model presented in section 1.5. Since it was created and validated using data from the 60s to the 90s, the CEF value introduced in the same section is very important. Furthermore, the units used in the creation of the model were British so to avoid mistakes in the correlating formulas it is a better option to change all inputs to such units. Moreover, for the model to work correctly, the suggested AMPR weight is taken from a take-off weight range between 5000 lbs to 10^6 lbs, Figure 2.4. Consequently, a correction factor needs to be introduced to account for much smaller aerospace platforms, Annex D. For this correction factor the categorization of satellite sizes was used. In this context the four main categories for smaller than regular sized satellites are: Pico (0.1 to 1 kg), Nano (1 to 10 kg), Micro (10 to 100 kg) and small (100 to 500 kg) [40]. Additionally, the data used to create the model came from important programs that developed big military and commercial aircraft so there need to be a distinction with the other platforms when setting the variables criteria as described in tables Table 2.7Table 2.8Table 2.9.

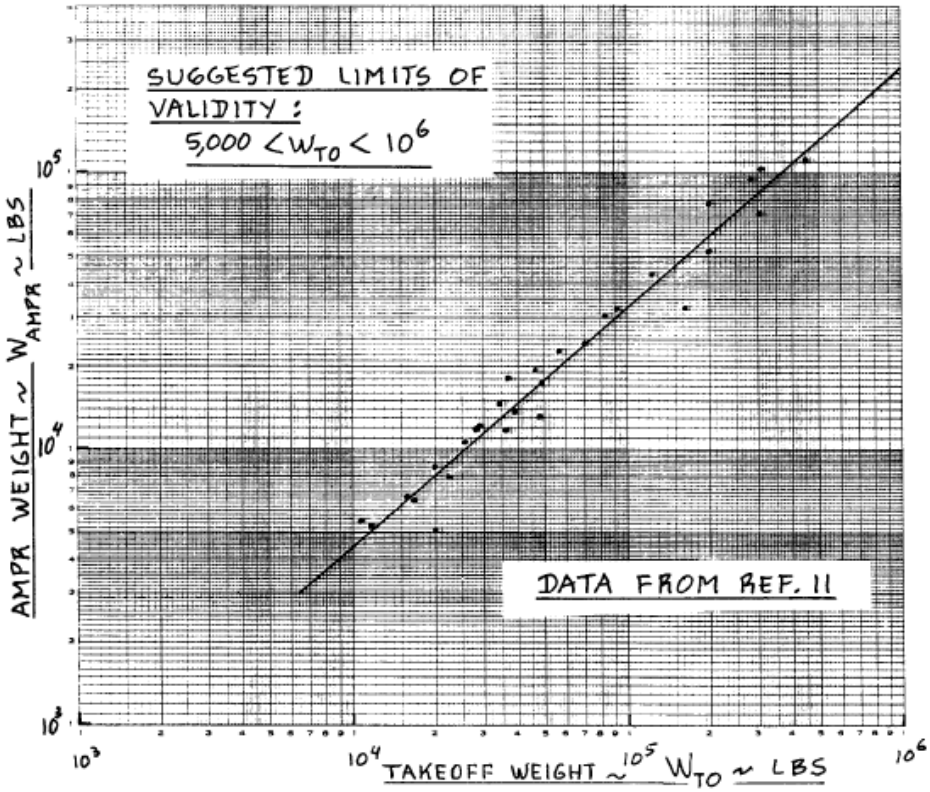

Figure 2.4. Data and trend line of AMPR weight as related to takeoff weight
(Source: Reference [9])

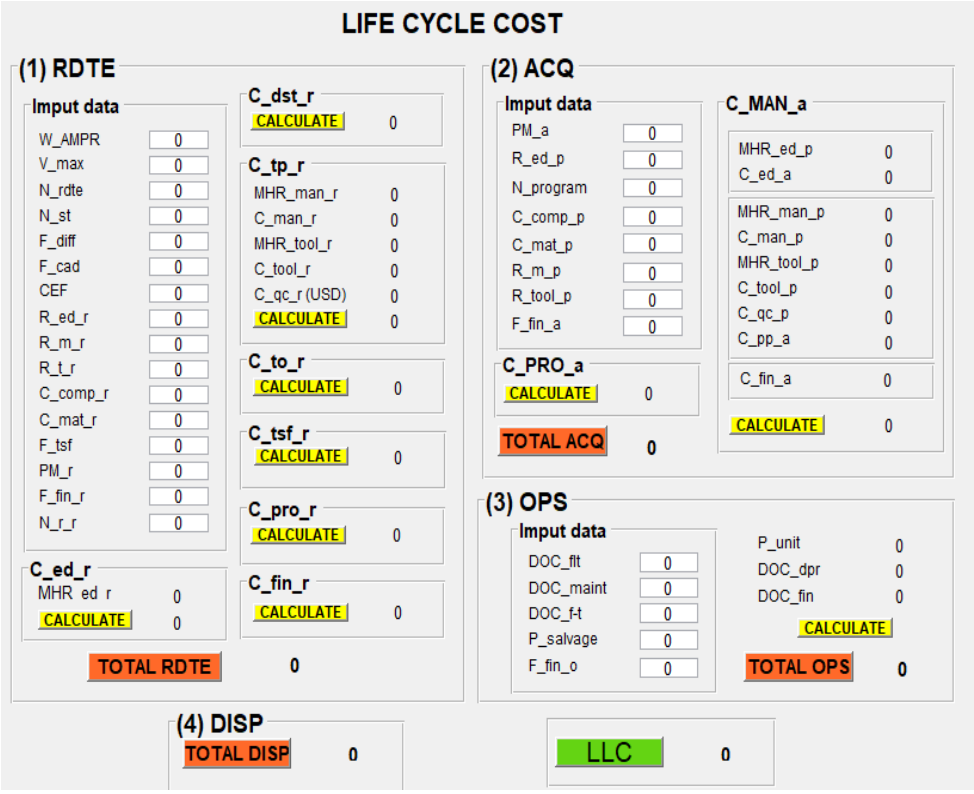

Figure 2.5. Life cycle cost calculator
(Source: own)

Figure 2.5 presents a lifecycle cost estimation tool that was created using the guide feature in MATLAB and the theory presented in section 1.5 and the AMPR correction factor previously discussed. To have a better representation of the recategorization of platform size the correction factor is introduced for the calculation of C_{edr}, C_{dstr}, and C_{tor}. The prototypes cost (C_{tpr}) did not use the correction factor since this cost reflects the manufacturing of the prototypes so the actual weight and size is important here. The other three costs involve engineering, office and laboratory use, human capital, and other operational related costs, so the weight and size of the aerospace platform in these cases is relative. Furthermore, to simplify the study and to have similar context for all three platforms is important to define the program as the operation of each platform for one year and to collect data at least one time each day, if possible. From this operation requirement point of view the number of platforms created will be evaluated independently. Furthermore, there are other considerations pertinent to each platform that will be addressed as well:

1. For weather balloons is important to consider that there is a risk that the probe will not be recovered. Ecuador has areas with limited road access and many mountain ranges, forests, and rivers. Additionally, the GPS installed in this weather balloon requires cellular connectivity to function properly adding an additional difficulty since cellular coverage is not complete. For, these main reasons the recovery rate of the probe has been set at 50%.

2. The nanosatellite will have to match the year of operation that has been stablished for all three systems. As previously shown, this requires a particular orbit that comes with a cost increase and fewer launch opportunities. Additionally, it is common practice in spacecraft development to build two identical copies to have one as backup on earth in case there is a need for software reprograming [41]. The two prototypes will also be the total number of platforms build for this program. One is developed during the RDTE phase while the second one during the ACQ phase.

3. For the UAV the main considerations are range and endurance. These parameters are key to determining how many UAVs are needed for a specific mission. The results presented latter on in the thesis suggest that two operational UAVs are enough if the user requires a full work day of data; however, due to the nature of environmental monitoring this is not the case and one UAV is enough. Nevertheless, the program contemplates 2 UAVs for each operating altitude discussed, for a total of 6 UAVs. The main reason for this is to always have an operational UAV in case one needs to be grounded.

2.6. Payload mission analysis

Section 1.1 provides the scientific background to perform the RGB camera payload analysis and contains the main technical specifications of the RGB camera system used for this study, Table 1.1 and Table 1.2. The calculations were done using MATLAB and the equations previously presented. The main variable that affects the camera performance is the object´s distance to the camera system since the payload is the same for all the platforms.

The spatial resolution will be the same using all the three platforms since this parameter is dependent on the technical features of the optical system only. Nevertheless, what comes into play is the ground sample distance achieved by all three platforms since it is very dependent on the objects distance to the camera in addition to the camera technical characteristics. The aperture of the camera and the wavelength of the visible light (red, blue, green, and near IR) are given in Table 2.1. The GSD as an angle is calculated for the corresponding object distance for all three platforms. The results are presented latter in this document.

Table 2.1. Camera aperture and visible light wavelength

Parameter	Value
D_A	25.5 mm
λ (Blue)	4.5 x 10^{-4} mm
λ (Green)	5.5 x 10^{-4} mm
λ (Red)	6.5 x 10^{-4} mm
λ (Near IR)	7.5 x 10^{-4} mm

(Source: own)

The spectral resolution for this study is very dependent on the cloud coverage so the information presented in Figure 1.2 is used to analyze the collection of useful data from a platform that is higher than 2 km. For distances higher than 2 km the percentage of sunlight can be used to estimate the final number of useful images collected by each platform. These results are cross-referenced with the other camera performance parameters. The temporal resolution is dependent on the preferred setting according to the camera system specifications, Table 1.2. Changing the windowing setting of the camera will reduce the number of pixels that were used to capture the image and consequently the resolution is also affected. However, a higher frame rate is useful to collect more samples that are needed for detecting movement. MATLAB was used to determine how the IFOV change

according to each setting. Furthermore, the sample time calculated from this step is used as input to calculate the duty cycle or samples per picture of the camera for the purpose of determining the ability to detect change.The radiometric resolution also changes according to the distance of the object from the camera. However, it is only necessary to use the altitude of the aerospace platform with respect to the ground to showcase how the emissivity of the object being captured decreases as the distance increases.

As previously mentioned, the main variable used to determine the above parameters needed for the payload analysis is the distance of the object to the camera system. For this reason, in the case of the balloon, Case B can be used for all calculations since it has the higher burst altitude, consequently covering all three cases. For the nanosatellite, Orbit B and C have the same altitude, while Orbit A does not; however, they all have the same end of orbit altitude of 100 km, so an altitude range can be used in the analysis. In the case of the UAV the data collection in done from a minimum altitude of 100 m to 200 m from the ground.

2.7. Study cases

Weather Balloons

The three cases introduced in section 1.2 were simulated using the MALAB models for the same launch day and location. Table 2.2 shows the input parameters used in the simulations. Additionally, case A was modeled several times with different launch dates (around the middle of each month of the year 2020), but same launch location to demonstrate the changing wind conditions and the unpredictability of balloon trajectory on any given day through the year. The lift mass is the additional mass added to the model to simulate the force of the helium due to buoyancy as explained in section 1.2.

Table 2.2. Input parameters for the balloon trajectory simulations

Parameter	Balloon A	Balloon B	Balloon C	Validation case
Latitude (º)	-0.2499	-0.2499	-0.2499	-0.2499
Longitude (º)	-78.5833	-78.5833	-78.5833	-78.5833
Altitude (m)	3050	3050	3050	3050
Day of year	10 (2020)	10 (2020)	10 (2020)	331 (2019)
Time (s) (UTC)	39600	39600	39600	39600
Total mass (kg)	2.136	2.386	2.589	1.596
Lift mass (kg)	0.214	0.203	0.427	0.319

Burst Altitude (m)	21940	27020	21380	22170

(Source: own)

Nanosatellites

The initial orbital elements of each of the orbits studied are presented in to following table. These parameters are basic to describe an orbit as explained in section 1.3, and they will change overtime as the lifespan of orbit progresses. These initial orbital elements were generated using the methodology presented previously, for more detail on the initial parameter, resources, and commands used, check annex B. The orbital elements for Orbit A are the ones right after the orbit has been achieved from the kibo impulse as described in section 2.3.

Table 2.3. Orbital elements for the three nanosatellite cases

Orbit Element	Orbit A	Orbit B	Orbit C
a (km)	6781.59	6832.77	6825.02
e	0.000932	0.001124	0.001259
i (º)	51.64	51.68	0.6622
Ω (º)	139.49	91.09	71.49
ω (º)	124.57	99.42	348.30
Θ (º)	182.86	299.67	310.41

(Source: own)

The workload of each component as a percentage during each of the four operation modes is used to calculate the total power requirement of the nanosatellite, Table 2.4. For the communication mode it is important to consider that there are three types of data as explained earlier; the first percentage from left to right reflect the time for telemetry, the second is JPEG, and at the third is BMP. Notice that in the case of the communication equipment the operation time adds since the telemetry is being sent every five minutes regardless if there is communication with the ground station or not. Nevertheless, there is only one picture per orbit either JPEG or BMP since there is only one change to be above the target, (in a collection orbit). The orbit simulation solution help determine what image format can be taken according to the contact window duration.

Table 2.4. Power requirements per nanosatellite operational mode

Component	Operation modes (%)			
	Initial	Navigation	Data	Communication
Battery heater	-	36.64	-	-

EPS module	-	100	-	-
Magnetorquer	-	100	-	-
Reaction wheel	-	100	-	-
Camera (boot)	0.27 0.26 0.27	-	-	-
Camera (idle)	-	100	-	-
Camera (op)	-	-	0.27 0.26 0.27	-
Main computer	-	100	-	-
Interface PCB	-	100	-	-
Electric knifes	0.02	-	-	-
Antenna	-	8	-	0.44, 1.59, 5.29 0.42, 1.54, 5.10 0.43, 1.54, 5.12
Comm module (Rx)	-	-	-	5.04 6.49 7.88
Comm module (Tx)	-	8	-	0.44, 1.59, 5.29 0.42, 1.54, 5.10 0.43, 1.54, 5.12

* Orbit A is in red, B is in blue and C is in orange
(Source: own)

Fixed wing UAV

Three cases of study are done for this thesis: sea level, Quito altitude, and high altitude. Table 2.5 present the input parameters used in the constraints model to determine the preliminary designs that best fit these cases. While, Table 2.6 shows the electronics power parameters used in the collection strategies previously stablished.

Table 2.5. UAV operational design requirements

Parameter	Minimum Value	Maximum Value
Payload mass (g) (RGB camera + 3-axis gimbal)	336	336
Stall speed (m/s)	6	8
Cruise speed (m/s)	12	16
Rate of climb (m/s)	1	3
Take-off runway (m)	10	30
Ceiling Case A (m) asl	100	200
Ceiling Case B (m) asl	2900	3000

Ceiling Case C (m) asl	4100	4200

(Source: own)

Table 2.6. Fixed wing UAV power operation rates per data collection strategy

Component	Power Rating (W)	Operation rate (%)	Power Required (W)
No Image			
Avionics	15	100	15
Payload	1.65	0	0
Max			
Avionics	15	100	15
Payload	1.65	100	1.65
High rate			
Avionics	15	100	15
Payload	1.65	87.16	1.44
Mid rate			
Avionics	15	100	15
Payload	1.65	80.81	1.33
Low rate			
Avionics	15	100	15
Payload	1.65	75.72	1.25

(Source: own)

Life cycle costs

The flowing tables present the parameters used in the study cases in the context of a one-year program as previously discussed.

Table 2.7. Balloon cost variables and selection criteria

Parameter	Value	Units	Selection criteria
RDTE			
W_{AMPR}	1.755	lbs	Calculated using the mass information from Table 1.3. Since the balloon different sizes adds no additional complexity to the system the probe´s mass is taken for this calculation
V_{max}	1	knots	There is no propulsion component for this system; therefore, the weight is one
N_{rdte}	2	#	Two prototypes are needed (based on the stablished recovery rate)
N_{st}	0	#	The same prototypes

F_{diff}	1	-	(Range: 1-2) This is easy difficulty
F_{cad}	1	-	(Range: 0.8-1.2) Average skill of the people involved
CEF	6.5	-	From Figure 1.20. CEF according to consumer price index for 2019
R_{ed_r}	5.88	USD/mhr	Based on the engineer salary at OAQ
R_{man_r}	5.88	USD/mhr	Based on the engineer salary at OAQ
R_{tool_r}	5.88	USD/mhr	Based on the engineer salary at OAQ
C_{comp_r}	Balloon A & C 1678.91 X 2 **3357.82** Balloon B 1742.34 X 2 **3484.68**	USD	This cost includes all the subcomponents of the system including the balloons and parachutes except for the materials and consumables needed for assembly and manufacture. Figure 1.7 shows the main electronic components for this system; the price is given by the provider. Annex E has more detail about the cost of each component. (For 2 prototypes)
C_{mat_r}	31,8 X 2 **63.6**	USD	The materials cost includes the aluminum tubes, EPS spheres, screws, connecting cables, nylon string, and PLA used for additive manufacturing. (For 2 prototypes)
F_{tsf}	0.01	-	(Range: 0-0.2) this factor takes into consideration the need for a ground station to receive the signal from the aerospace system
PM_r	0	%	There is no profit margin, since this is initially a nonprofit endeavor.
F_{fin_r}	0	%	There is no financing component to this cost
N_{r_r}	8	#/month	Assumed production rate
ACQ			
PM_a	0	%	There is no profit margin assumed for manufacturing
R_{ed_p}	5.88	USD/mhr	Based on the engineer salary at OAQ
$N_{program}$	183	#	Estimate based on the assumption that the probe will be lost every other day during the year.
C_{comp_a}	Balloon A & C 307,240.53 Balloon B 318,848.22	USD	The cost of the components in the RDTE phase times 183
C_{mat_a}	5819.40	USD	The cost of the materials in the RDTE phase times 183
R_{man_p}	5.88	USD/mhr	Based on the engineer salary at OAQ
R_{tool_p}	5.88	USD/mhr	Based on the engineer salary at OAQ

F_{fin_a}	0	%	There is no financing component to this cost
OPS			
DOC_{flt}	Balloon A 95,989.42	USD	(for the complete program) Assume the vertical flight distance and the amount of helium needed for each balloon. Includes the cost of 3 engineers: one for tracking and monitoring and two for preparation, launch, and search. The time required for remote tracking and monitoring is the flight time plus 20 mins for setup. The time required for preparation and launch including travel time is 2 hours and for search and recovery 4 hours plus the flight time (Annex E)
	Balloon B 106,711.20		
	Balloon C 98151.03		
DOC_{maint}	1949.44	USD	Maintenance needed includes one engineer cost for 2 hours per week plus 10% of the material cost for each flight. Additionally, a 10% of component cost is added to the DOC maintenance cost for the possible replacement of components. (Annex E)
DOC_{f-t}	0	USD	There is no taxes or fees expected for the operation of this system
$P_{salvage}$	0	USD	This assumes that all 183 weather balloons will be lost
F_{fin_o}	0	%	There is no financing component to this cost

(Source: own, Reference [65])

Table 2.8. Nanosatellite cost variables and selection criteria

Parameter	Value	Units	Selection criteria
RDTE			
W_{AMPR}	0.668	lb	Calculated using the mass information from Table 1.8.
V_{max}	1	knots	There is no propulsion component for this system
N_{rdte}	1	#	One prototype is needed
N_{st}	0	#	The same prototypes
F_{diff}	2	-	(Range: 1-2) This is hard difficulty by a factor of 10 for space
F_{cad}	1	-	(Range: 0.8-1.2) Average skill of the people involved
CEF	6.5	-	From Figure 1.20 for 2019
R_{ed_r}	5.88	USD/mhr	Based on the engineer salary at OAQ
R_{man_r}	5.88	USD/mhr	Based on the engineer salary at OAQ
R_{tool_r}	5.88	USD/mhr	Based on the engineer salary at OAQ

C_{comp_r}	Orbit A 86,900 Orbit B 82,120.50 Orbit C 82,120.50	USD	This cost includes all the subcomponents of the system except for the materials and consumables needed for assembly and manufacture. Figure 1.16 shows the main electronic components for this system; the price is given by the provider. Annex F has more detail about the cost of each component. A Deployment from the ISS has a cost increase of 5.5% of the components to make them ISS compliant.
C_{mat_r}	206.63	USD	The materials cost includes the aluminum for the structure, screws, PCB materials, grease, liquid Teflon, and mylar (Annex F)
F_{tsf}	0.2	-	(Range: 0-0.2) this factor takes into consideration the need for a ground station to receive the signal from the aerospace system. Additionally, a clean environment is needed for assembly and testing with an integration testbed. Furthermore, special certified laboratories are needed for prelaunch testing.
PM_r	0	%	There is no profit margin, since this is initially a nonprofit endeavor.
F_{fin_r}	0	%	There is no financing component to this cost
N_{r_r}	0.2	#/month	Assumed production rate of 1 every 5 months
ACQ			
PM_a	0	%	There is no profit margin assumed for manufacturing
R_{ed_p}	5.88	USD/mhr	Based on the engineer salary at OAQ
$N_{program}$	2	#	A typical satellite program has two operative systems including the prototype.
C_{comp_a}	Orbit A 86,900 Orbit B 82,120.50 Orbit C 82,120.50	USD	The cost of all the components for the additional nanosatellite
C_{mat_a}	206.63	USD	The cost of the materials for the additional nanosatellite
R_{man_p}	5.88	USD/mhr	Based on the engineer salary at OAQ
R_{tool_p}	5.88	USD/mhr	Based on the engineer salary at OAQ
F_{fin_a}	0	%	There is no financing component to this cost
OPS			
DOC_{flt}	Orbit A 3044.79 - 95544.79	USD	This cost includes the launch and deployment to orbit. And two engineers, one to monitor the communication daily (10 minutes before and after

	Orbit B 98953.63 Orbit C 110502.77		each orbital window), and the second one to analyze status telemetry daily (1 hour) and update orbit simulation. (Annex F)
DOC_{maint}	8937.60	USD	There is no maintenance needed. If an anomality occurs two engineers are needed to try to fix the problem within an estimated duration of 4 hours. Assume a 52% chance of anomality this means that 52% of the year there will be a need to fix an anomaly.
DOC_{f-t}	0	USD/km	There is no taxes or fees expected for the operation of this system
$P_{salvage}$	Orbit A 43,553.32 Orbit B 41,163.57 Orbit C 41,163.57	USD	Assumed 50% of the component and material value of the second satellite.
F_{fin_o}	0	%	There is no financing component to this cost

(Source: own Reference [16] [47] [66])

Table 2.9. Fixed wing UAV cost variables and selection criteria

Parameter	Value	Units	Selection criteria
RDTE			
W_{AMPR}	UAV A 1.365 UAV B 1.663 UAV C 1.795	lbs	Calculated using the mass information from Table 1.12. UAV type B will be used as the prototype since the production, and testing is assumed to be done near Quito.
V_{max}	31.1	knots	Upper limit for the constraint analysis operational speed. Entered as 1.311 in LCC calculator
N_{rdte}	1	#	One prototype is needed
N_{st}	2	#	Two static prototypes: one for wind tunnel testing, another for propulsion testing
F_{diff}	1.5	-	(Range: 1-2) This is average difficulty
F_{cad}	1	-	(Range: 0.8-1.2) Average skill of the people involved
CEF	6.5	-	From Figure 1.20 for 2019
R_{ed_r}	5.88	USD/mhr	Based on the engineer salary at OAQ
R_{man_r}	5.88	USD/mhr	Based on the engineer salary at OAQ

R_{tool_r}	5.88	USD/mhr	Based on the engineer salary at OAQ
C_{comp_r}	UAV A 2075.75 UAV B 2037.75 UAV C 2062.45	USD	This cost includes all the subcomponents of the system including the camera, except for the materials and consumables needed for assembly and manufacture. (UAV type B will be the prototype)
C_{mat_r}	UAV A 220.04 UAV B 265.93 UAV C 286.32	USD	The materials cost includes the balsa wood, EPS, fabric, screws, and epoxy.
F_{tsf}	0.1	-	(Range: 0-0.2) this factor takes into consideration the need for a ground station to receive the signal from the aerospace system. Additionally, it is required an operational wind tunnel and a propulsion test bed.
PM_r	0	%	There is no profit margin, since this is initially a nonprofit endeavor.
F_{fin_r}	0	%	There is no financing component to this cost
N_{r_r}	1	#/month	Assumed production rate of 1 every month
ACQ			
PM_a	0	%	There is no profit margin assumed for manufacturing
R_{ed_p}	5.88	USD/mhr	Based on the engineer salary at OAQ
$N_{program}$	6	#	A total of 6 UAVs are needed including the RDTE fly capable prototype
C_{comp_a}	UAV A 2075.75 x 1 UAV B 2037.75 x 2 UAV C 2062.45 x 2	USD	The cost of all the components for the additional UAVs (1 type A, 2 type B, and 2 type C) Enter the total in the LCC calculator (10276.15)
C_{mat_a}	UAV A 220.04 x 1 UAV B 265.93 x 2 UAV C 286.32 x 2	USD	The cost of the materials for the additional nanosatellite Enter the total in the LCC calculator (1324.54)

R_{man_p}	5.88	USD/mhr	Based on the engineer salary at OAQ
R_{tool_p}	5.88	USD/mhr	Based on the engineer salary at OAQ
F_{fin_a}	0	%	There is no financing component to this cost
OPS			
DOC_{flt}	UAV A 9331.66 UAV B 10439.98 UAV C 10047.82	USD	Assume the endurance without payload operation. Includes the cost of 3 engineers: one for tracking and monitoring and two for preparation, launch, and search. The time required for remote tracking and monitoring is the flight time plus 20 mins for setup. The time required for preparation and launch including travel time is 2 hours and for search and recovery 1 hours plus the flight time. (Annex G) Enter the total in the LCC calculator (29819.45)
DOC_{maint}	UAV A 967.969 UAV B 1029.55 UAB C 1056.91	USD	Maintenance needed includes one engineer cost for 2 hours per week plus 1% of the material cost for each flight. Additionally, a 10% of component cost is added to the DOC maintenance cost for the possible replacement of components. (Annex G) Enter the total in the LCC calculator (3054.43)
DOC_{f-t}	0	USD/	There is no taxes or fees expected for the operation of this system
$P_{salvage}$	UAV A 1721.84 UAV B 1727.76 UAV C 1761.58	USD	75% of original value of the components in one year (estimated useful life: 4 years) Enter the average in the LCC calculator (1737.06)
F_{fin_o}	0	%	There is no financing component to this cost

(Source: own)

3. RESULTS AND DISCUSSION

3.1. Balloon

As previously mentioned, there were three different balloon designs that were analyzed. All three balloons use the same probe; however, they use a different balloon size for the case of B with respect to A and more helium in the case of C also with respect to A. The results of the trajectory simulation show what was expected from theory: the bigger balloon drifts

further and had a burst altitude higher than the other two, Figure 3.1, with a longer flight duration, Table 3.1. On the other hand, C, with the same size balloon than A climbed faster because it used more helium; although, the helium increased the drag area by inflating more the balloon the vertical speed was significantly more so it drifted less than balloon A. Vertical speeds for all three cases plus the validation case mentioned in section 2.2 are shown in table. The table also compares the results with balloon calculator from reference [31]. As previously mentioned, the significant difference in helium volume comes from the use of the error introduced in section 1.2. Furthermore, the MATLAB balloon trajectory model was also compared with other high-fidelity simulators as mentioned in section 2.2 using the validation case, figure 3.2. It can be seen that all three simulations send the balloon in the same general direction with burst locations and altitudes close to each other. The ASTRA and CUSF simulations include a possible landing location, not included with the MATLAB simulation done for this work. Both ASTRA and CUSF have gone through their own verification as previously mentioned.

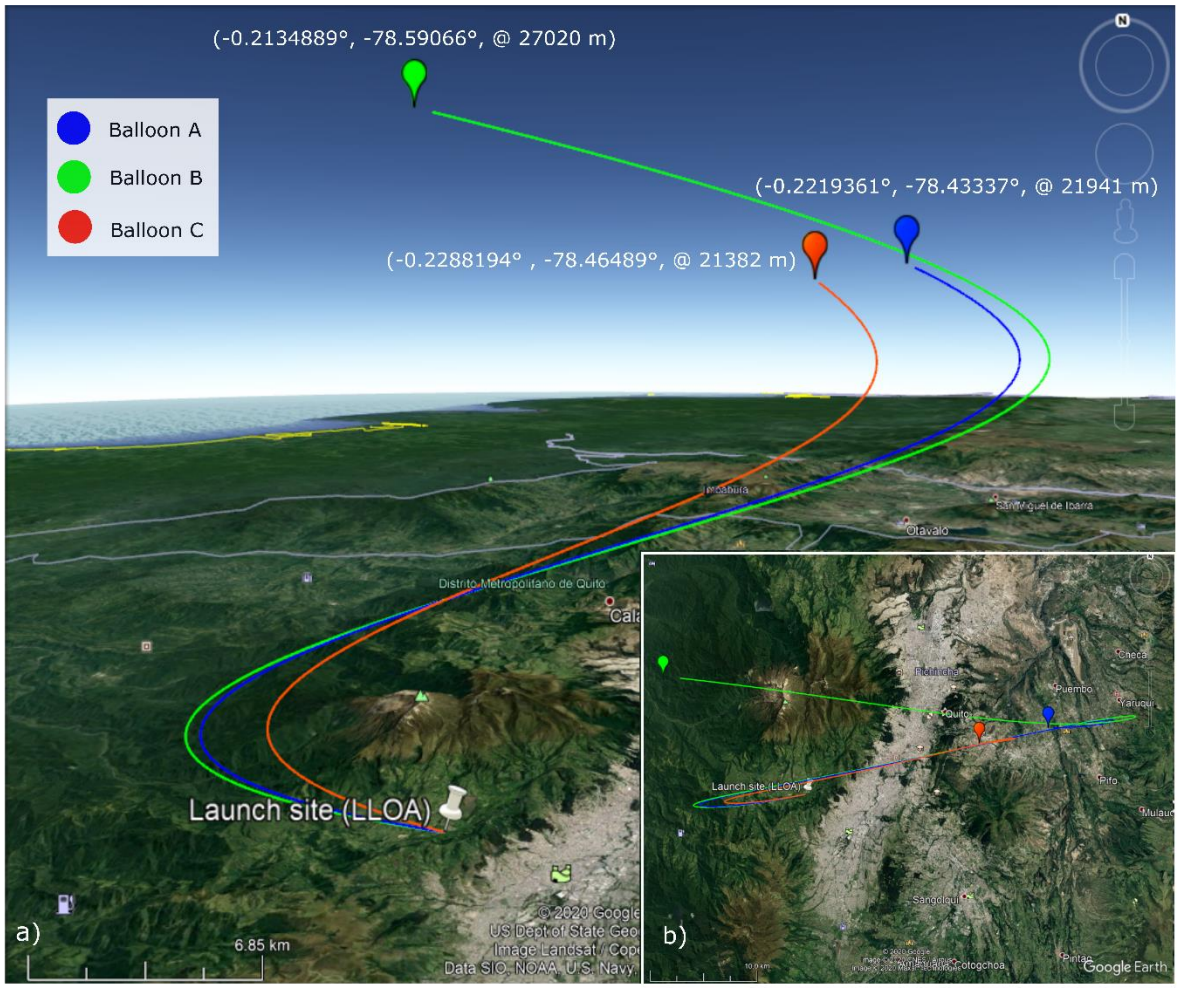

Figure 3.1. Overview of the trajectory for the balloon cases, a) side view, b) top view (Source: own)

Table 3.1. Trajectory simulation results and validation

Study case	HAS vertical *Ve* (m/s)	Model vertical *Ve* (m/s)	Dif (%)	HAS He (m^3)	Model He (m^3)	Dif (%)	Flight time (s)
Balloon A	2.512	2.4098	4.07	2.3913	2.7947	14.43	7840
Balloon B	2.368	2.4109	1.81	2.6345	3.0792	14.44	9943
Balloon C	3.455	3.2893	4.79	2.6091	3.0487	14.42	5574
Validation Case	3.116	3.1612	1.59	1.9461	2.2777	14.56	6049

(Source: own)

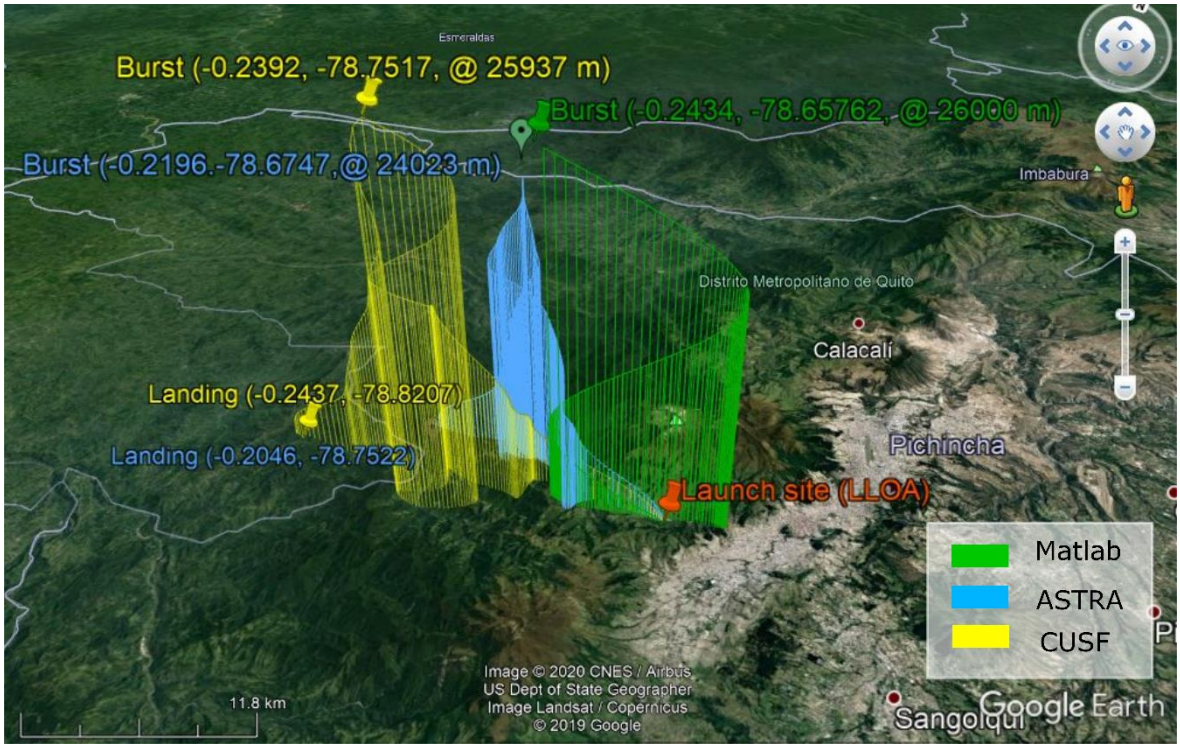

Figure 3.2. Trajectory simulation comparison with two other models
(Source: own)

The reliability of collecting data at a specific location is important for weather monitoring using an RGB camera. Knowing that a balloon has little control on the direction it will fly it is necessary to analyze how the constant changes throughout the year in wind direction and magnitude affect the balloon trajectory. For this, case A was modeled using wind data from reference [28] middle of each month of the year 2020. Figure shows the results by plotting the KML file of each trajectory using Google Earth. The wind generally has greater effect in the west-east direction as opposed to the north-south direction, Figure 3.3, with the wind pushing east early in the year and west letter in the year. Generally, the wind around Quito seems calm enough to not drift the balloon too far away from the launch site, about

40 km west or east. Nevertheless, the actual trajectory is hard to predict with certainty; making the balloon an unreliable choice if samples need to be collected at a specific site.

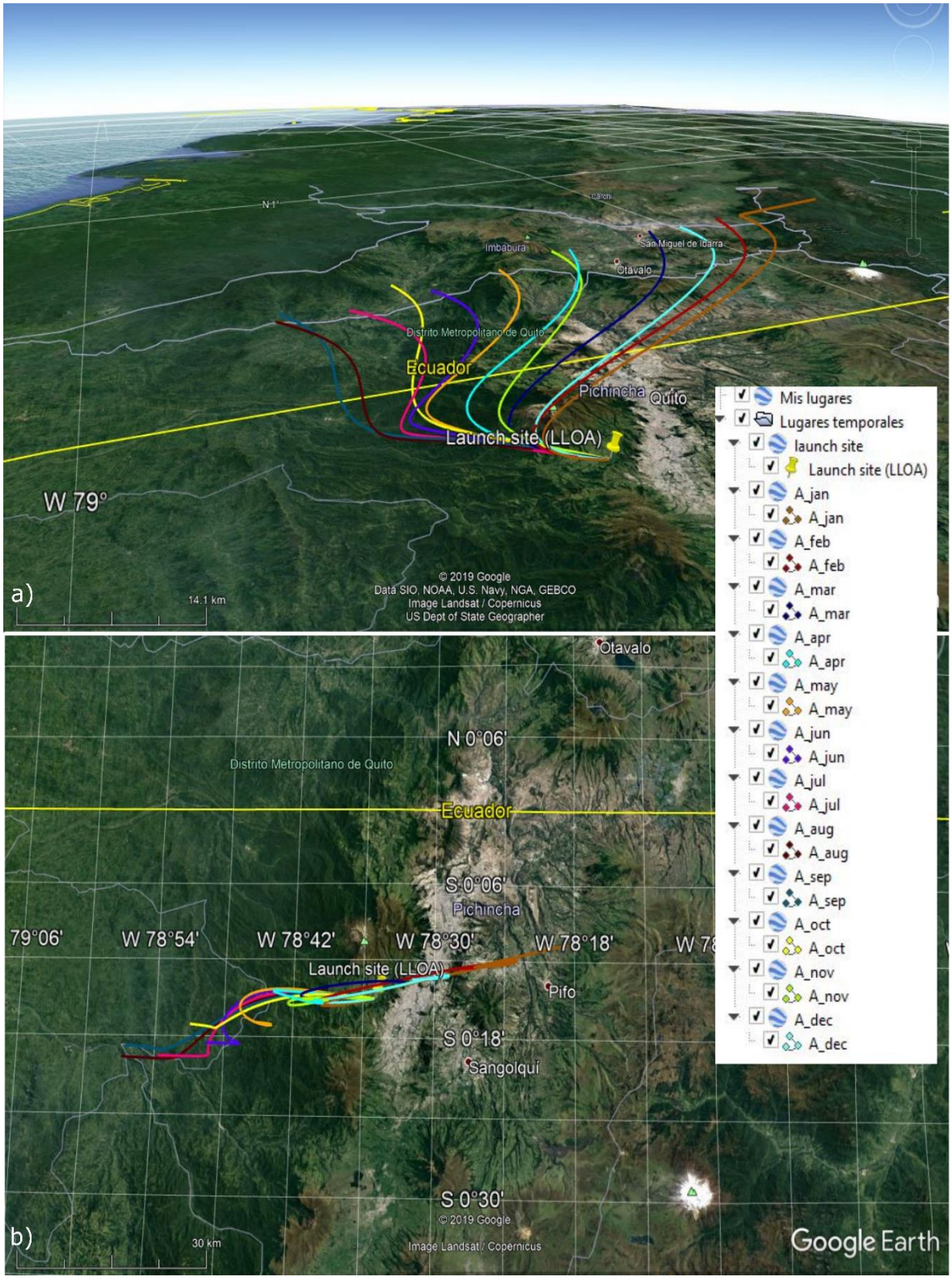

Figure 3.3. Trajectory simulations for balloon A during the year, a) side view, b) top view
(Source: own)

Finally, the other parameter that needs to be analyzed is the power requirements to run the environmental monitoring mission. For this the flight duration plays an important role to calculate if the battery will be sufficient to power the entire flight considering the data collection strategies introduced in section 2.5. Figure 3.4 shows the number of images that can be achieved with each balloon design case for each collection strategy. In general, balloon B can collect the most images and other environmental data. However, as shown in Figure 3.5, it will run out of power before its flight is over. Balloon A runs into a similar fate with the MAX collection strategy; while, balloon C will have power left after burst for at least 40 more minutes, important for increasing the chances of recovery. These results suggest thus far that the best option for the balloon as platform for environmental monitoring is C.

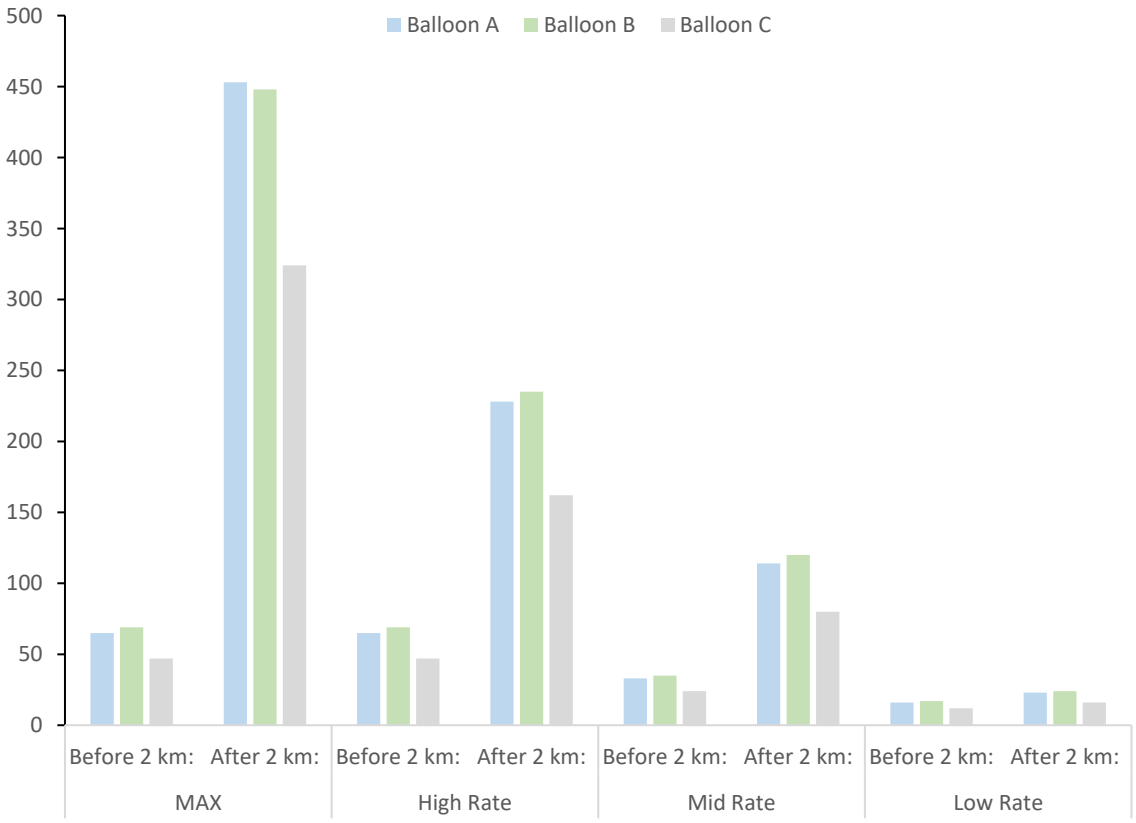

Figure 3.4. Number of samples collected by the balloon per collection strategy
(Source: own)

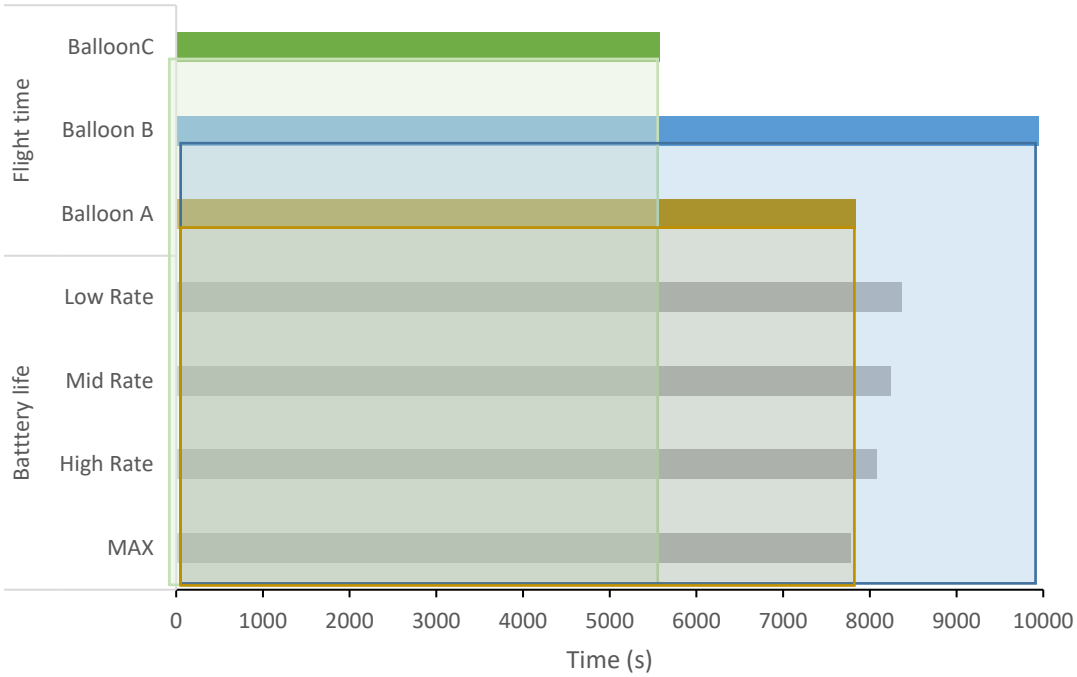

Figure 3.5. Flight duration and battery life for each balloon case and collection strategy
(Source: own)

3.2. Nanosatellite

Figure 3.7 and Figure 3.6 show the first 120 minutes of orbit life. Notice that Orbit C passes over the ground station directly as it has an inclination of near 0 degrees.

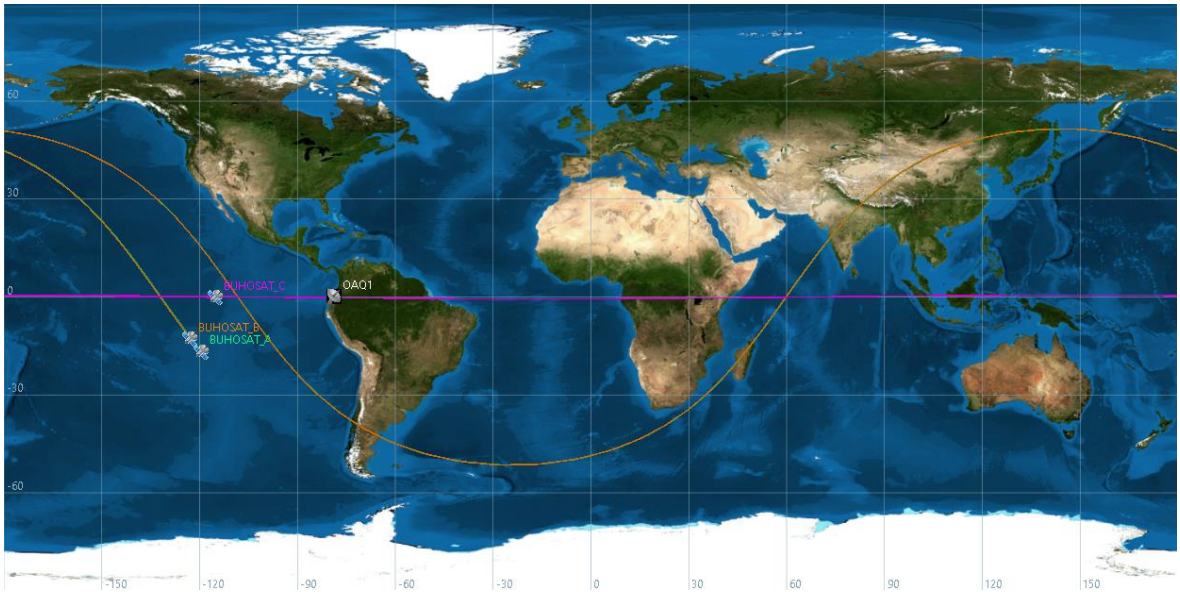

Figure 3.6. Ground track view of the three nanosatellite cases
(Source: own)

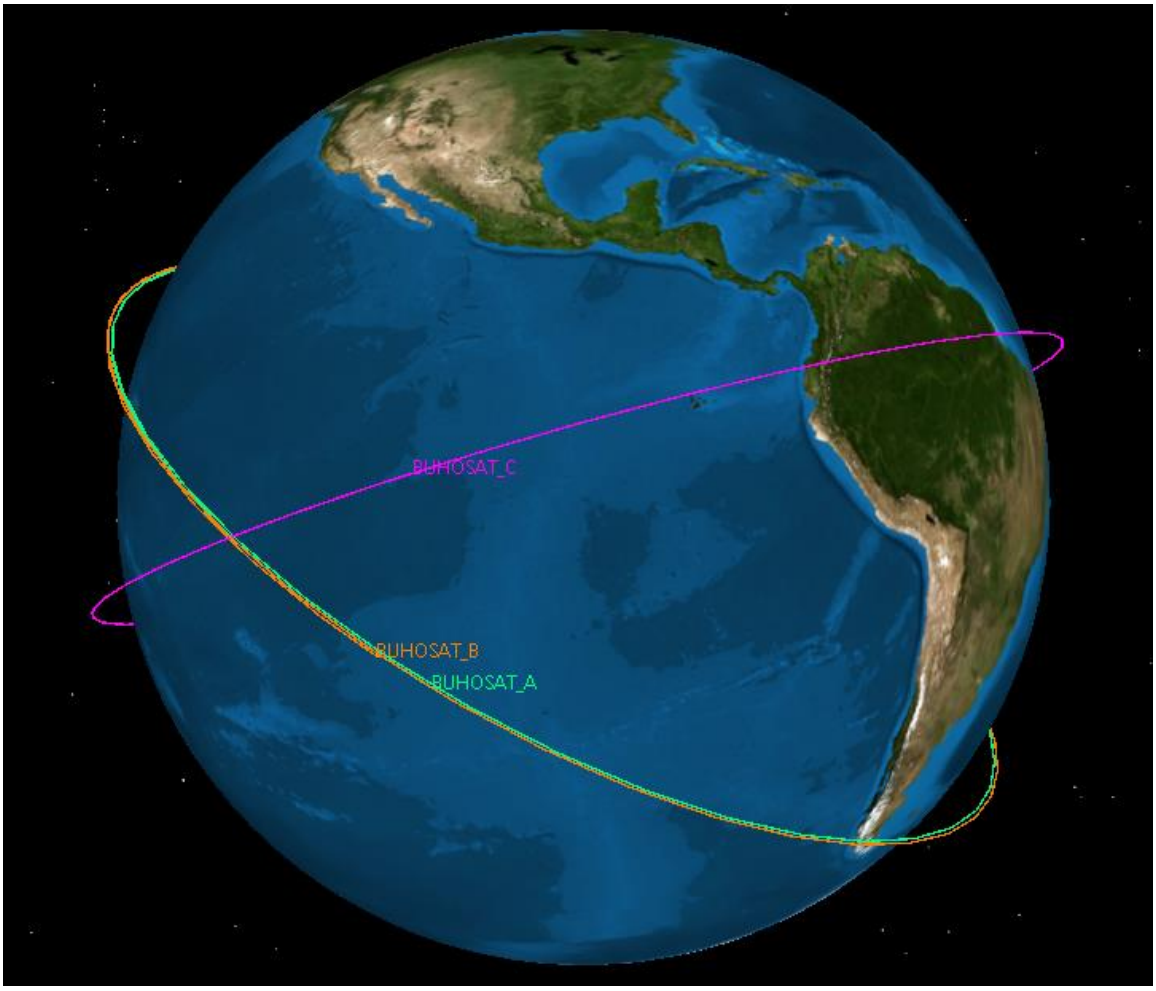

Figure 3.7. 3D orbit view of the three nanosatellite cases
(Source: own)

As explained in the methodology section orbit B was extrapolated from orbit A by simulating orbits by adding 50 km intervals to the semi-mayor axis and leaving the other orbital elements the same until finding an orbit that can last for at least one year. Figure 3.8 shows the result of these simulations, notice that as the orbit reach an altitude of near 250 km from earth's surface it decays quickly. The orbit scenario that was picket for Orbit B is Orbit A + 50 km. Orbit C has the same initial orbital elements as B except for the inclination to near 0, Table 2.3. Orbital elements for the three nanosatellite casesTable 2.3, and a life span similar to Orbit B. On the other hand, Orbit A, which is a deployment from the ISS has a much shorter life span, approximately 160 days. Although, Orbit A does not allow a full year of operation for the CubeSat, it should also be included in this analysis since it presents other benefits such as cost, discussed in more detail latter in this work.

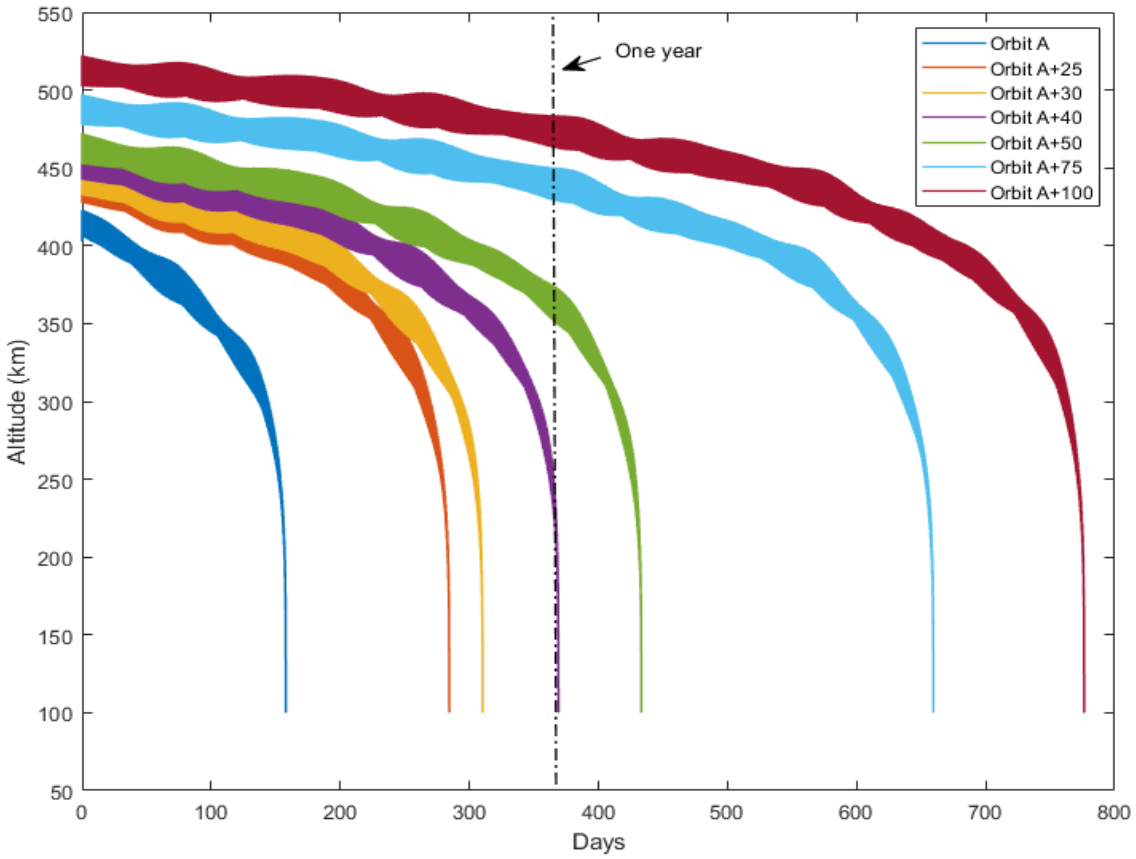

Figure 3.8. Orbit simulations used to find the best altitude for Orbit B
(Source: own)

The most important results from these orbit simulations are displayed in Table 3.2. All orbits last until they reach 100 km altitude. that corresponds to the time in orbit until 100 km altitude. The data in the table corresponds to 157 days in the case of orbit A and 365 days for B and C even though these orbits decay in longer times. The average contact widow for orbit B increases by about 100 seconds and the number of contacts more than double compared to orbit A because the higher altitude helps increase the viewing angle for communication. Furthermore, the contact window for orbit C and the number of contacts has a significant improvement over the other two because the inclination allows the CubeSat to be in a direct line of sight with the ground station, Figure 3.6. The table also states the number of possible contacts that have enough window duration to allow download of telemetry, and images in JPEG and BMP formats. This was determined using the download times mentioned I section 2.3. This information is important to analyze power requirements and the overall CubeSat performance for environmental monitoring with the RGB camera. Notice that the near equatorial orbit has many opportunities, but will require more power.

Table 3.2. Main results from orbit simulations

	Orbits (#)	Average period (s)	Contacts (#)	Contact window (average) (s)	Contacts (telemetry) (#)	Contacts JPEG (#)	Contacts BMP (#)
Orbit A	2437	5459.5	373	274.95	372	343	121
Orbit B	5340	5661.2	985	367.42	985	951	720
Orbit C	5602	5644.8	5237	444.99	5237	5237	5237

(Source: own)

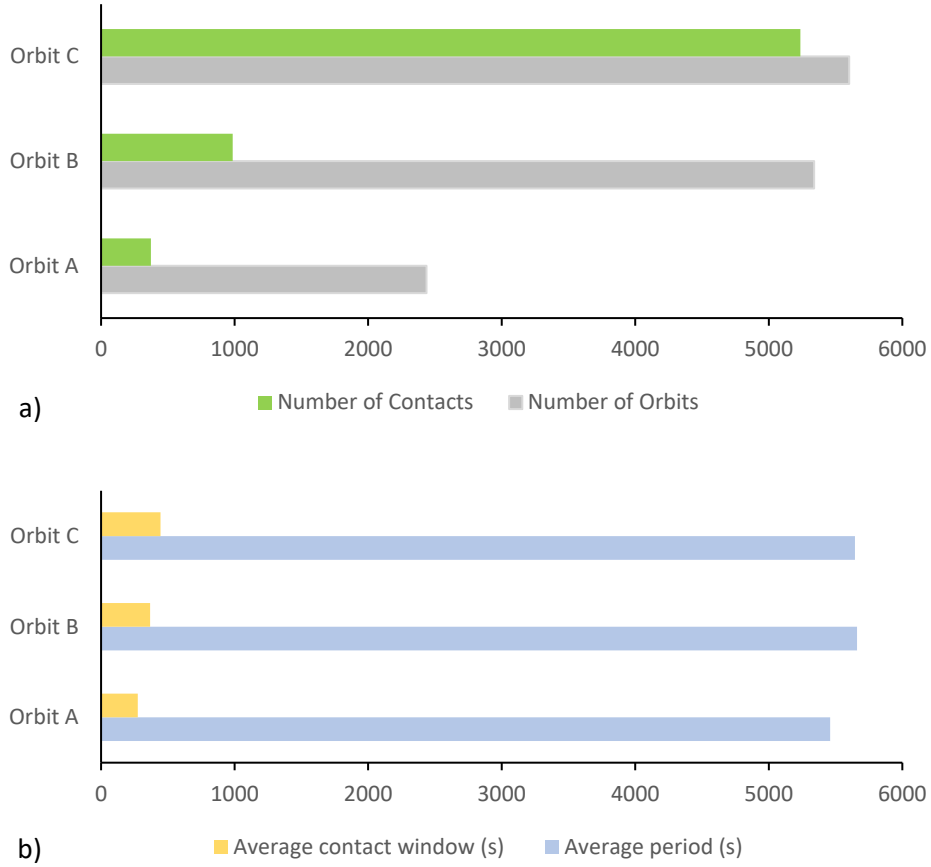

Figure 3.9. Nanosatellite contact opportunities a) Number of contacts b) average contact window (Source: own)

Power requirement plays an important role in the analysis to determine the best type of orbit. To calculate the power available and required the orbit simulations were used together with the information previously presented. Annex C shows an example of the power and current calculations for Orbit A, the other two orbits followed the same procedure, and the results are shown in Figure 3.10, Figure 3.11, and Figure 3.12. The figures show the power available from the solar panels and the power required by five typical orbits: first orbit, non-

collection (non-contact), non-collection (contact), JPEG collection, and BMP collection. The first orbit requires additional power to run mechanisms to start the CubeSat such as electric knifes to deploy the antenna. Non-collection (non-contact) orbits are the most common ones, being the ones without any contact with the ground station. Non-collection (contact) are the orbits that have contact with the ground station; however, the contact window is not large enough to allow image transmission. JPEG and BMP collection orbits are the ones that have a large contact window to allow transmission of those types of image formats, notice that there are fewer opportunities for BMP images. In addition, notice that Orbit C present the most image collection opportunities, in fact there is only a small percentage of periods too small to collect an image (7.2%). The mentioned figures, also show the power consumption from the solar panels and the battery based on the component power rating, and sunlight exposure Annex C. Furthermore, the figures also highlight the battery current used and the solar panels power available to recharge the batteries and the amount of current that may be charged per orbit based on the GMAT simulation and the methodology previously presented, Figure 3.13Figure 3.14Figure 3.15.

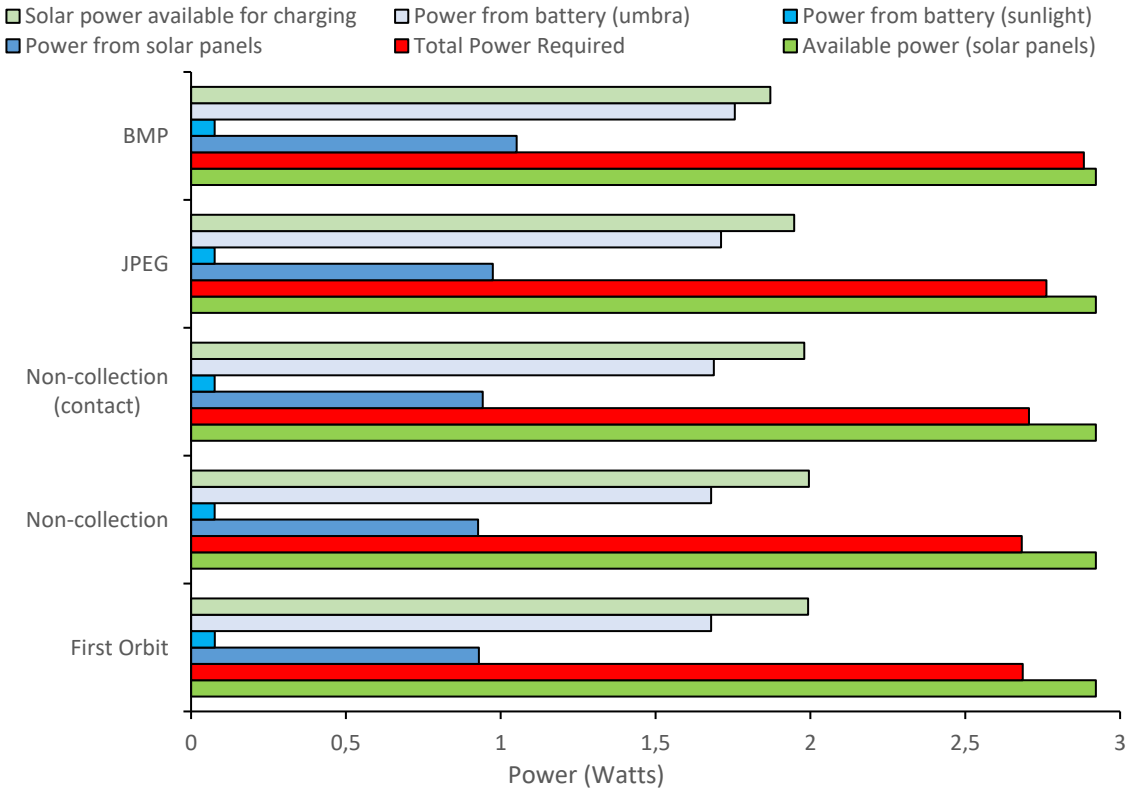

Figure 3.10. Power required and available for the nanosatellite, Orbit A
(Source: own)

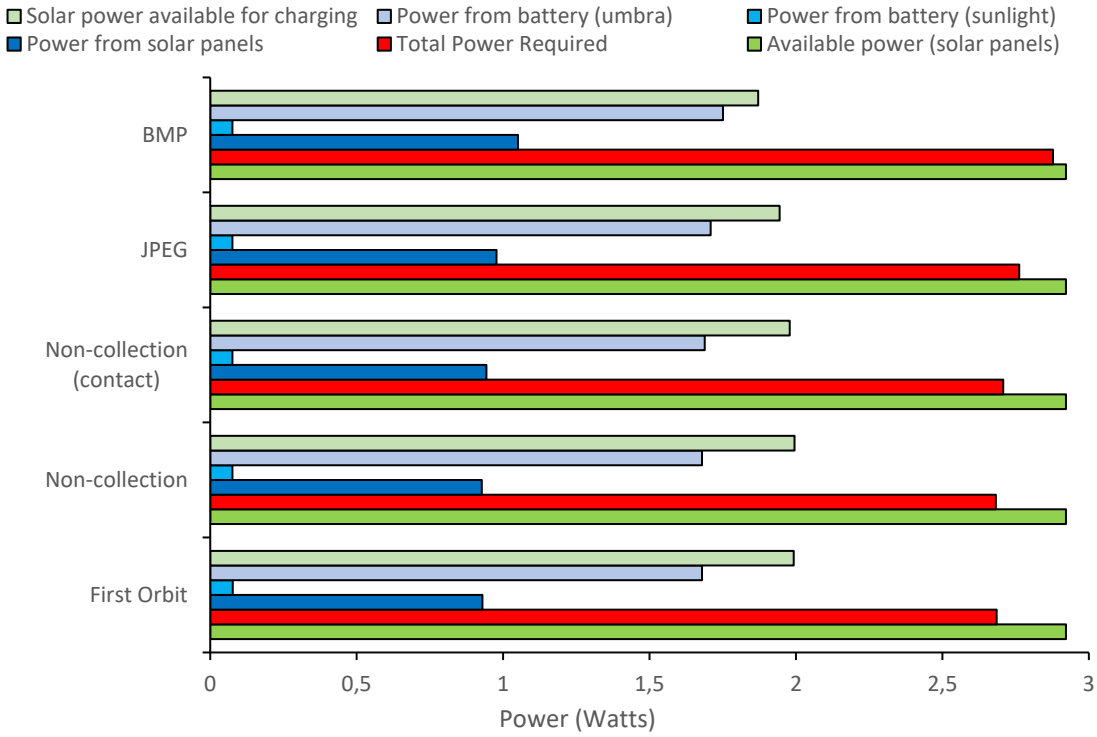

Figure 3.11. Power required and available for the nanosatellite, Orbit B
(Source: own)

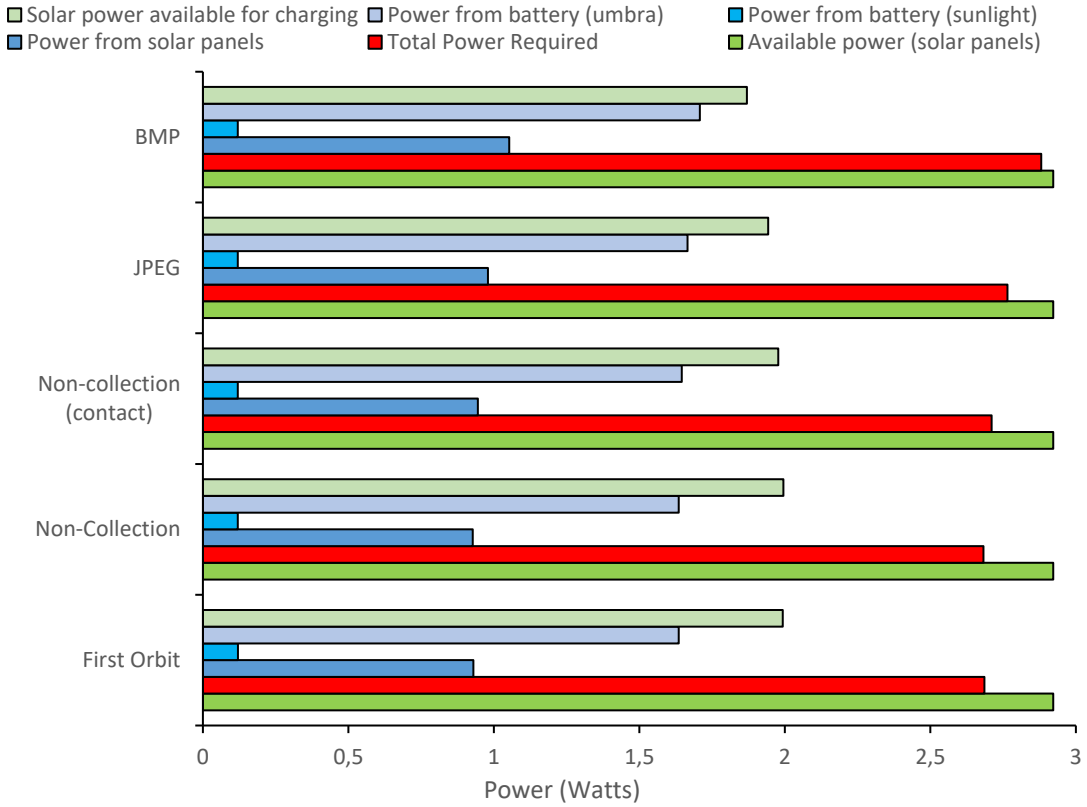

Figure 3.12. Power required and available for the nanosatellite, Orbit C
(Source: own)

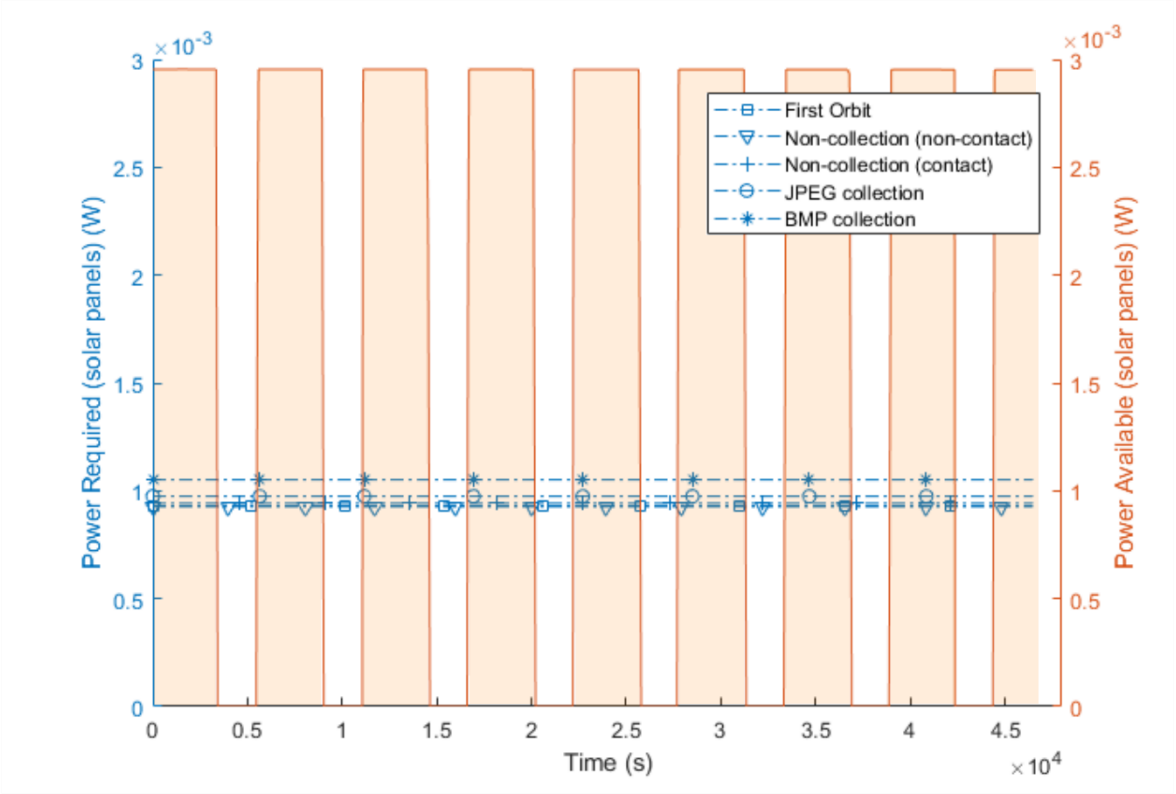

Figure 3.13. Solar power available and required per period, Orbit A
(Source: own)

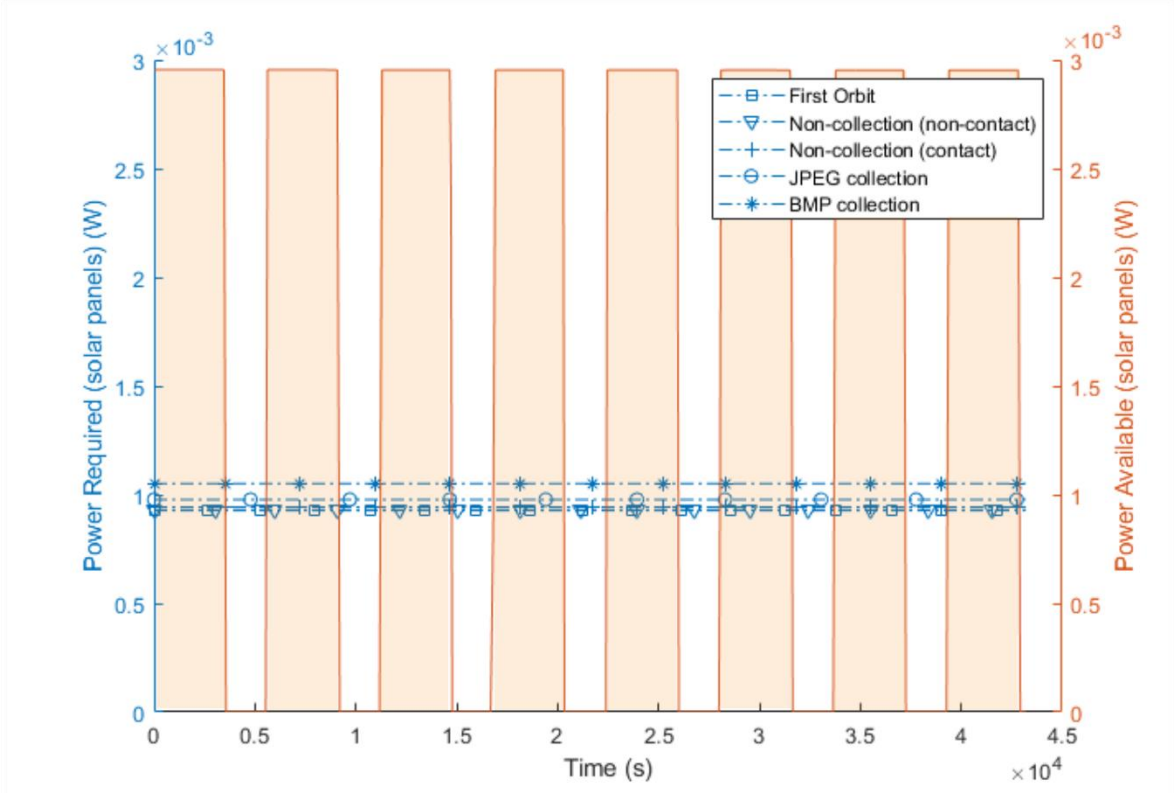

Figure 3.14. Solar power available and required per period, Orbit B
(Source: own)

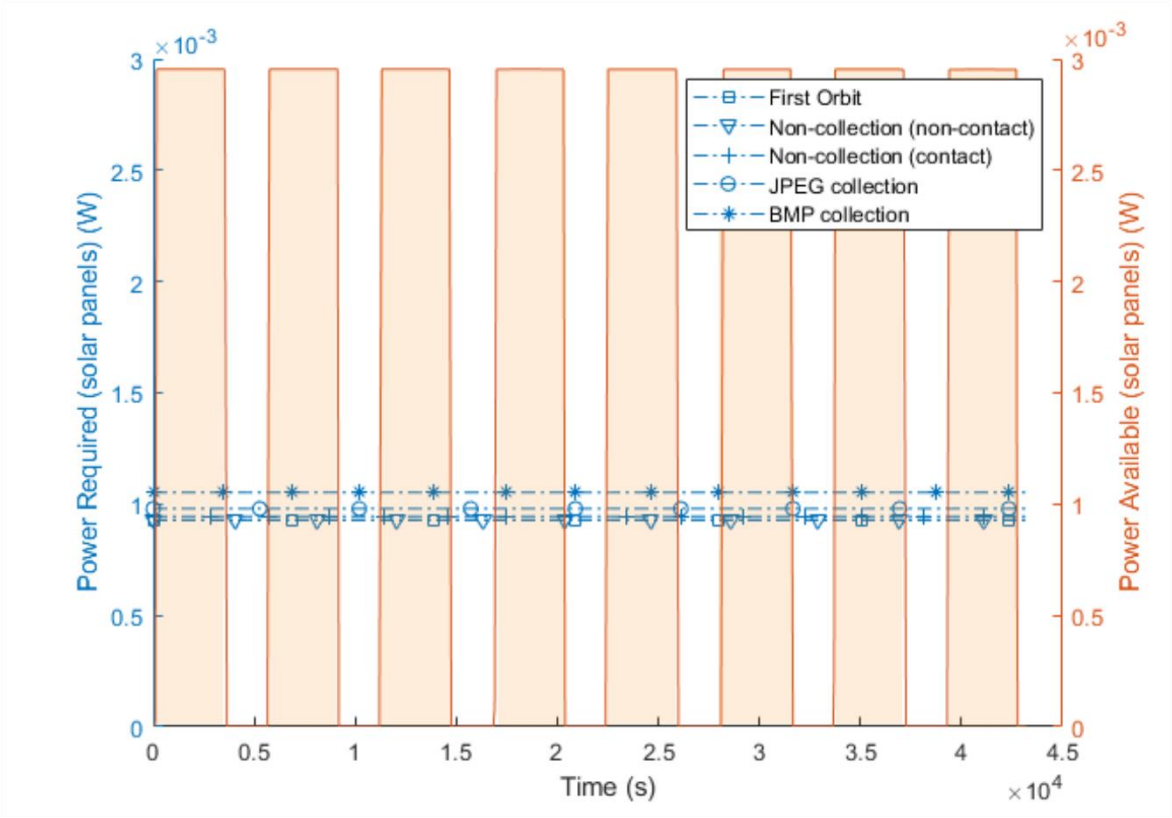

Figure 3.15. Solar power available and required per period, Orbit C
(Source: own)

These results suggest that the CubeSat's electrical power system is capable of handling all power needs to run the mission successfully for all three orbits and that the batteries can be fully charged each period. Therefore, power requirements are not a determining factor for selecting the orbit. On the other hand, collection opportunities are significantly improved with orbit C (inclination near the equator). It is analyzed latter on if this is the best cost-effective orbit.

3.3. Fixed wing UAV

The models were used to determine three preliminary designs for UAVs, each corresponding manly to the required operational altitude. These UAV designs are referred as UAV class in this work. UAV A corresponds to an operational altitude near see level, UAV B corresponds to an operational altitude near Quito, and UAV C corresponds to an operational altitude near 4000 m above sea level. The first step was to create the design space using the constraints model. Figure 3.16, shows the solution generated by the model, notice that the design points for each UAV is set around the middle of the design space and

ROC for all three resulted in 2.7 m/s. Furthermore, it is interesting to see that the design space for the higher altitude UAV shrinks compared to the sea level UAV. This is because at higher altitudes it is harder to maintain flight and the low-density hinder performance. Hence, the importance of preliminary design for specific operational altitudes.

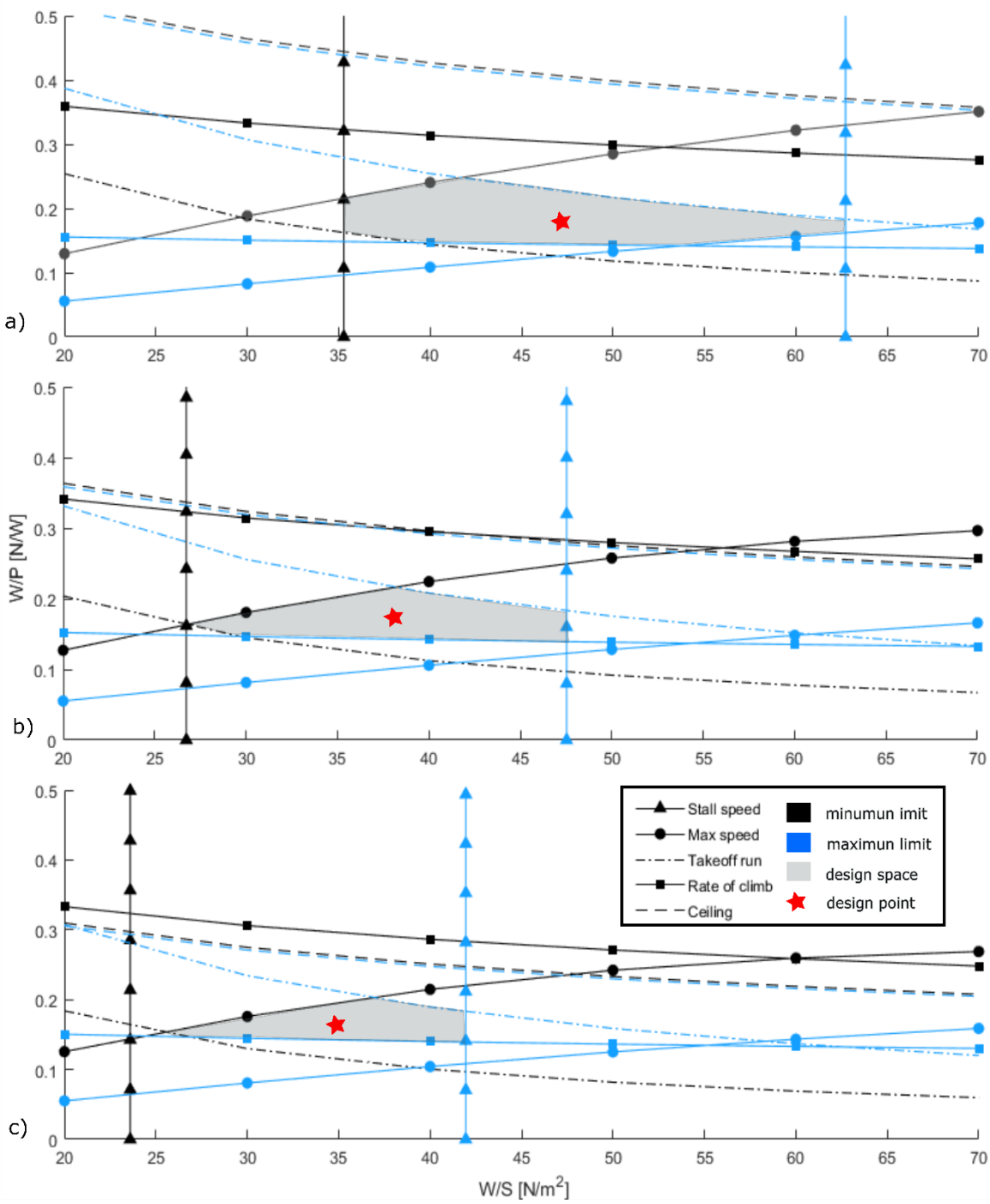

Figure 3.16. Constraint analysis, a) UAV A, b) UAV B, c) UAV C
(Source: own, Reference [55])

The constraint analysis set the foundation for the geometry and the aerodynamic models discussed in section 2.4. The results for the UAV sizing and airfoil selection were previously presented in section 1.4, Table 1.11 and Table 1.12 to keep a logical order in the presentation of this thesis. Notice that for UAV class B and class C the geometry of the lifting surfaces is larger than the UAV class A, Table 1.11. This is because at lower density the UAV will require bigger lifting surfaces for flight. However, the extra size and weight of the lifting surfaces and fuselage needed for UAV B and C will have a negative effect on the available weight for the battery. This is because the model optimizes a preliminary UAV weight based on payload mass and not necessarily operational altitude; which, resulted in a preliminary mass of 2.039 kg for all three UAVs. Nevertheless, as shown with the results here presented this does not have much effect on the overall performance. On the other hand, the aerodynamics model was also used to obtain important flight speeds that optimized the aerodynamic performance of the UAV. These speeds that are needed to help select the most adequate propulsion system components are presented in Table 3.3 and serve as input for the propulsion selection model.

The next step was to select the propulsion system components as previously discussed. Again, to maintain a logical flow and structure for the thesis the components that were selected by the model were presented in Table 1.13 in section 1.4, because that section presents the main parameters that are used for the main analysis, namely the performance of each platform for weather monitoring using an RGB camera. The selected electric motor is from T-motor [67], and is the same base model for all three UAV classes with a variation in the Kv rating, with the higher altitude UAVs having a faster Kv since more revolutions are required to generate thrust in thinner air (low air density). A proper propeller must be selected to have the best possible efficiency for the propulsion system. To find a matching propeller that maximizes efficiency there must be a similar torque rating by the motor and the propeller at specific revolutions and flight speed. Figure 3.17Figure 3.18Figure 3.19 plot the electric motor performance at different throttle settings and also show the performance of the selected propeller for different flight speeds. The propeller data used to create the figures come from actual propeller tests done at sea level; while, the data used to plot the electric motor performance come from theory as previously discussed given by reference [53]. Using the provided data, the optimal RPM setting that the model selected for all three UAV classes resulted in 7000 RPM for cruise. Furthermore, it is important to mention that the propeller data presented by Figure 3.18 and Figure 3.19 was corrected to the proper altitude. The resulting propeller selection is also presented in Table 1.13 from section 1.4.

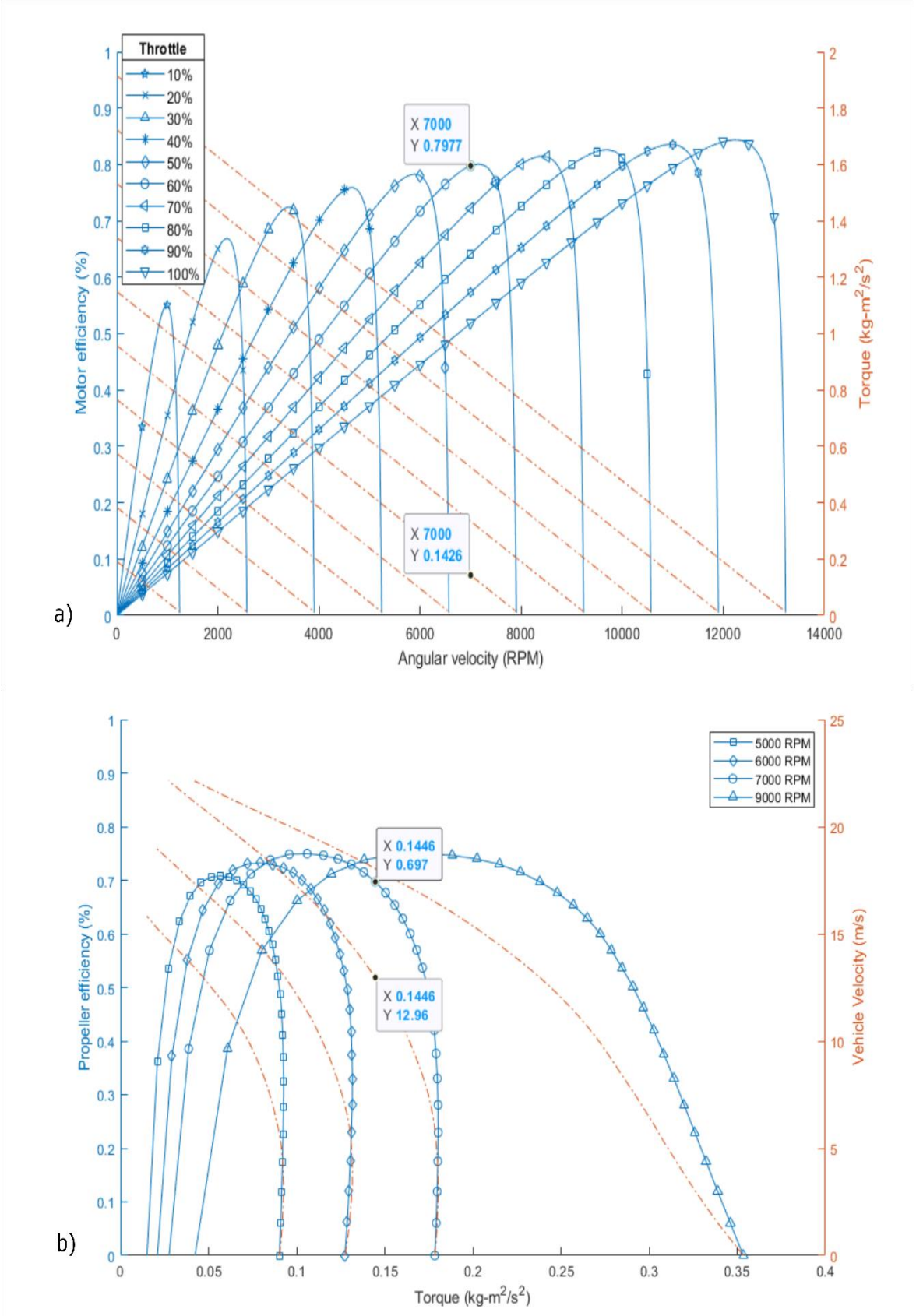

Figure 3.17. Propulsion system performance, UAV A a) Electric motor, b) Propeller
(Source: own)

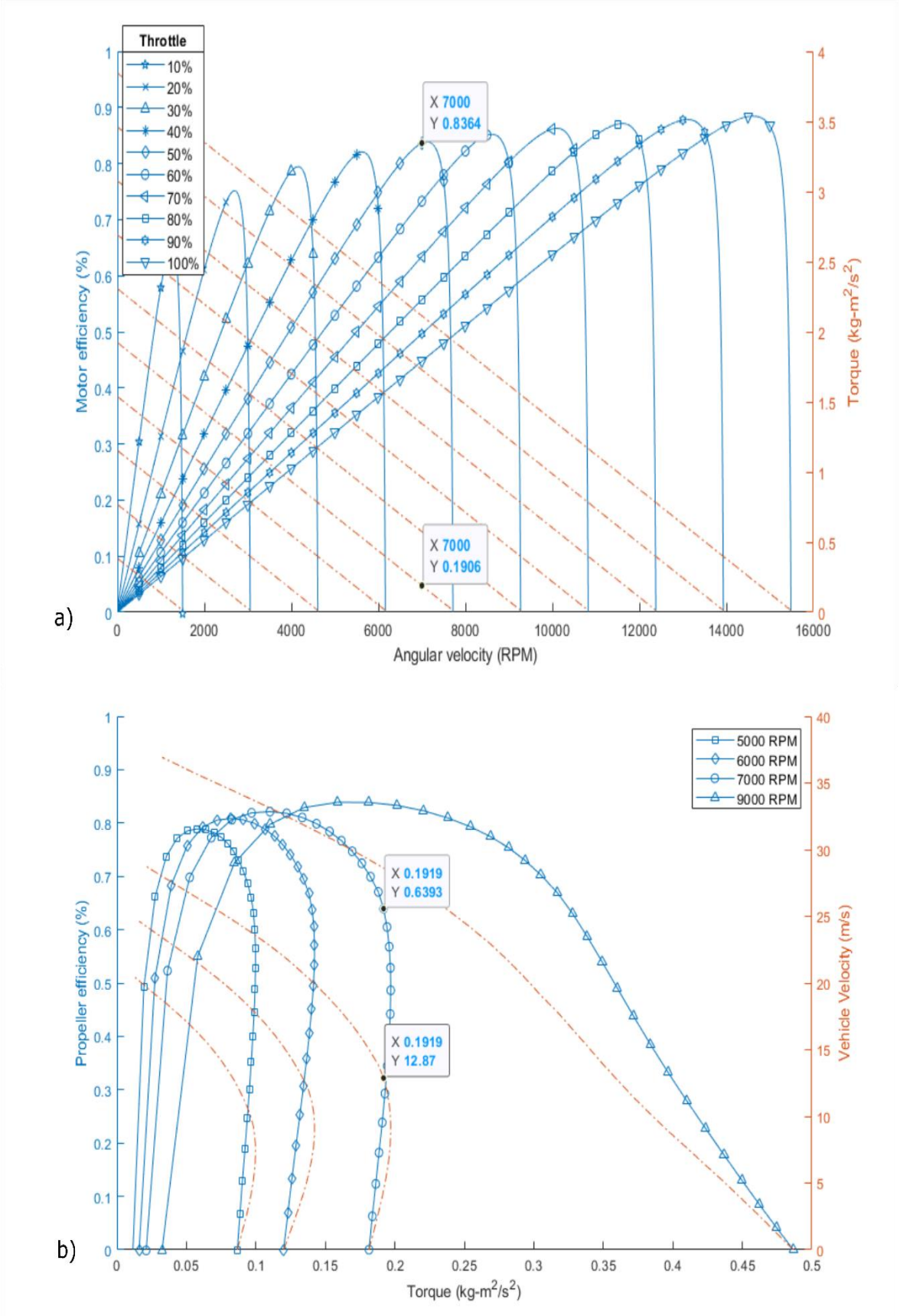

Figure 3.18. Propulsion system performance, UAV B a) Electric motor, b) Propeller
(Source: own)

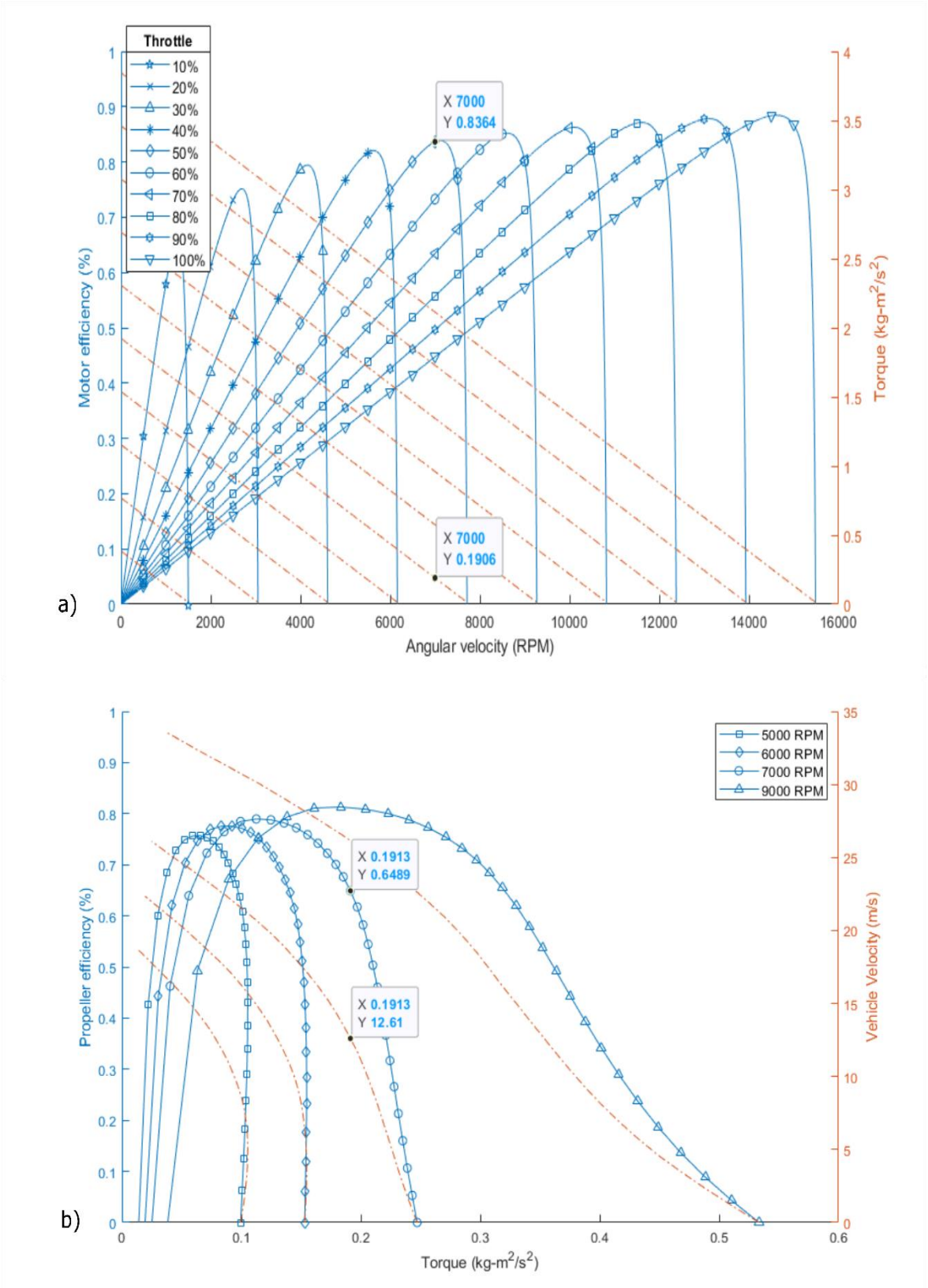

Figure 3.19. Propulsion system performance, UAV C a) Electric motor, b) Propeller
(Source: own)

The following table summarizes the main performance results and parameters needed for further analysis obtained from the models thus far mentioned. Notice that the propulsion system efficiency depends on the RPM setting that in turn depends on the cruise speed that is desired, previously obtained using the aerodynamics model. Additionally, the power required for specific flight speeds was obtained from the aerodynamics model and are shown in Figure 3.20. The figure also shows the available power from the selected propulsion system. Notice that for the case of UAV A and B the propulsion system at 7000 RPMs does not cover the full requirement range (i.e. past 18 m/s). Nevertheless, this is of no importance since the speed limit was previously set at 16 m/s. Furthermore, as previously mentioned the figure displays the performance according to the best possible efficiency for the specific needed parameters (i.e. the corresponding cruise speeds for each UAV).

Table 3.3. Fixed wing UAV models main results

	UAV A	**UAV B**	**UAV C**
RPM	7000	7000	7000
V_{Dmin} (m/s)	8.5203	10.2385	10.3739
V_{stall} (m/s)	7.4554	7.4716	7.5375
V_c (m/s)	12.9587	12.0962	12.0952
η_p	0.798	0.836	0.836
η_m	0.697	0.639	0.649
η_t	0.556	0.534	0.543
P_{Req_c} (W)	27.6563	19.1536	19.31
ROC (m/s)	2.7	2.7	2.7
D_c (N)	2.2708	1.5834	1.5966

(Source: own)

Using the information provided in Table 3.3 the range and endurance can be determined for each UAV class and RGB camera collection strategy as previously discussed. Furthermore, the range and endurance differ if the UAV climbs up to 100 m or 200 m. The results are presented in the following figures.

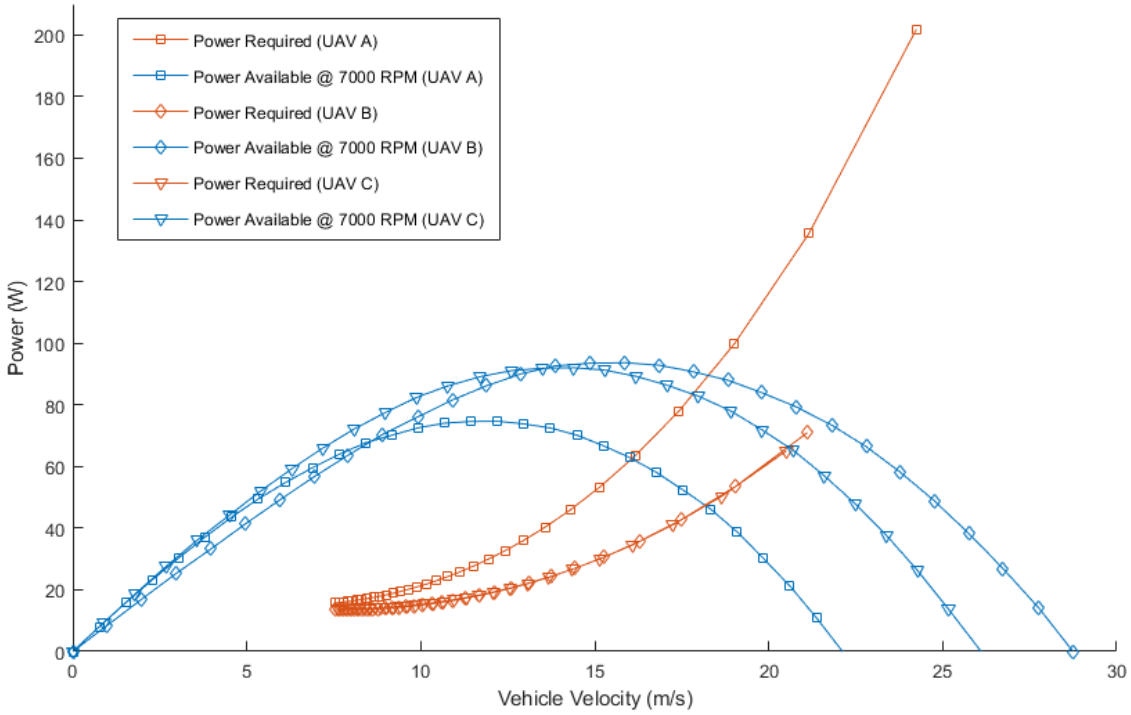

Figure 3.20. Propulsion power requirement, Fixed wing UAVs
(Source: own)

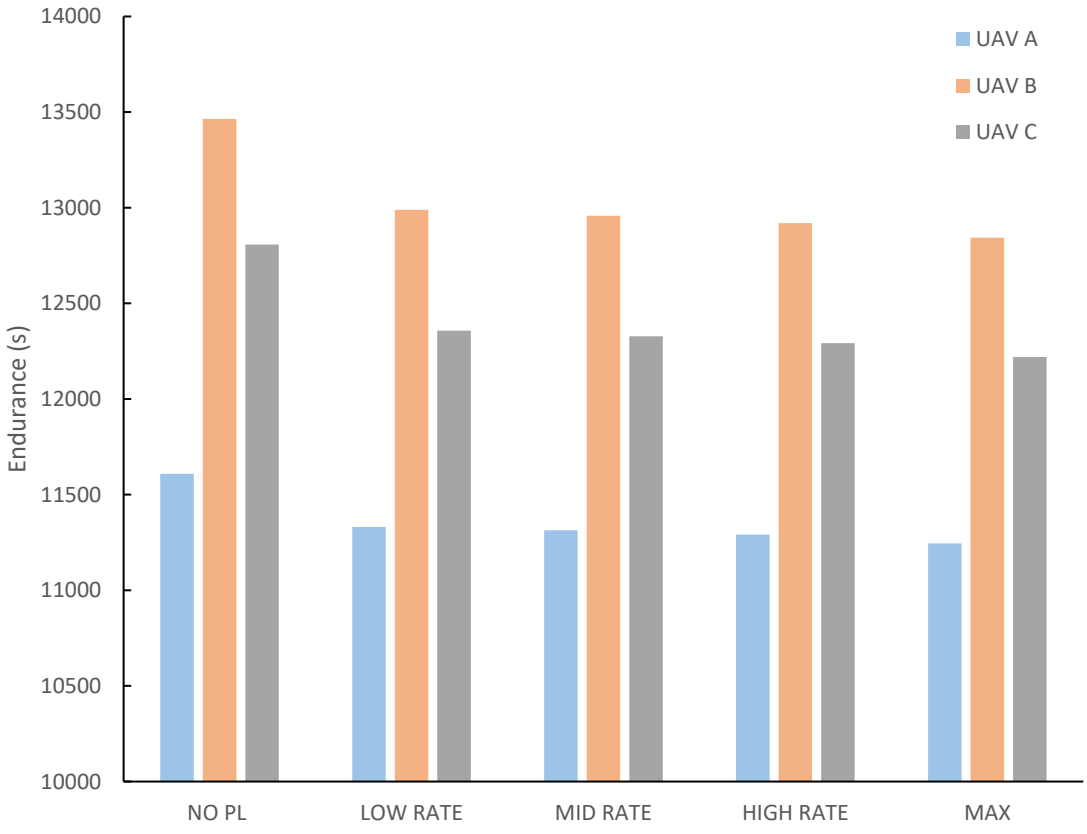

Figure 3.21. Endurance, fixed wing UAVs
(Source: own)

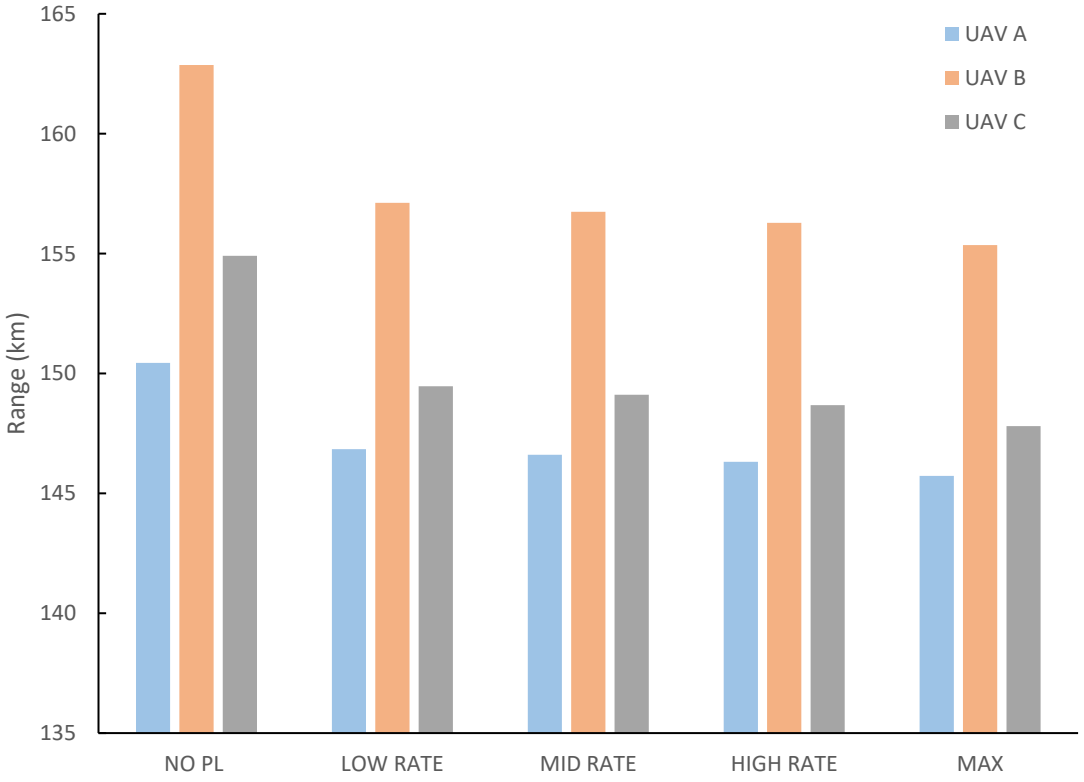

Figure 3.22. Range, fixed wing UAVs
(Source: own)

Notice that the endurance decreases as the collection rate of data increases. The NO PL case is the endurance of the UAV when no data is collected. The UAV class B resulted with the highest endurance, approx. 30 minutes more than UAV class A and 11 minutes more than UAV class B for NO PL, even though UAV A has the largest battery, Table 1.13. This could be to the fact that the models provided a better overall preliminary design (geometry and propulsion system selection) for the class B UAV. On the other hand, Figure 3.23 brakes down the endurance to three main sections: take-off, cruise, and landing for each UAV class. There is a reduction of about 1.5% in cruise time when the UAV climbs to 200 m above ground altitude as opposed to 100 m. Data collection differences for each altitude above ground level will be discussed latter on.

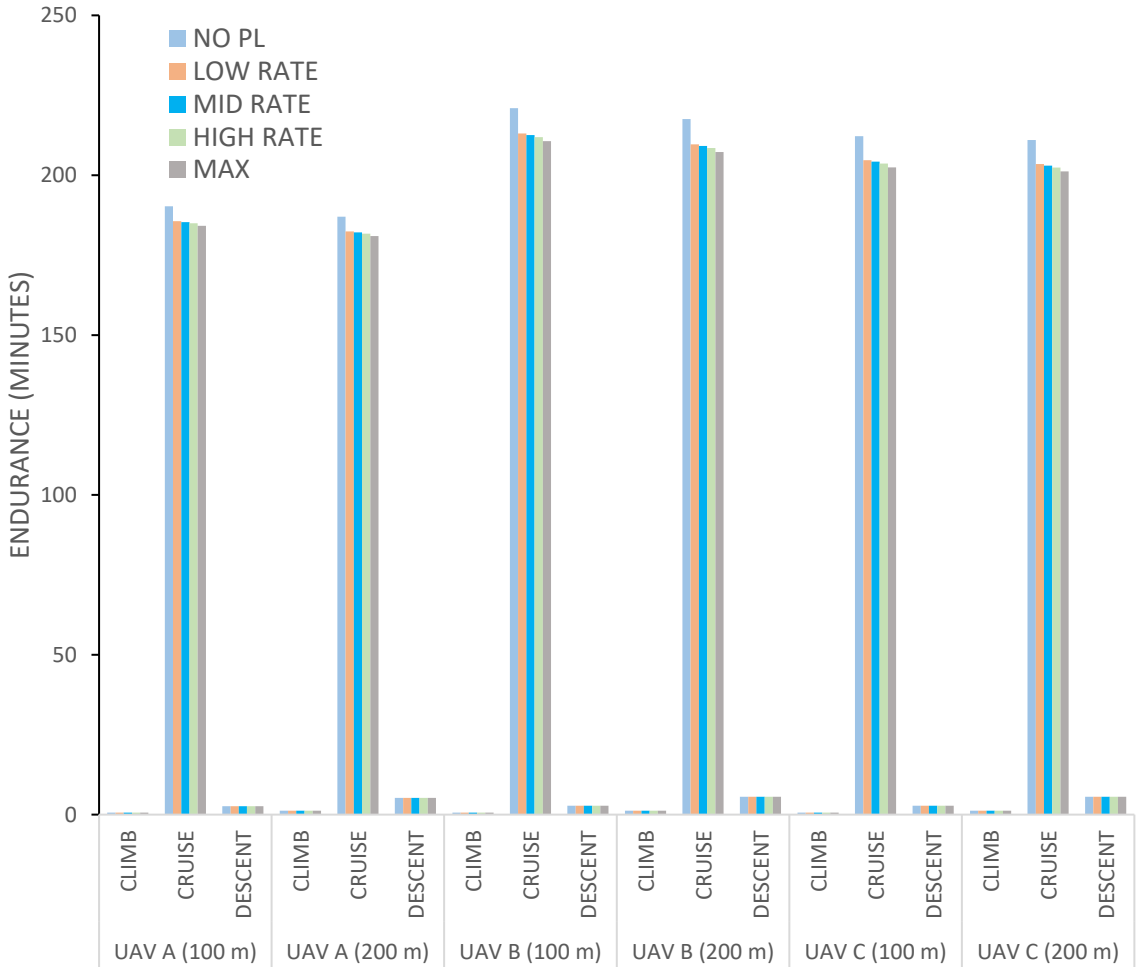

Figure 3.23. Endurance with image acquisition, fixed wing UAVs
(Source: own)

On the other hand, range, Figure 3.22 is an important parameter to know if the mission requires the UAV to travel far. However, many data collection missions for weather monitoring require data for a specific area. In these cases, range can provide a good idea about the size of the area that can be covered during one particular flight. There are many data collection strategies and flight patterns that can be used to optimize data collection that will not be covered in detail in this thesis; however, latter on can be seen how the FOV of the camera together with the UAV rage can be helpful to determine how much area can be covered.

The UAV design approach presented in this work allows for UAVs tailored to be more efficient at different altitudes. This suggest that the UAV solution should not be a particular design, rather it should be a few designs that cover specific needs. This is why as mentioned in section 2.6 the three UAV classes are used intrinsically together in the UAV program for the environmental monitoring mission in analysis.

3.4. Life cycle costs

The following table shows the main cost results for the parameters introduced in section 1.5 and the total life cycle cost for the different study cases of the three aerospace platforms for a one-year program as discussed in section 2.5. As mentioned earlier the fixed wing UAVs are looked as a whole when considering the one-year program scenarios because they were designed for specific site management meaning that each of the UAV classes perform better at different altitudes. Therefore, the one-year fixed wing UAV program consisted of 2 UAVs of each class operating 122 days each to equal the operation of the other two aerospace platforms (every day of the year). For the two other platforms the one-year program is considered for each specific design case to find the best alternative for those two platforms. Nevertheless, previous review of result suggest that design case B of the balloon can be discarded because of power requirements, and Orbit A of the nanosatellite can be discarded because it cannot complete the one-year program stated as a requirement in this study. The main benefit of Orbit A is to have the opportunity of a free launch and orbit deployment from ISS reducing the LCC of the CubeSat significantly, nearly 19%.

Table 3.4. Life cycle cost results for one-year program, all platforms

LCC Parameters		Balloon			Nanosatellite			UAVs
		A	B	C	Orbit A	Orbit B	Orbit C	
RDTE	MHR_{ed_r} (hrs)	173,50	173,50	173,50	347,44	347,44	347,44	413,86
	MHR_{man_r} (hrs)	63,19	63,19	63,19	430,05	430,05	430,05	73,38
	MHR_{tool_r} (hrs)	55,81	55,81	55,81	11,79	11,79	11,79	11,32
	C_{ed_r} (USD)	1020,18	1020,18	1020,18	2042,94	2042,94	2042,94	2433,5
	C_{dst_r} (USD)	624,84	624,84	624,84	892,04	892,04	892,04	1496,43
	C_{tp_r} (USD)	4169,48	4296,34	4169,48	90033,42	85253,92	85253,92	2857,82
	C_{to_r} (USD)	3572,51	3572,51	3572,51	1211,93	1211,93	1211,93	4146,96
	C_{tsf_r} (USD)	94,82	96,10	94,82	23545,08	22350,21	22350,21	1214,97
	C_{pro_r} (USD)	0,00	0,00	0,00	0,00	0,00	0	0,00
	C_{fin_r} (USD)	0,00	0,00	0,00	0,00	0,00	0	0,00
	RDTE (USD)	9481,83	9609,97	9481,83	117725,41	111751,03	111751,03	12149,68

ACQ	MHR_{ed_p} (hrs)	396,50	396,50	396,50	394,43	394,43	394,43	574,45
	MHR_{man_p} (hrs)	673,67	673,67	673,67	618,39	618,39	618,39	187,64
	MHR_{tool_p} (hrs)	124,70	124,70	124,70	13,34	13,34	13,34	15,58
	C_{ed_a} (USD)	1311,22	1311,22	1311,22	276,29	276,29	276,29	944,29
	C_{man_p} (USD)	3589,61	3589,61	3589,61	1107,42	1107,42	1107,42	671,84
	C_{tool_a} (USD)	405,06	405,06	405,06	9,11	9,11	9,11	25,01
	C_{qc_a} (USD)	466,65	466,65	466,65	143,96	143,96	143,96	87,34
	C_{pp_a} (USD)	317521,26	329128,95	317521,26	88367,12	83863,91	83863,909	12384,89
	C_{fin_a} (USD)	0,00	0,00	0,00	0,00	0,00	0	0,00
	C_{man_a} (USD)	318832,48	330440,17	318832,48	88643,41	83863,91	83863,91	12384,89
	C_{pro_a} (USD)	0,00	0,00	0,00	0,00	0,00	0	0,00
	ACQ (USD)	318832,48	330440,17	318832,48	88643,41	83863,91	83863,91	13329,18
OPS	P_{unit}	1813,89	1814,60	1813,89	206368,82	195614,94	195614,94	5095,77
	DOC_{dpr}	1813,89	1814,60	1813,89	162815,49	154451,37	154451,37	3358,71
	OPS	99752,75	110475,24	101914,36	174797,89	262341,97	273891,74	36232,59
DISP	DISP	4323,91	4550,76	4345,74	3850,17	4625,83	4742,49	623,35
LCC		432390,97	455076,14	434574,41	385016,87	462582,74	474249,17	62334,80

(Source: own)

Figure 3.24, summarizes the four main costs that add up to the LCC, notice that the fixed wing UAV is the more economical solution. First, it is important to understand that the number of vehicles produced for each platform plays an important role in the final LCC. In the case of the balloon, the balloon needs to be replaced constantly since it is not easy to recover without a trajectory control feature such as the one discussed in reference [53]. This increases acquisition costs by a lot as shown by the results even though the balloon is much cheaper per unit (1813.89 USD) in the LCC context, as compared to the nanosatellite ($195614.94) and the fixed wing UAV ($5095.77). In fact, flying balloons to collect every

day runs the highest acquisition cost of the three platforms, even higher than the nanosatellite, which uses expensive components. In fact, even though the nanosatellite uses the same camera it costs around 17 times more because of the space rating and certificates. On the other hand, the CubeSat runs the highest RDTE cost; which, is not surprising since a satellite requires more effort in design, modeling, simulation, and better assembly and manufacturing precision. Furthermore, it requires specialized laboratories such as a clean room, in particular when working with optics. And, it also requires flight readiness certificates that need to be certified in specialized laboratories, notice the high test and simulation (tsf) cost that is in accordance to real life examples. In addition, the Cubesat runs the highest operational cost, this because of the launch and deployment to orbit, which costs around 100 thousand dollars. The surprise in operational cost is the balloon, running a higher than expected cost; however, this can be explained because of the need of helium as lifting gas that has a cost of about $67 per m^3. Further detail on operational costs can be found in annex F.

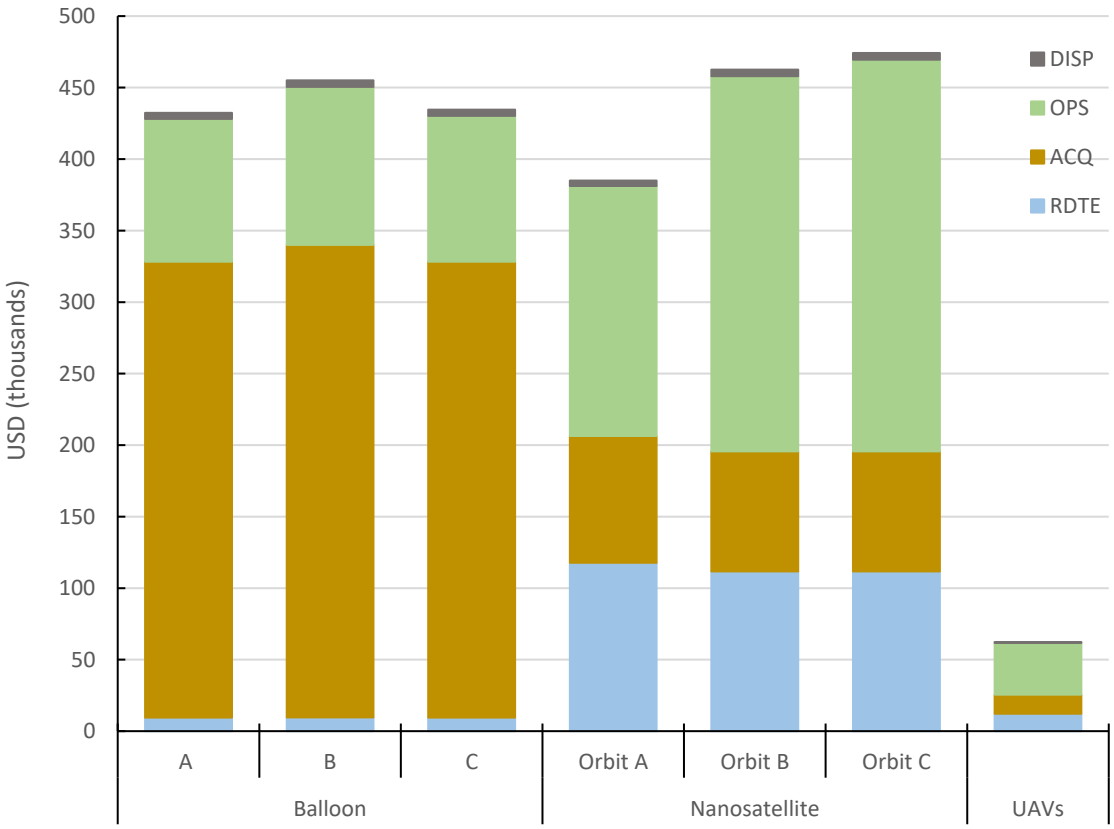

Figure 3.24. Life cycle cost breakdown, all platforms
(Source: own)

The fixed wing UAV is clearly the best choice over the other two platforms when cost is the main driver. This comes as no big surprise since RDTE costs are much cheaper than the CubeSat and only about 20 % more than the balloon, mainly due to complexity, and the need for only six UAV as opposed to the high number of balloons makes the acquisition cost very cheap in comparison, even though the unit price is 3 times more. Additionally, the operational cost is much less because there is no need to buy any consumable such as gasoline since the UAV is all electric; while the balloon requires helium and the CubeSat requires a launch and orbit deployment.

3.5. Mission analysis

At this point is worth noting that the results presented thus far suggest that the best choice for balloon fly planning and design is C and for the nanosatellite the best orbit is C; while, for the fixed wing UAV the three designs complement each other. Consequently, the analysis presented next will concentrate on those platforms. As mentioned in the theoretical framework there are four main parameters that describe the performance of an RGB camera: spatial, spectral, temporal and radiometric resolution. In most cases these parameters are indifferent to the overall aerospace platform performance; however, their behavior can be affected with certain elements associated with each aerospace platform performance, such as location and distance from the object being imaged. Furthermore, parameters such as the overall IFOV of the image mainly depends on the objects distance to the camera. In addition, it is necessary to evaluate the area that each platform can cover and reach.

Figure 3.25 summarizes the main characteristics of the optical system picked for this study. Remember that the focal distance can be set manually for this optics with the results suggesting that the focal length can be adjusted withing a range of 16.81 to 17.52 mm. The maximum adjustment of 17.52 mm corresponds to an object´s distance of 6139.4 meters; after this the optics resolution cannot be adjusted further. Figure 3.25, b shows the effects of altitude on the focal distance up to 200 m; which, is the case of the fixed wing UAV. The object distance is important for the balloon and the fixed wing UAV to determine the magnification factor of the image with respect to the object, Figure 3.25, c. For the CubeSat the distance is too big to make any improvement on the image resolution; at that point what matters is the spatial resolution of the camera that tells if objects in the image can be resolved. The minimum GSD that this camera system requires to comply with effective spatial resolution is shown in Figure 3.26 together with the minimum GSD for each color

spectrum as a function of angular distance. The minimum angular ground sample distance between each pixel captured by the camera is 1.83 x 10^{-4} rad and is the same in the x and y dimensions since the pixel has equal dimensions. Notice that the color spectrum requires a smaller minimum GSD to be spatially resolved. The findings suggest that this RGB camera system is appropriate for all three platforms since the main characteristic that affects the spatial resolution is the lens aperture; which, is more than appropriate.

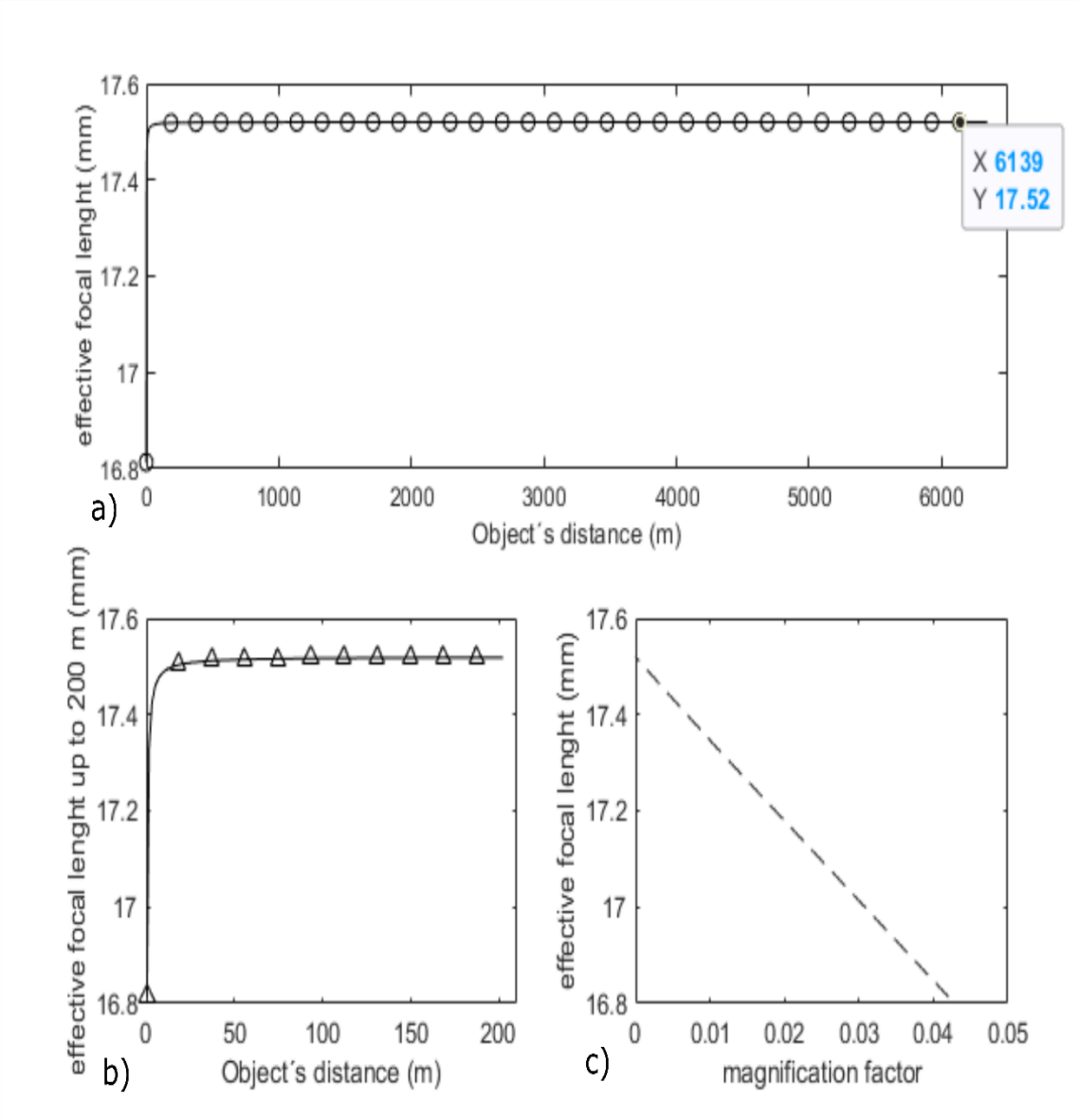

Figure 3.25. RGB camera characteristic parameters
(Source: own)

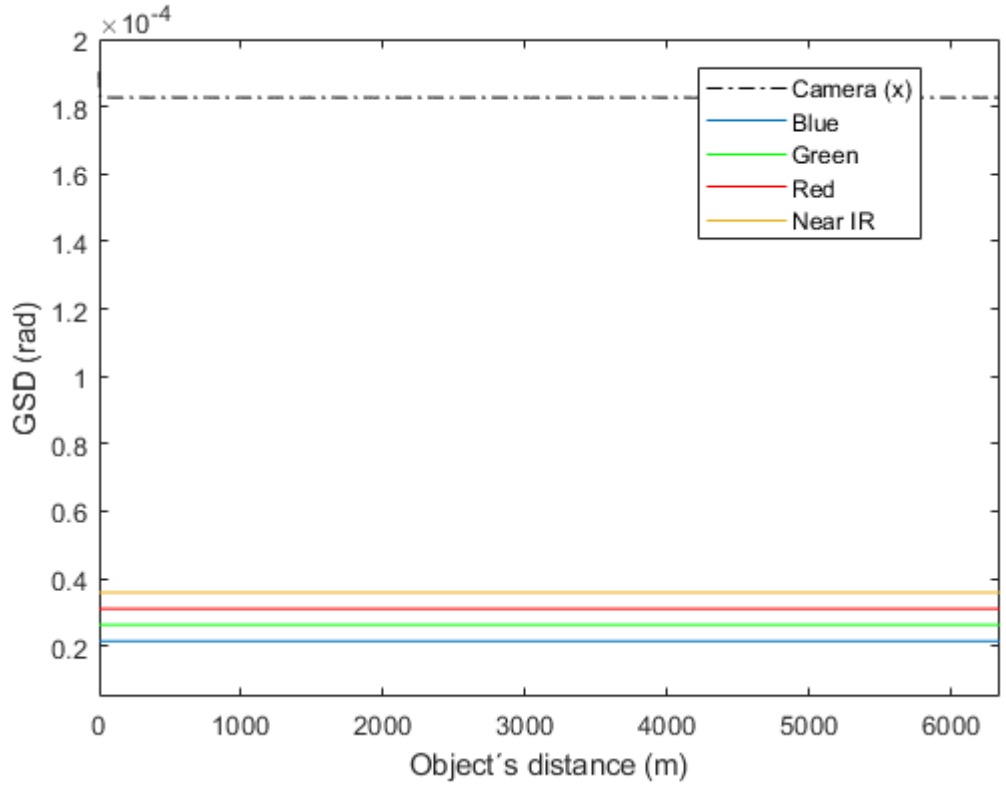

Figure 3.26. RGB camera spatial resolution
(Source: own)

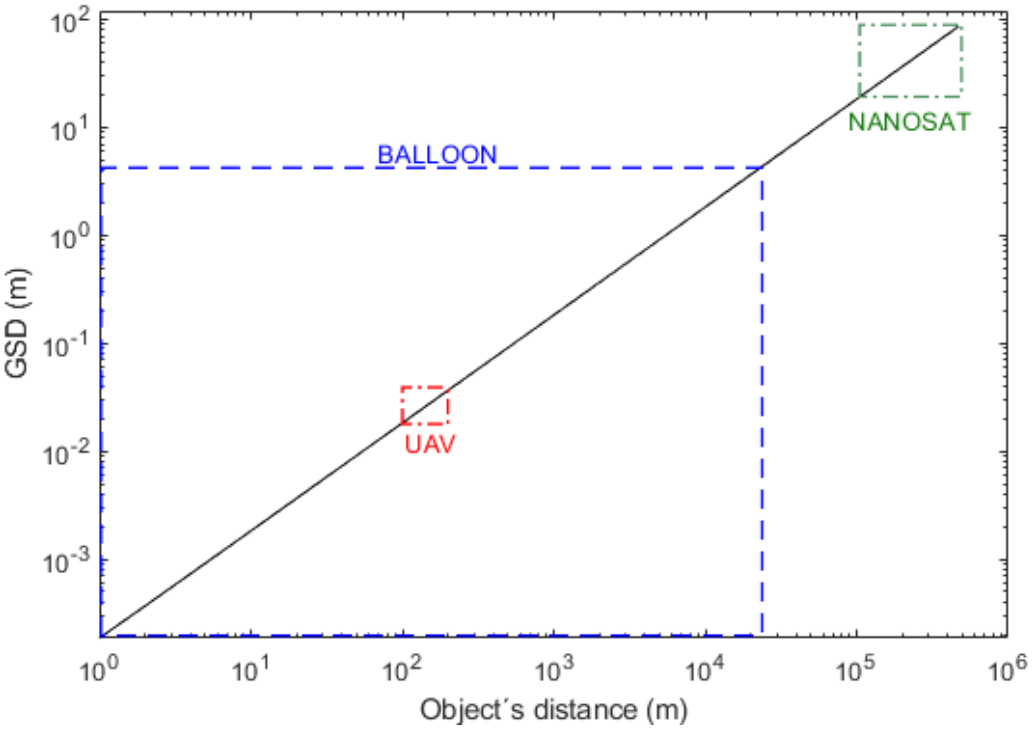

Figure 3.27. GSD for each aerospace platform class
(Source: own)

As previously mentioned, the above figure presents the information as a function of angular distance when translating that information to meters the object's distance comes to play. Figure 3.27 displays the GSD in meters for the three platforms in log scale. In the case of the UAV that fly at an altitude from the ground between 100 m to 200 m the GSD is between 0.0183 m to 0.365 m. For the balloon since it stars collection soon after flight can be around 5 meters at its highest altitude. And, for the nano-satellite is between 18.26 m and 86.27 m, considering that the orbit is considered useful until it falls to 100 km, after that altitude the nano-satellite will decay fast.

For the spectral resolution analysis Figure 1.2 is used to determine the average percentage of sunlight during the year, 47.52 %. As explained in section 1.1 cloud altitude is around 2 km so cloud coverage will only affect pictures that are taken above that altitude. Using this concept Table 3.5 summarizes the effect of the final number of pictures that are useful during the one-year mission. In addition, the table also compares the number of total images that each platform can take during a year, the fix wing UAV can take about twice as many as the balloon and 55 time more than the nano-satellite (MAX strategy). Furthermore, cloud coverage has a big effect on the Nano-satellite and balloon, while no effect on the UAV.

Table 3.5. Number of images collected by each platform after cloud coverage correction

	Collection Strategy	**Total images collected in a year**	**Number of images corrected for cloud coverage**
Balloon C	MAX	135786	79241
	High-rate	76494	48210
	Mid-rate	38064	24009
	Low-rate	10248	7407
Orbit C	JPEG	5237	2748
	BPM	5237	2748
Fix wing UAV	MAX	291580	291580
	High-rate	146522	146522
	Mid-rate	73444	73444
	Low-rate	14762	14762

(Source: own)

The case of the temporal resolution is similar to that of the spatial resolution; dependents on the camera system characteristics, in this case the frame rates introduced in Table 1.2. The following table summarizes the results. A higher duty cycle is better for detecting movement since it has a direct relationship to how many frames were taken. However, a

higher duty cycle affects the IFOV as shown in Figure 3.28. A smaller IFOV means a smaller area that is covered by the image. Figure 3.29Figure 3.30Figure 3.31 show examples of IFOV for each camera setting at specific altitudes.

Table 3.6. Temporal resolution for the RGB camera

Image format	Frame rate (fps)	T_{sample}(s)	C_{duty}
2048 x 1536 QXGA	12	0.0833	60
1600 x 1200 UXGA	20	0.0500	100
1280 x 1024 SXGA	27	0.0370	135
1024 x 768 XGA	43	0.0233	215
800 x 600 SVGA	65	0.0154	325
640 x 480 VGA	93	0.0108	465
1920 x 1080 HDTV1	18	0.0556	90
1280 x 720 HDTV2	39	0.0256	195

(Source: own)

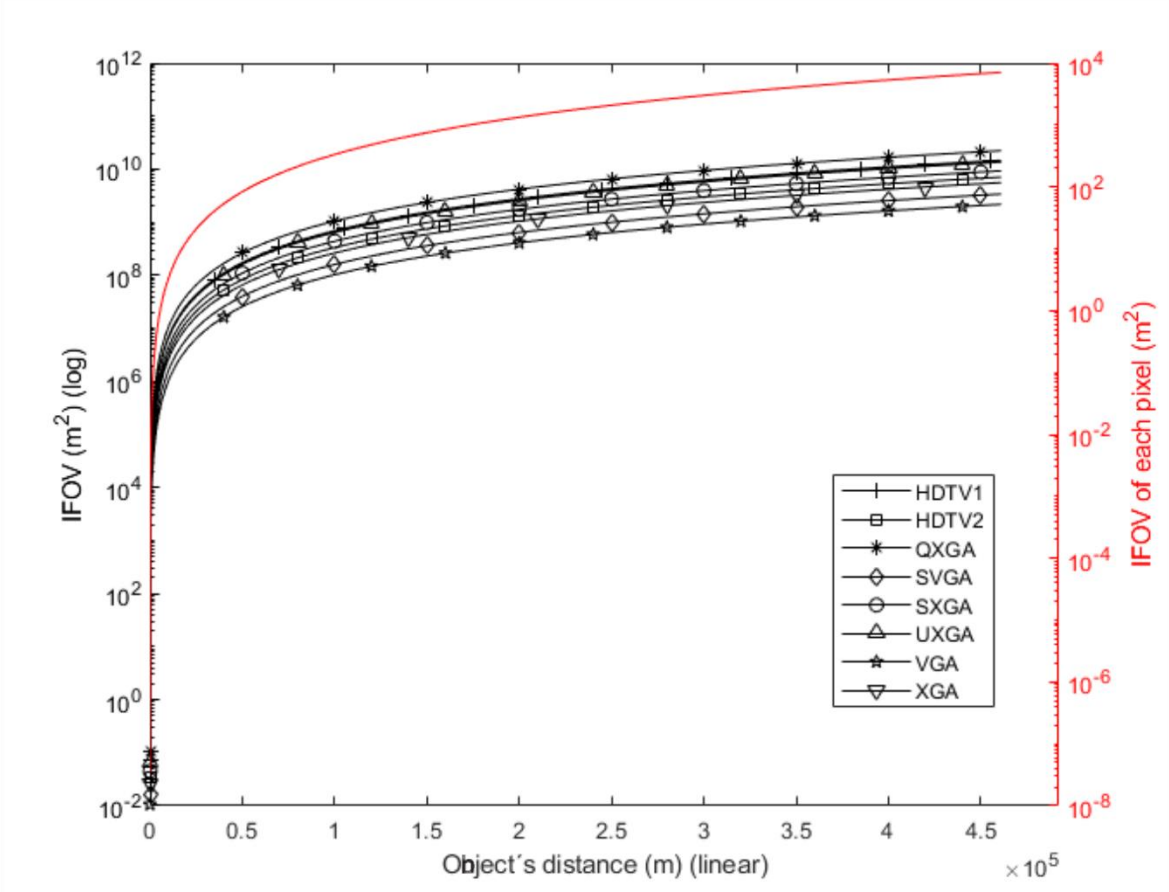

Figure 3.28. IFOV for each camera resolution
(Source: own)

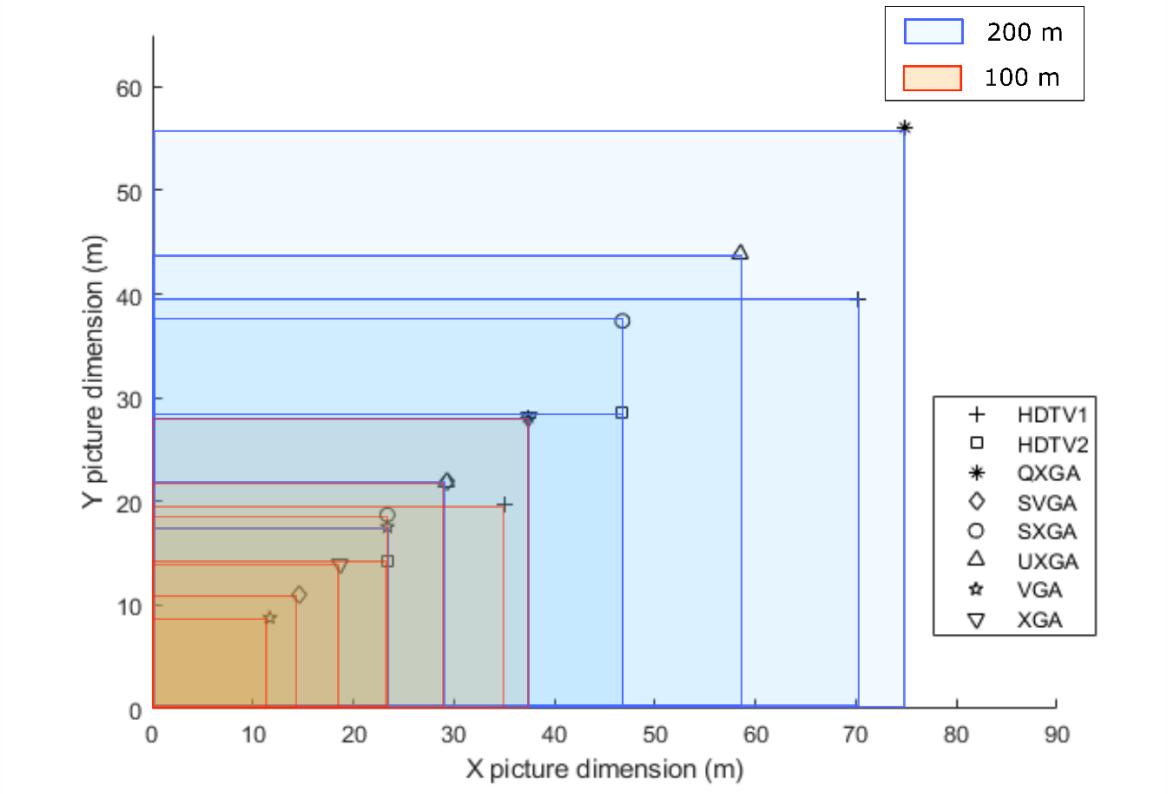

Figure 3.29. Image size for each camera resolution, fixed wing UAV
(Source: own)

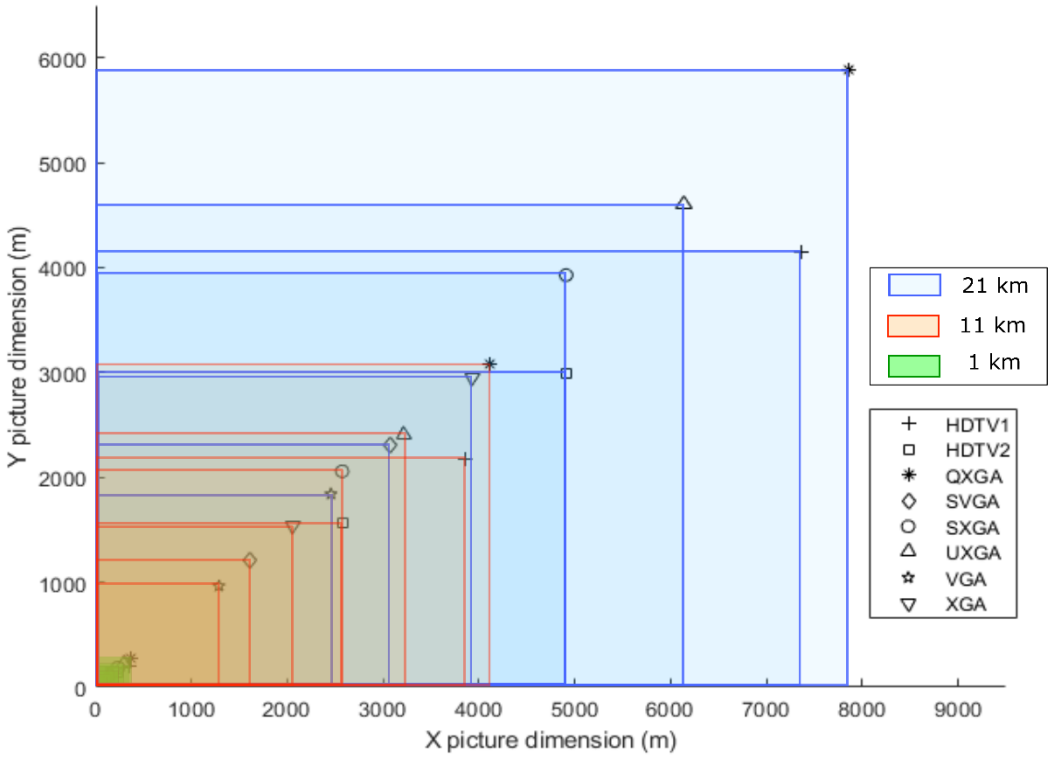

Figure 3.30. Image size for each camera resolution, balloon
(Source: own)

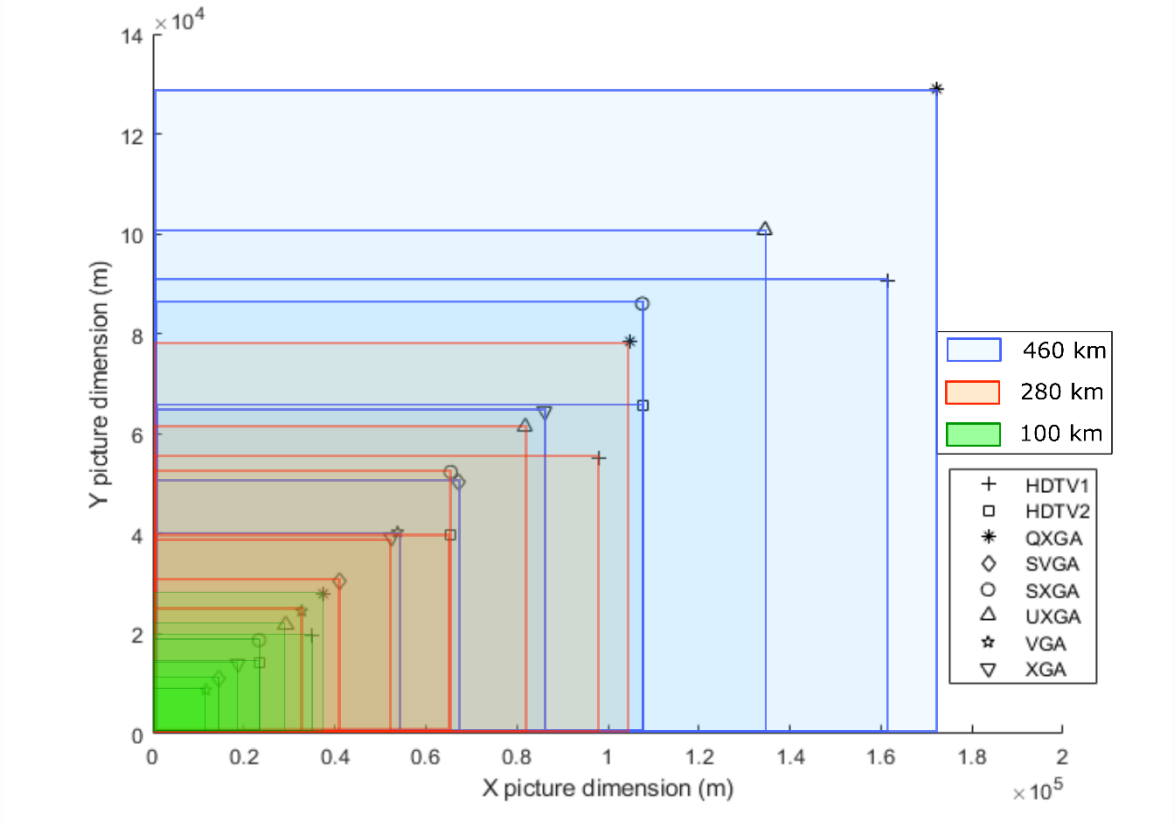

Figure 3.31. Image size for each camera resolution, nanosatellite
(Source: own)

As shown by the figures the VGA setting has the best duty cycle, but the smallest IFOV. Notice that the IFOV for the QXGA setting is more than 6 times larger than VGA; however, the VGA format offers an improvement in duty cycle of nearly 8 times. The user will have to decide if for a specific collection is better to go with a higher duty cycle or bigger coverage area. This may not be an issue for the nanosatellite since it has a large coverage area compared to the other two platforms. In the case of the balloon a larger coverage area is better because as mentioned earlier the trajectory is random and the image may not capture the desired target, therefore a bigger IFOV increases the chances of capturing the target. In the case of the UAV the size of the IFOV can become an issue because of the range previously mentioned. In this context, the UAV can use the range to do runs over an area to collect the desired data the size of this area will depend on the size of the IFOV and the range. Figure 3.32, shows an example to demonstrate this concept and Table 3.7 shows the estimated areas that can be covered with this technique. However, there will be holes in the image with this particular RGB camera because of the image acquisition and processing times that add up to 15 s, see Table 1.1. By considering the cruise speeds given

in Table 3.3, the UAVs will travel approximately 180 meters in those 15 s, three times the y dimension of the QXGA image at 100 m altitude, Figure 3.29.

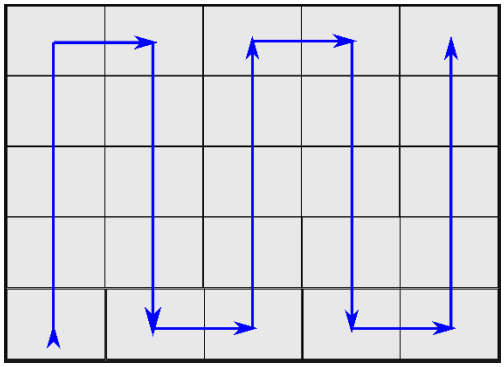

Figure 3.32. Area coverage strategy for fixed wing UAVs
(Source: own)

Table 3.7. Area coverage with the fixed wing UAVs

Image format	Area coverage, UAV A (km^2)		Area coverage, UAV B (km^2)		Area coverage, UAV C (km^2)	
	100 m	200 m	100 m	200 m	100 m	200 m
QXGA	9.50	5.04	11.15	5.80	10.65	5.63
UXGA	6.92	3.96	8.17	4.55	7.79	4.42
SXGA	5.26	3.42	6.24	3.93	5.94	3.82
XGA	3.81	2.52	4.57	2.90	4.33	2.82
SVGA	2.68	1.98	3.26	2.28	3.08	2.21
VGA	4.21	1.62	4.81	1.86	4.62	1.81
HDTV1	8.13	3.42	9.63	3.93	9.17	3.82
HDTV2	4.90	2.52	5.87	2.90	5.57	2.81

(Source: own)

Finally, the other RGB camera resolution analyzed is the radiometric resolution. As explained in section 1.1 this resolution is affected with the distance and therefore a signal factor was discussed. As expected, the balloon and the UAV have the best signal factor since they are closer to the object being imaged, Figure 3.33.

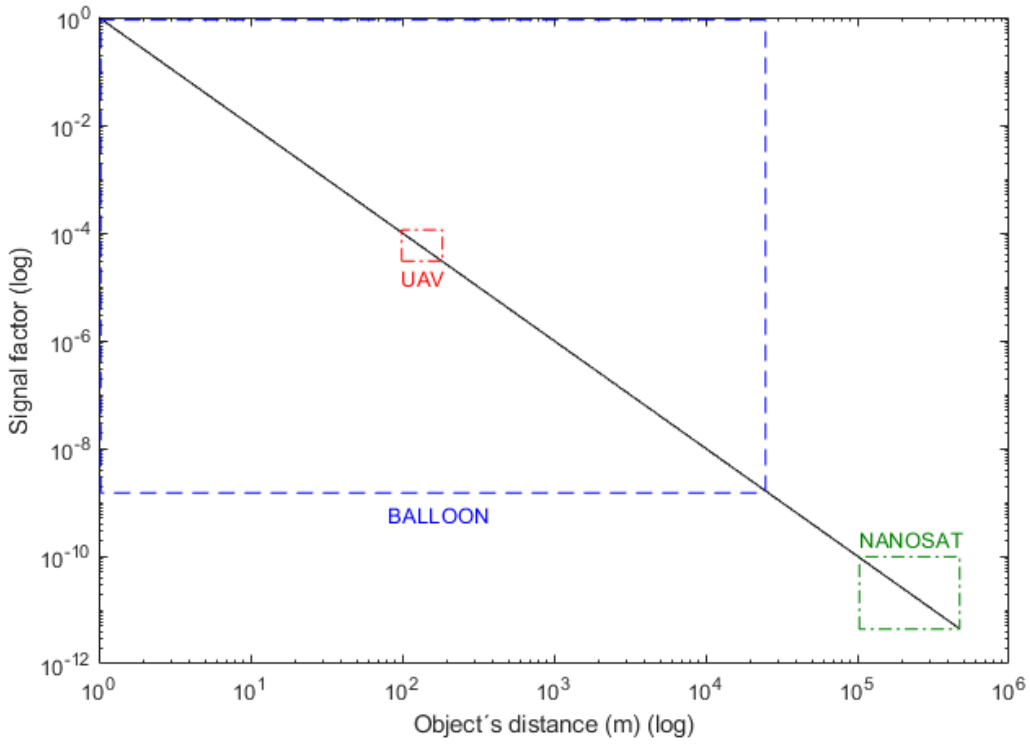

Figure 3.33. Radiometric resolution, all aerospace platforms
(Source: own)

3.6. Summary of results

Each platform has its strengths and weakness and to study this further three different designs were explored for each in the context of environmental monitoring with an RGB camera. In the case of the balloon the best design for this particular mission turned out to be balloon C, being the main driver for this conclusion the power requirement. However, in general the balloon presents a problem if the mission requires images at a specific location since the trajectory is unpredictable and difficult to control although there are some proposals to solve this problem, [53]. On the other hand, for the nanosatellite the design focus was on the orbit sine the CubeSat was the same in all cases, being orbit C the best choice. Orbit C presents the higher number of collection opportunities and contact windows, albeit with more current consumption, but the power system is capable of handling it as shown with the results. Orit A is an interesting option because it reduces the overall LCC of the nanosatellite by about 17%, because of free launch opportunities from the ISS [16]; however, its life is only about 160 days, short of the one-year requirement for the context of this study. The fixed wing UAVs also presented three options; nevertheless, the personalization nature for this platform allow for site specific design at little additional cost.

In this context, all three UAVs are combined for the one-year program in this analysis. After picking the best design for each platform the next step is to compare them using the four parameters described in Figure 2.1.

Flight autonomy is mostly related to power requirements. In this case the best aerospace platform is the nanosatellite because of the solar panels that give it a renewable source of energy, and as shown with the results all power needs are covered and the recharge capability are not hindered at all. On the other hand, the fixed wing UAV and the balloon both use batteries that cannot be charged during flight, Furthermore, the balloon needs another source of power, namely the helium to provide the required lift. In addition, the fixed wing UAV has a higher endurance than the balloon, nearly 65 % more. The main reason for this is the bigger battery that can be fitted and was specifically selected using the design procedure previously explained.

Area of operation has a wide context, it does not only mean the physical area that the images can cover, it also means the ability to take the images at the desired location. In addition, the number and quality of images come to play as well. The quality of the images can be measured with their spatial, spectral, temporal, and radiometric resolution. Since all three platforms use the same camera the performance parameters are the same; however, distance comes to play in spatial, spectral, and radiometric resolutions. Even though the distance of all platforms does not impair the main function of the camera and it accomplishes its mission, these resolutions are better when the object is closer to the camera, so in this case the UAV performs better. Furthermore, as demonstrated with the results cloud coverage has a direct effect on the number of useful images; which, in the case of the nanosatellite and the balloon this represents a loss of 47.5 % and 41.6% respectively (MAX collection strategy case). A good temporal resolution can detect change since it represents how many frames are taken in the image; however, improving the temporal resolution affects the area or size of the image. For the nanosatellite having an image setting to detect change may not affect the coverage area since the image is large enough due to distance, Figure 3.28. In the case of the UAV this may affect how much area it can cover as previously explained. And, in the case of the balloon, the higher it gets the bigger the coverage area; however, since the trajectory cannot be controlled, the balloon becomes unreliable if a specific area needs to be imaged.

The other factor that comes in review is the cargo capacity. This parameter is a straight forward calculation using the design information of each platform. The cargo capacity is directly related to the overall weight of the aerospace platform and the life cycle cost. In the case of the balloon probe a higher cargo capacity will imply higher cost for a balloon that

can carry more weight and additional cost for more helium. Notice that an increase of nearly 13 % in mass for balloon B compared to balloon A resulted in an LCC increase of 5% to have similar climb speeds. In the case of the nanosatellite, mass is the main variable to determine the launch cost, Annex F. On the other hand, weight is a design driver for the fixed wing UAV. This becomes evident since the first parameter determined by the models is the preliminary weight; which, became the building block for the other modules. Furthermore, an increase in payload weight implies a redesign of the whole UAV including geometry, aerodynamic assessment, and propulsion system selection. What is interesting to compare between the tree platforms is the payload to platform mass ratio presented in the next table. For the payload mass of the UAV and balloon the camera (106 g) plus the gimbal (230 g) was considered while for the nanosatellite the payload (106 g) plus the reaction wheel (60 g) was considered. These additional components are considered to be essential for the camera to operate correctly. The mass ratio provides a rough estimate on how much the weight of the platform will need to change to accommodate a bigger or smaller payload, influencing in the overall design and LCC. Consequently, a larger payload to platform mass ratio is desired, suggesting that a smaller frame is capable of providing support for a bigger and better payload. It is interesting to see that all three platforms have similar ratios even though as previously mentioned the payload of the nanosatellite occupies approximately 35% of the overall volume.

Table 3.8. Payload to platform mass ratios

Aerospace platform	Total mass (g)	Payload mass (g)	Payload to platform mass ratio
Balloon A	1956	336	0.17
Balloon B	2196	336	0.15
Nanosatellites	1050	166	0.16
Fixed wing UAVs	2039	336	0.16
Fixed wing UAVs (no gimbal)	2039	106	0.05

(Source: own)

Finally, the fourth parameter of importance for this analysis is the life cycle cost; which in fact has influence over the whole design. What came as a surprise is the important price difference between the LCC of the fixed wing UAVs compared to the other two platforms, 85.6% less than balloon C and 86.9% less than Orbit C. Also, of interest is the similarity in price between the balloon and the nanosatellite, only 8% more for the nanosatellite. The balloon defied first impression of being a cheap platform to becoming nearly as expensive as a nanosatellite in the context of the life cycle cost of a one-year program.

In this context, table 3.15 summarizes the findings thus far discussed in a comparative way. The criteria are as follows:

- Green: complies with mission with the following scores: 3: complies, 4: complies with good performance, 5 complies with best performance.
- Yellow: partially complies with mission with the following scores: 1: poorly complies, and 2: marginally comply.
- Red: does not comply with a score of 0.
- When considering the LCC, the ceiling for the cost is $200,000 is used; which, represents the maximum budget for an internal university research project. However, manhour costs are taken out because personnel from the university are employed to develop the project. The final LLC are as follows:
    - Weather balloons: $401,655.46
    - Nanosatellite: $438,419.72
    - Fixed Wing UAV: $24,399.60

Table 3.9. Environmental monitoring mission with an RGB camera compliance matrix

Parameter	Sub parameter	Balloon C	Orbit C	Fixed wing UAVs
Flight autonomy	Power available vs power required	3	5	3
	Power source	3	5	3
	Endurance	3	5	4
Total score		**9**	**15**	**10**
Area of Operation	Area coverage	4	5	4
	Specific target acquisition	0	3	5
	Number of images	4	3	5
	Quality of images	2	4	5
Total score		**10**	**15**	**19**
Cargo capacity*	Additional equipment needed	3	3	3
	Main design driver	5	5	3
	Mayor LLC driver	3	3	5
Total score		**11**	**11**	**11**
LCC	RDTE	5	3	4
	ACQ	0	3	5
	OPS	2	0	5
	DISP	3	3	5
Total Score		**10**	**9**	**19**
Overall score		**40**	**50**	**59**

* Sub parameter represents a difficulty
(Source: own)

4. CONCLUSIONS

This thesis proposes a methodology for selection of an aerospace platform for specific missions based on TEA analysis. The analyzed mission is environmental monitoring with an RGB camera. Four main indicators are created to arrive at the most appropriate platform for that specific task: flight autonomy, area of operation, cargo capacity, and life cycle cost for a one-year program. The results obtained are a product of design parameters and mathematical models created to gather information to feed these indicators. The results suggest that the most appropriate aerospace platform for this particular mission is the fixed wing UAV. In fact, the balloon demonstrated to be marginal performing poorly in the area of operation, especially in its inability to capture an image of a selected target. On the other hand, the nanosatellite is the most expensive platform, consequently not as cost effective as the fixed wing UAV. However, its technical performance is equal to the fixed wing UAV.

Other important finding is that the fix wing UAV presents a unique opportunity for site specific personalized design improving overall performance for flight at different altitudes at little additional cost. The other two platforms used in this study did not present that characteristic, instead design changes would imply significant additional cost and physical changes such as size. The UAV did change geometry for specific altitudes, but its mass remained the same. Furthermore, the balloon might have the misconception of being a cheap alternative, and in the perspective of unit cost it is; however, its poor performance for this particular task meant a significant life cycle cost. The nanosatellite finished in second place to the fixed wing UAV, not surprisingly it presented some advantages over the other two in flight autonomy because of its solar power system.

Another very interesting novelty is that the payload to platform mass ratio was the same for all three aerospace platforms. Changing the size of the camera to a bigger one will improve mission performance in all platforms with respect to resolution; nevertheless, the work presented in this thesis demonstrates that the main driver is the payload to platform mass ratio. The mass of the payload was considered in the design of all platforms studied, and played an important part in their mission performance. This suggests that the payload mass ratio has a similar effect as a design cost driver for all studied platforms.

The four indicators selected for this TEA proved to be enough to determine with significant support the best aerospace concept for the particular mission studied. This suggests that these four indicators can be useful when selecting aerospace platforms for other distinct missions. However, mathematical models will need to be tailored to gather results that support those studies.

Bibliography

[1] Asamblea Constituyente, "Constitución del Ecuador," Gobierno del Ecuador, 2008.

[2] Ministerio del Ambiente, "Sistema Nacional de Monitoreo de Bosques," Gobierno del Ecuador, Quito, 2017.

[3] S. Manfreda, M. F. Mccabe, P. E. Miller, L. Richard, V. M. Pajuelo, G. Mallinis, E. B. Dor, D. Helman and et al, "Use of Unmanned Aerial Systems for Environmental Monitoring," *Remote Sensing,* vol. 10(4), no. March, 2018.

[4] D. Ventura, A. Bonifazi, M. F. Gravina and G. D. Ardizzone, "Unmanned Aerial Systems (UASs) for Environmental Monitoring: A Review with Applications in Coastal Habitats," *Aerial Robots - Aerodynamics, Control and Applications,* no. September, 2017.

[5] Dow Centre, "Techno-Economic Analysis," The University of Queensland, Australia, [Online]. Available: http://www.dowcsei.uq.edu.au/technology. [Accessed 13 07 2018].

[6] M. Lauer, "Methodology guideline on techno economic assessment (TEA)," *ThermalNet WP3B Economics,* 2008.

[7] G. Liu, M. Li, B. Zhou, Y. Chen and S. Liao, "General indicator for techno-economic assessment of renewable energy resources," *Energy Conversion and Management,* vol. 156, no. November 2017, pp. 416-426, 2018.

[8] A. S. Belward and J. . O. Skøien, , "Who launched what, when and why; trends in global land-cover observation capacity from civilian earth observation satellites," *ISPRS Journal of Photogrammetry and Remote Sensing,* vol. 103, pp. 115-128, 2015.

[9] J. Roskam, Airplane Design, Lawrence: Design, Analysis and Research Corporation, 1997.

[10] H. E. Evans II, An Introduction to Electro-Optical and Overhead Non-Imaging Infrared Remote Sensing Collection Phenomenology and Data Processing, Analysis and Exploitation, Riverside Research Institute, Ed., Dayton: Air Force Institude of Technology, 2005.

[11] W. H. Bakker, W. Feringa, A. Gieske, B. G. H. Gorte, K. A. Grabmaier, C. A. Hecker, J. A. Horn, G. C. Huurneman, L. L. F. Janssen, N. Kerle, F. D. V. D. Meer, G. N. Parodi, C. Pohl, C. V. Reeves, F. J. V. Ruitenbeek, E. M. Schetselaar, K. Tempfli, M. J. C. Weir, E. Westinga and T. Woldai, Principles of Remote Sensing, An introductory textbook, Enschede, The Netherlands: The International Institute for Geo-Information Science and Earth Observation, 2009.

[12] J. B. Campbell and R. H. Wynne , Introduction to Remote Sensing, New York: The Guilford Press, 2011.

[13] H. E. Evans II, An Introduction to the Science and Phenomenology of Electro-Optical, Infrared, and Radar Remote Sensing as Applied to the Intelligence Community, Riverside Research Institute, Ed., Dayton: Air Force Institude of Technology, 2004.

[14] Y. Hernandez, "Nubosidad de Quito 2017," Observatorio Astronómico de Quito, Escuela Politécnica Nacional, Quito, 2017.

[15] "MT9T031 Image Sensor," Micron Technology, Inc, Boise, United States, 2006.

[16] D. Vera-Hensiek, E. López, J. Armijos, D. Benalcazar, D. Mena, G. Flores, S. Sandobalin, H. Llumiquinga and E. Celi, "OAQUBE_01 Nanosatellite Project "Ecuadorian Synchrotron Space Probe" - KiboCUBE CubeSat Mission Application for the Third Round," Observatorio Astronómico de Quito, Escuela Politécnica Nacional, Quito, Ecuador, 2018.

[17] Schneider Kreuznach, "Xenon-Ruby 2.2/25," Jos. Schneider Optische Werke GmbH, Bad Kreuznach, Germany, 2018.

[18] GOMspace, "NanoCam C1U Datasheet," GOMspace, Aalborg, Denmark, 2017.

[19] Y. Lee and K. Yee, "Numerical Prediction of Scientific Balloon Trajectories While Considering Various Uncertainties," *Journal of Aircraft,* vol. 54, no. 2, pp. 768-782, 2017.

[20] R. Palumbo, G. Morani and F. Corraro, "Effective Approach to Characterization of Prediction Errors for Balloon Ascent Trajectories," *Journal of Aircraft,* vol. 47, no. 4, pp. 1331-1337, 2010.

[21] P. Alexander, "A numerical study of open atmospheric balloon dynamics," *Physics of Fluids,* vol. 15, no. 10, pp. 3065-3077, 2003.

[22] A. Sóbester, H. Czerski, N. Zapponi and I. Castro, "Notes on Meteorological Balloon Mission Planning," in *AIAA 2013, A Balloon Systems (BAL) Conference*, Daytona Beach, Florida, 2013.

[23] Cambridge University Space, U.K. High Altitude Society, [Online]. Available: http://predict.habhub.org/.

[24] D. R. Downing and V. U. Muirhead, An introduction to Aerospace, fifth ed., Lawrence, KS: Department of Aerospace Enginnering, University of Kansas, 1998.

[25] P. Brien, "Notes on computing," *Society,* 1987.

[26] W. Y. Liang Ling and J. Balta, "Derivation of Basic Balloon Flight Dynamics".

[27] National Oceanic and Amospheric Administration, "U.S. standard Atmosphere, 1976," National Aeronautics and Space Administration, Washington, D.C., 1976.

[28] D. P. Drob, J. T. Emmert, J. W. Meriwether, J. J. Makela, E. Doornbos, M. Conde, G. Hernandez, J. Noto, K. A. Zawdie, S. E. McDonald, J. D. Huba and J. H. Klenzing, "An update to the Horizontal Wind Model (HWM): The quiet time thermosphere," *Earth and Space Science,* vol. 2, no. 7, pp. 301-319, 2015.

[29] "Electric Power – The Physics Hypertextbook," [Online]. Available: https://physics.info/electric-power/. [Accessed 19 11 2019].

[30] PVEducation, "Battery Capacity," [Online]. Available: https://www.pveducation.org/pvcdrom/battery-characteristics/battery-capacity. [Accessed 19 11 2019].

[31] "High Altitude Science," [Online]. Available: https://www.highaltitudescience.com/. [Accessed 19 11 2019].

[32] "Karma Tech Specs," Karma, 2019.

[33] T. Liu , "Dht22 (Am2302) Datasheet," Aosong ELectronics Co, Ltd., 2015.

[34] Microchip, "Mcp3004/3008 Datasheet," Microchip Technology Inc, 2008.

[35] Maxim Integrated Products, "MAX6675 Datasheet," Motorola, Inc., 2014.

[36] Pi In The Sky, "Pi In The Sky Installation Manual," Pi In The Sky, 2019.

[37] Raspberry Pi, "Raspberry Pi Compute Module 3+ Raspberry Datasheet," Raspberry Pi (Trading) Ltd., 2019.

[38] D. Vera-Hensiek, "Dinámica de Órbitas en el Espacio," in *Boletín Astronómico 2015*, Quito, Ecuador, Observatorio Astronómico de Quito, Escuela Politécnica Nacional, 2015.

[39] A. K. Maini and V. Agrawal, Satellite Technology, Third ed., Chichester: John Wiley & Sons Ltd, 2014.

[40] M. D. Griffin and J. R. French, Space Vehicle Desing, Blacksburg, Virginia: American Institute of Aeronautics and Astronautics, Inc, 2004.

[41] G. S. Aglietti, M. Bandecchi, F. Chatel, G. E. Dorrington, J. B. Farrow, N. P. Fillery, R. Francis, G. Hall, J. M. Houghton, B. Moss, T. Ransome, K. M. Redford , C. J. Savage, R. E. Sheriff, D. Stanton, M. N. Sweeting , A. R. Tatnall and G. I. Underwood, Spacecraft Systems Engineering, London: Wiley, 2011.

[42] S. Sanchez-Sanjuan , J. Gonzalez-Llorente and R. Hurtado-Velasco , "Comparison of the incident solar energy and battery storage in a 3U cubesat satellite for different orientation scenarios," *Journal of Aerospace Technology and Management,* vol. 8, no. 1, pp. 91-102, 2016.

[43] GMAT Development Team, General Mission Analysis Tool (GMAT): User Guide, R2018a ed., National Aeronautics and Space Administration, 2018.

[44] "Cubesat," California Polytechnic State University, San Luis Obispo and Stanford University's Space Systems Development Lab, [Online]. Available: https://www.cubesat.org/.

[45] "CubeSat Design Specification Rev 13," The CubeSat Program, Cal Poly, San Luis Obispo, 2014.

[46] JAXA, JEM Payload Accommodation Handbook - Small Satellite Deployment Interface Control Document, Japan Aerospac eExploration Agency, 2015.

[47] D. Vera-Hensiek, E. Lopez, J. Armijos, D. Benalcazar, S. Sandobalin , D. Mena, H. Llumiquinga and G. Flores, "Design of a university nano-satellite for space weather monitoring," in *Proceedings - 2019 7th International Engineering, Sciences and Technology Conference, IESTEC 2019*, Panama City, 2019.

[48] E. Valencia, D. Rodriguez, V. Alulema, D. Vera-hensiek and P. Mosquera, "Conceptual design and optimization methodology for Electric Fixed-Wing UAVs implemented in High Altitude Remote Sensing," *PREPRINT,* 2020.

[49] M. H. Sadraey, Aircraft Design, Chennai, India.: John Wiley & Sons, Ltd, 2013.

[50] E. Valencia, V. Hidalgo and D. Rodríguez, "Parametric modeling for aerodynamic assessment of a fixed wing UAV implemented for site specific management," in *AIAA Information Systems-AIAA Infotech at Aerospace*, Kissimmee, Florida, 2018.

[51] M. H. Sadraey, Aircraft Performance An Engineering Approach, Boca Raton, FL: Taylor & Francis Group, LLC, 2017.

[52] G. Avanzini, E. L. de Angelis and F. Giulietti , "Optimal performance and sizing of a battery-powered aircraft," *Aerospace Science and Technology,* vol. 59, pp. 132-144, 2016.

[53] D. Vera-Hensiek, E. Valencia , E. López and W. E. Banda, "Modeling a propulsion system for the trajectory correction of weather balloons," in *AIAA Propulsion and Energy 2019 Forum*, Indianapolis, IN, 2019.

[54] "XFOIL Subsonic Airfoil Development System," MI, GNU General Public License, [Online]. Available: https://web.mit.edu/drela/Public/web/xfoil/.

[55] D. Rodríguez, *MATLAB parametric fixed wing UAV preliminary design code,* Quito: Escuela Politécnica Nacional, 2020.

[56] Zippy-compact-8000mah-4s, "HobbyKing-com," Hobby King, 2020. [Online]. Available: https://hobbyking.com.

[57] Turnigy-high-capacity-battery-6600mah-4s, "HobbyKing.com," Hobby King, 2020. [Online]. Available: https://hobbyking.com.

[58] Zippy-compact-5800mah-4s, "HobbyKing.com," Hobby King, 2020. [Online]. Available: https://hobbyking.com.

[59] L. Meier, "Pixhawk 4 Technical Data Sheet," Dronecode Foundation, 2018.

[60] US Bureau of Labor Statistics, "Consumer Price Index," United States government, 2020. [Online]. Available: https://www.bls.gov/cpi/.

[61] L. W. Renegar, "A Survey of Current Balloon Trajectory Prediction Technology," University of Maryland, College Park, MD, 2017.

[62] GMAT Development Team, General Mission Analysis Tool (GMAT): Architectural Specifcation, Greenbelt, Maryland and Tucson, Arizona 85718: National Aeronautics and Space Administration, 2018.

[63] S. P. Hughes, R. H. Qureshi, S. D. Cooley, J. J. Parker and T. G. Grubb, "Verification and Validation of the General Mission Analysis Tool (GMAT)," in *AIAA SPACE Forum*, San Diego, 2014.

[64] R. H. Qureshi and S. P. Hughes , "Preparing general mission analysis tool for operational maneuver planning of the advanced composition explorer mission," in *AIAA/AAS Astrodynamics Specialist Conference* , San Diego, 2014.

[65] *Omega Electrónica proforma,* Octubre 9, 2016.

[66] B. J and J. Guo, "Survey of worldwide pico- and nanosatellite missions, distributions and subsystem technology," *Acta Astronautica,* vol. 67, no. 7-8, pp. 854-862, 2010.

[67] T-MOTOR, "T-Motor The Sefer Propulsion System," T-Motor, 2020. [Online]. Available: http://uav-en.tmotor.com/html/uav/html/company/about/.

[68] Bryce Space and Technology, "The Annual Compendium of Commercial Space Transportation: 2018," Federal Aviation Administration, Alexandria, VA, 2018.

[69] A. Bonnema, *Launch of a 1U in 2017 (email),* Innovative Solutions In Space B.V., 09/12/2015.

ANNEX A

EXAMPLE OF BALLOON FLIGHT POWER AND ENERGY REQUIREMENTS AND CONSUMPTION

Input data used in the calculation for balloon A:

- Flight time: 7840 seconds
- Time to reach 2 km altitude: 992 seconds
- Voltage supply for all components: 5.4 Volts
- Battery capacity: 2.5 Amps-hour

Calculation tables:

Table A.1. Maximum use strategy for balloon A

Component	Main function	Response time (s)	Power rating (W)	Use	Samples (#)	Operation time (s)	Energy req (Wh/flight)	Current (Ah)
Main computer	control and command	~	3,5	MAX		7840	**7,62222**	1,4115
Sensors	humidity / temperature	2	0,0033	MAX	3920	7840	0,00719	
	pressure	0,02	0,0357	MAX	392000	7840	0,07775	
	A/D Converter	0,02	0,0033	MAX	392000	7840	0,00719	
	thermocouple to digital converter	0,22	0,00825	MAX	35636	7840	0,01797	
Total							**0,11009**	0,0204
Comm module	communication and navigation		1,05	MAX	7840	7840	**2,28667**	0,4235
Camera	boot	15	1,3	MAX		15	0,00542	
	idle	~	0,38	MAX		0	0,00000	
	image acquisition	5	0,8	MAX	522	2608	0,57963	
	image processing	10	0,8	MAX	522	5217	1,15926	
	computation (other)		0,85			7825	1,84757	
Total							**3,59188**	0,6652

Table A.2. High rate use strategy for balloon A

Component	Main function	Response time (s)	Power rating (W)	Use	Samples (#)	Operation time (s)	Energy req (Wh/flight)	Current (Ah)
Main computer	control and command	~	3,5	MAX		7840	**7,62222**	1,4115
Sensors	humidity and temperature	2	0,0033	high rate	1568	3136	0,00287	
	pressure	0,02	0,0357	high rate	1568	31,36	0,00031	
	A/D Converter	0,02	0,0033	high rate	1568	31,36	0,00003	
	thermocouple to digital converter	0,22	0,00825	high rate	1568	344,96	0,00079	
Total							**0,00400**	0,0007
Comm module	communication and navigation		1,05	MAX		7840	**2,28667**	0,4235
Camera	boot	15	1,3			15	0,00542	
	idle	~	0,38			3424	0,36142	
	image acquisition	5	0,8	high rate	293	1467	0,32600	
	image processing	10	0,8	high rate	293	2934	0,65200	
	computation (other)		0,85			7825	1,84757	
Total							**3,19241**	0,5912

Table A.3. Mid rate use strategy for balloon A

Component	Main function	Response time (s)	Power rating (W)	Use	Samples (#)	Operation time (s)	Energy req (Wh/flight)	Current (Ah)
Main computer	control and command	~	3,5	MAX		7840	**7,62222**	1,4115
Sensors	humidity and temperature	2	0,0033	mid rate	784	1568	0,00144	
	pressure	0,02	0,0357	mid rate	784	15,68	0,00016	
	A/D Converter	0,02	0,0033	mid rate	784	15,68	0,00001	
	thermocouple to digital converter	0,22	0,00825	mid rate	784	172,48	0,00040	
Total							**0,00200**	0,0004
Comm module	communication and navigation		1,05	MAX		7840	**2,28667**	0,4235
Camera	boot	15	1,3			15	0,00542	
	idle	~	0,38			5625	0,59370	
	image acquisition	5	0,8	mid rate	147	734	0,16300	
	image processing	10	0,8	mid rate	147	1467	0,32600	
	computation (other)		0,85			7825	1,84757	
Total							**2,93568**	0,5436

Table A.4. Low rate use strategy for balloon A

Component	Main function	Response time (s)	Power rating (W)	Use	Samples (#)	Operation time (s)	Energy req (Wh/flight)	Current (Ah)
Main computer	control and command	~	3,5	MAX		7840	**7,62222**	1,4115
Sensors	humidity and temperature	2	0,0033	low rate	523	1045,333333	0,00096	
	pressure	0,02	0,0357	low rate	523	10,45333333	0,00010	
	A/D Converter	0,02	0,0033	low rate	523	10,45333333	0,00001	
	thermocouple to digital converter	0,22	0,00825	low rate	523	114,9866667	0,00026	
Total		~	0,05055				**0,00133**	0,0002
Comm module	communication and navigation		1,05	MAX		7840	**2,28667**	0,4235
Camera	boot	15	1,3			15	0,00542	
	idle	~	0,38			7238	0,76405	
	image acquisition	5	0,8	low rate	39	196	0,04346	
	image processing	10	0,8	low rate	39	391	0,08691	
	computation (other)		0,85			7825	**1,84757**	
Total			1,65				**2,747400833**	0,5088

ANNEX B

PARAMETERS, RESOURCES AND COMMANDS USED IN THE GMAT SIMULATIONS

Table B.1. Resources and their parameters used for the orbital models.

Resources	Parameters	Description
Common resources in all orbit simulations		
Solar system and its barycenter Includes the sun, all planets and the Earth's moon. The source of the ephemeris to create it is the DE405 file created and updated regularly by the JPL	GMAT default parameters	Gravitational parameters, masses, sizes, orientation, orbits, etc. of the sun, planets, and the Earth's moon
Coordinate systems Defines the origin of an axis system	MJ2000Eq	The ECI mentioned before with J2000 as epoch
	Local Vertical Local Horizontal (LVLH)	A non-inertial coordinate system based on the position of the spacecraft with respect to Earth, being this the x-axis. The y-axis is the normal of the orbit and the z-axis completes the right-hand rule. This coordinate system is useful for the satellite´s attitude simulation.
BuhoSat	Physical properties	Mass (1.02 kg), drag area (0.01135 m^2) (from the BuhoSat design parameters), C_D (2.2), coefficient of reflectivity (1.8), (default values), SRP Area (0.00078 m^2) (extrapolated from ISS value)
	Attitude	Nadir pointing attitude using a local coordinate system (LVLH) previously created.
	Power system	P31U (described next)
Power system A model of the power system used in the BuhoSat (P31U) to determine power generated as a function of time and distance from the sun.	P31U parameters	Epoch, initial max power, decay rate, bus coefficient 1
	Solar power function parameters	Default solar coefficients from GMAT that define the function

BuhoSat antenna Transmits and receives radio frequency signals (created using the script)	There are no parameters	The antenna is a resource that needs to be created to associate the radio signal from the ground station
Buhosat receiver (created using the script)	ID number	The receiver must have an identifier and be attached to an antenna resource
Ground Station The facility fixed on Earth's surface used to transmit and receive signal from the spacecraft (can be created using the GUI but must have the antenna, receiver, and transmitter resources added to it and they can only be created with the script)	ID number	A number to identify the ground station used, the simulation only uses one ground station
	Minimum Elevation	The minimum elevation angle for data to be output representing the line of sight of the satellite to the ground station, it is set as 10 degrees.
	Location	The location of the ground station was given in latitude, longitude, and altitude using a spherical coordinate system with an ellipsoid horizon reference
Ground station antenna	N/A	Same as the BuhoSat antenna
Ground station receiver	ID number	Different Id number than the BuhoSat receiver
Ground station transceiver	Frequency	450 MHz
Propagator Is the resource that is used to model the spacecraft motion. There are two types: numerical integrator that also requires a force model and ephemeris propagator. These models use the numerical type.	Numerical integrator	The integrator, PrinceDormand78 was used setting MinStep to 0 as recommended. The other parameters are set to the GMAT default values
	Force model environmental forces and dynamics that affect motion of a spacecraft	Error control: RSSStep (root sum square relative to the current step in the numerical integrator)
		Central body and primary body are set to Earth
		Gravity model: the simulations use the Joint gravity model 3 (JGM3-) called by GMAT
		Drag: drag forces are calculated using the Jacchia-Roberts atmosphere model
		Point masses: additional point masses used are the moon and the sun
		SRP model: spherical model with GMAT default parameters
		No relativistic correction is needed at this close distances

Differential Corrector A numerical solver used to solve boundary value problems like orbit maneuvers and decay conditions.	Algorithm	NewtonRaphson: a quasi-Newton root finding method that computes the Jacobian using finite differencing
	Derivative Method	Forward difference
	Maximum iterations	The default value of 25 was used
	Output	Is set to show progress and to generate a normal report file
Orbit A		
Coordinate systems Defines the origin of an axis system	Velocity Normal Binormal (VNB)	A non-inertia coordinate system based on the motion of the spacecraft with respect to a set origin, in this case the origin is the Earth. The x-axis is along the velocity of the spacecraft with respect to earth, the y-axis is the normal of this orbit, and z-axis completes the right-hand rule. This coordinate system is useful for the modeling of impulses.
ISS International space station	Epoch set as UTC Gregorian	From ephemeris data obtained on Mar 12 Mar 2018
	Keplerian elements	From ephemeris data obtained on Mar 12 Mar 2018 using the MJ2000Eq coordinate system
	Physical properties	Mass, C_D, Drag area, Coefficient of reflectivity, SRP Area (from a sample script in the GMAT documentation)
BUHOSAT	Epoch set as UTC Gregorian	From ephemeris data obtained on Mar 12 Mar 2018 for the ISS
	Keplerian elements	From ephemeris data obtained on Mar 12 Mar 2018 for the ISS using the MJ2000Eq coordinate system
Impulse (burn in GMAT) Model of the impulse generated from the J-SSOD	Coordinate system	Must be local (spacecraft), with the Earth as the origin and using the VNB coordinate system
	Delta-V vector	The initial velocity produced by the impulse (-0.001202, 0, -0.001202) km/s
Orbit B		
BUHOSAT Finding the best semi-mayor axis for one-year orbit	Epoch set as UTC Gregorian	Same as Orbit A

	Keplerian elements	Same as Orbit A except for (a) The semi-mayor axis was increased from Orbit A with the following steps: 25 km, 30 km, 40 km, 50 km, 75 km, and 100 km.
BUHOSAT 50 km increase in (a) was chosen as Orbit B	Keplerian elements	Same as Orbit A, but with a semi-mayor axis 50 km higher
Orbit C		
BUHOSAT (near equatorial orbit)	Epoch set as UTC Gregorian	Same as Orbit A and B
	Keplerian elements	Same as Orbit B except for the inclination. *(i)* was set as 0.6221

(Source: Reference [43] [62] [46])

Table B.2. Commands to run the orbit simulations.

Command	Description
Orbit A	
Prop to Apoapsis	Uses the propagator described in the previous table to generate the orbit until the nanosatellite reaches apoapsis
Create Target	Generate a target named orbit life and set it to use differential corrector solver previously created (table 2.2). The target is the start of the command sequence.
Set parameters for the differential corrector	GMAT standard parameters and limits were used
Maneuver Impulse from ISS	Use the burn previously created to command the impulse when apoapsis is reached
Prop to test	Uses the propagator described in the previous table to generate initial orbits needed for the next step
Achieve ECC	Uses the differential corrector until the orbits achieve an eccentricity set as 0.0015 with a 0.1 tolerance.
Prop to decay	Uses the propagator described in table 2.2 to generate orbits until the altitude reaches 100 km
Achieve Alt	Uses the differential corrector until the orbits reach 100 km altitude with a 0.1 tolerance.
End Target	Finishes the mission sequence started with the Target creation
Orbit B	

Prop to decay	Uses the propagator described in table 2.2 to generate orbits until the altitude reaches 100 km (This was used for the orbit B interactions to find the final orbit B)
Prop for one year	Uses the propagator described in table 2.2 to generate orbits for a year
Orbit C	
Prop for one year	Uses the propagator described in table 2.2 to generate orbits for a year
Mission command for solar power data sample gathering for all Orbits	
Prop for 1/2 days	Uses the propagator described in table 2.2 to generate orbits for 12 hrs

(Source: own)

Table B.3. GMAT output resources

Output Resource	Description
Altitude plot	Plots orbit altitude with days in the x axis and altitude in the y axis
Power data	Collects data for the power system: days, power required and power available
Period data	Collects the number of periods and their duration for the life of the orbits
Altitude data	Similar as the plot, but the data is collected so that it can be used in other programs such as MATLAB
Eclipse Locator	Collects data regarding umbra penumbra and antumbra including their duration
Contact Locator	Collect data regarding contact information with the ground station including dates, start time, end time and contact duration

(Source: own)

ANNEX C

EXAMPLE OF ORBIT POWER AND ENERGY REQUIREMENTS AND CONSUMPTION

Input data used in the calculation for Orbit A:

- Mean orbit period: 7840 seconds
- Sunlight time: 63.36%
- Umbra time: 36.64%
- Average contact window: 274.95 seconds
- Telemetry download time: 24 seconds
- JPEG image download time: 87 seconds
- BMP image download time: 289 seconds

Calculation tables:

Table B.1. Power and energy requirements for the initial power-on orbit, Case A

Component	Power rating (W)	Voltage (V)	Sunlight (s)	Umbra (s)	Total energy required (Wh)	Solar panels energy (Wh)	Battery energy (Wh) (sunlight)	Battery energy (Wh) (umbra)	Battery current (Ah)
Battery heaters	3,000	8,4		2000,36	1,6670			1,6670	0,1984
EPS module	0,160	3,3	3459,14	2000,36	0,2426	0,1537		0,0889	0,0269
Magnetorquers (2)	0,162	3,3	3459,14	2000,36	0,2457	0,1557		0,0900	0,0273
Reaction wheel	0,120	8,4	3459,14	2000,36	0,1820		0,1153	0,0667	0,0217
RGB Camera (boot)	1,300	3,3	15,00		0,0054	0,0054			
RGB Camera (idle)	0,380	3,3	3444,14	2000,36	0,5747	0,3635		0,2111	0,0640
RGB Camera (op)	1,650	3,3							
Main computer	0,370	3,3	3459,14	2000,36	0,5611	0,3555		0,2056	0,0623
Interface PCB	0,132	3,3	3459,14	2000,36	0,2002	0,1268		0,0733	0,0222
Electric knifes	3,528	8,4	1,00		0,0010		0,0010		0,0001
Antenna	0,600	3,3	276,73	160,03	0,0728	0,0461		0,0267	0,0081
Comm module (Rx)	0,182	3,3							
Comm module (Tx)	2,640	3,3	276,73	160,03	0,3203	0,2029		0,1174	0,0356

Table B.2. Power and energy requirements for non-collection and non-contact orbits, Case A

Component	Power rating (W)	Voltage (V)	Sunlight (s)	Umbra (s)	Total energy required (Wh)	Solar panels energy (Wh)	Battery energy (Wh) (sunlight)	Battery energy (Wh) (umbra)	Battery current (Ah)
Battery heaters	3,000	8,4		2000,36	1,6670			1,6670	0,1984
EPS module	0,160	3,3	3459,14	2000,36	0,2426	0,1537		0,0889	0,0269
Magnetorquers (2)	0,162	3,3	3459,14	2000,36	0,2457	0,1557		0,0900	0,0273
Reaction wheel	0,120	8,4	3459,14	2000,36	0,1820		0,1153	0,0667	0,0217
RGB Camera (boot)	1,300	3,3							
RGB Camera (idle)	0,380	3,3	3459,14	2000,36	0,5763	0,3651		0,2111	0,0640
RGB Camera (op)	1,650	3,3							
Main computer	0,370	3,3	3459,14	2000,36	0,5611	0,3555		0,2056	0,0623
Interface PCB	0,132	3,3	3459,14	2000,36	0,2002	0,1268		0,0733	0,0222
Electric knifes	3,528	8,4							
Antenna	0,600	3,3	276,73	160,03	0,0728	0,0461		0,0267	0,0081
Comm module (Rx)	0,182	3,3							
Comm module (Tx)	2,640	3,3	276,73	160,03	0,3203	0,2029		0,1174	0,0356

Table B.3. Power and energy requirements for non-collection and contact orbits, Case A

Component	Power rating (W)	Voltage (V)	Sunlight (s)	Umbra (s)	Total energy required (Wh)	Solar panels energy (Wh)	Battery energy (Wh) (sunlight)	Battery energy (Wh) (umbra)	Battery current (Ah)
Battery heaters	3,000	8,4		2000,36	1,6670			1,6670	0,1984
EPS module	0,160	3,3	3459,14	2000,36	0,2426	0,1537		0,0889	0,0269
Magnetorquers (2)	0,162	3,3	3459,14	2000,36	0,2457	0,1557		0,0900	0,0273
Reaction wheel	0,120	8,4	3459,14	2000,36	0,1820		0,1153	0,0667	0,0217
RGB Camera (boot)	1,300	3,3							
RGB Camera (idle)	0,380	3,3	3459,14	2000,36	0,5763	0,3651		0,2111	0,0640
RGB Camera (op)	1,650	3,3							
Main computer	0,370	3,3	3459,14	2000,36	0,5611	0,3555		0,2056	0,0623
Interface PCB	0,132	3,3	3459,14	2000,36	0,2002	0,1268		0,0733	0,0222
Electric knifes	3,528	8,4							
Antenna	0,600	3,3	291,94	168,82	0,0768	0,0487		0,0281	0,0085
Comm module (Rx)	0,182	3,3	174,21	100,74	0,0139	0,0088		0,0051	0,0015
Comm module (Tx)	2,640	3,3	291,94	168,82	0,3379	0,2141		0,1238	0,0375

Table B.4. Power and energy requirements for collection (JPEG) and contact orbits, Case A

Component	Power rating (W)	Voltage (V)	Sunlight (s)	Umbra (s)	Total energy required (Wh)	Solar panels energy (Wh)	Battery energy (Wh) (sunlight)	Battery energy (Wh) (umbra)	Battery current (Ah)
Battery heaters	3,000	8,4		2000,36	1,6670			1,6670	0,1984
EPS module	0,160	3,3	3459,14	2000,36	0,2426	0,1537		0,0889	0,0269
Magnetorquers (2)	0,162	3,3	3459,14	2000,36	0,2457	0,1557		0,0900	0,0273
Reaction wheel	0,120	8,4	3459,14	2000,36	0,1820		0,1153	0,0667	0,0217
RGB Camera (boot)	1,300	3,3							0,0000
RGB Camera (idle)	0,380	3,3	3459,14	2000,36	0,5763	0,3651		0,2111	0,0640
RGB Camera (op)	1,650	3,3		15,00	0,0069			0,0069	0,0021
Main computer	0,370	3,3	3459,14	2000,36	0,5611	0,3555		0,2056	0,0623
Interface PCB	0,132	3,3	3459,14	2000,36	0,2002	0,1268		0,0733	0,0222
Electric knifes	3,528	8,4							0,0000
Antenna	0,600	3,3	347,06	200,70	0,0913	0,0578		0,0334	0,0101
Comm module (Rx)	0,182	3,3	174,21	100,74	0,0139	0,0088		0,0051	0,0015
Comm module (Tx)	2,640	3,3	347,06	200,70	0,4017	0,2545		0,1472	0,0446

Table B.5. Power and energy requirements for collection (BMP) and contact orbits, Case A

Component	Power rating (W)	Voltage (V)	Sunlight (s)	Umbra (s)	Total energy required (Wh)	Solar panels energy (Wh)	Battery energy (Wh) (sunlight)	Battery energy (Wh) (umbra)	Battery current (Ah)
Battery heaters	3,000	8,4		2000,36	1,6670			1,6670	0,1984
EPS module	0,160	3,3	3459,14	2000,36	0,2426	0,1537		0,0889	0,0269
Magnetorquers (2)	0,162	3,3	3459,14	2000,36	0,2457	0,1557		0,0900	0,0273
Reaction wheel	0,120	8,4	3459,14	2000,36	0,1820		0,1153	0,0667	0,0217
RGB Camera (boot)	1,300	3,3							0,0000
RGB Camera (idle)	0,380	3,3	3459,14	2000,36	0,5763	0,3651		0,2111	0,0640
RGB Camera (op)	1,650	3,3		15,00	0,0069			0,0069	0,0021
Main computer	0,370	3,3	3459,14	2000,36	0,5611	0,3555		0,2056	0,0623
Interface PCB	0,132	3,3	3459,14	2000,36	0,2002	0,1268		0,0733	0,0222
Electric knifes	3,528	8,4							0,0000
Antenna	0,600	3,3	475,05	274,71	0,1250	0,0792		0,0458	0,0139
Comm module (Rx)	0,182	3,3	198,32	114,68	0,0158	0,0100		0,0058	0,0018
Comm module (Tx)	2,640	3,3	475,05	274,71	0,5498	0,3484		0,2015	0,0610

ANNEX D

AMPR weight correction factor

Small Satellite classification:

- Pico: 0.1 kg to 1 kg
- Nano: 1 kg to 10 kg
- Micro: 10 kg to 100 kg
- Small: 100 kg to 500 kg

Table C.1. Weight correction table

Nano mass (kg)	Nano mass (lbs)	Equivalent mass (lbs)
1	2.2	5000
2	4.4	111100
3	6.6	222200
4	8.8	333300
5	11	444400
6	13.2	555500
7	15.4	666600
8	17.6	777700
9	19.8	888800
10	22	999900

Steps to find the corrected AMPR weight used in the LCC calculator:

1. Determine the structure to platform mass ratio
2. interpolate for values between table values
3. Multiply the Equivalent mass with the structure to platform mass ratio

✓ **The LCC calculator incorporates the correction factor**

ANNEX E

BALLOON SUPPLEMENTARY COST INFORMATION

Table D.1. Payload cost breakdown by component

Component	Unit price	Quantity	Price
CMOS	$20,00	1	$20,00
Chip	$10,00	1	$10,00
F-RAM	$6,00	1	$6,00
eMMC	$20,00	1	$20,00
DDR2	$4,00	1	$4,00
NOR	$8,00	1	$8,00
CAN	$4,00	1	$4,00
I2C	$2,00	2	$4,00
RS422	$6,00	1	$6,00
CVCC	$1,00	1	$1,00
GND	$4,00	1	$4,00
GOSH	$5,00	1	$5,00
USB	$4,00	1	$4,00
FRAM/RTC	$15,00	1	$15,00
temp sensor	$3,00	2	$6,00
Voltage sensor	$4,00	3	$12,00
I s connector	$5,00	3	$15,00
Digital to analog converter	$22,00	3	$66,00
sensor interface	$3,00	9	$27,00
PCB with shield	$100,00	1	$100,00
Lens (optics)	$517,05	1	$517,05
TOTAL			$854,05

Table D.2. Balloon cost breakdown

Components	Price A	Price B	Price C
Probe electronics	$499,30	$499,30	$499,30
Materials	$31,80	$31,80	$31,80
Parachute 1.5 m	$200,29	$200,29	$200,29
Balloon	$93,47	$156,90	$93,47
Payload	$854,05	$854,05	$854,05
Total	$1.678,91	$1.742,34	$1.678,91

Table D.3. Direct operational cost (flight) supplementary information for the balloon

Cost Component	Balloon A	Balloon B	Balloon C
Manhour cost			
Hourly rate (engineer) (USD)	$5,88	$5,88	$5,88
Flight time (hours)	2,18	2,76	1,55
Preparation and recovery (hours)	8,18	8,76	7,55
Tracking and monitoring (hours)	2,51	3,10	1,88
Total man hour (3 engineers) (hours)	12,87	14,62	10,98
Total program manhour, 365 launches (hours)	4696,33	5335,99	4007,09
Total manhour cost, 365 launches (USD)	$27.614,43	$31.375,65	$23.561,69
Helium cost			
Helium ($/m3)	$67,03	$67,03	$67,03
Helium volume (m3)	2,7947	3,0792	3,0487
helium cost per launch (USD)	$187,33	$206,40	$204,35
Helium cost 365 launches (USD)	$68.374,99	$75.335,55	$74.589,34
TOTAL (USD)	$95.989,42	$106.711,20	$98.151,03

Table D.4. Direct operational cost (maintenance) supplementary information for the balloon

Cost Component	All balloons
Manhour cost	
Hourly rate (engineer) (USD)	$5,88
Maintenance time (hours)	2
Weakly maintenance, 52 weeks (USD)	$611,52
Material cost	
10% material cost per flight (USD)	$3,18
program material cost, 365 flights (USD)	$1.160,70
Replacement parts cost	
Value to calculate component cost (USD)	$1.772,22
10% component cost (USD)	$177,22
TOTAL (USD)	$1.949,44

ANNEX F

NANOSATELLITE SUPPLEMENTARY COST INFORMATION

Table E.1. Nanosatellite components and materials cost

	Orbit A	Orbit A	Orbit A
Main components	$86.900,00	$82.120,50	$82.120,50
Materials			
Aluminum	$77,63	$77,63	$77,63
Face cover	$65,00	$65,00	$65,00
Mylar	$50,00	$50,00	$50,00
Thermal grease	$24,00	$24,00	$24,00
Liquid Teflon	$5,00	$5,00	$5,00
Screws	$10,00	$10,00	$10,00
Total material cost	$231,63	$231,63	$231,63

Table E.2. Launch cost of different vehicles per mass

Vehicle	MASS to Orbit (kg)		Price per launch (USD million)	Price per kg (USD thousand)	
	Low LEO	High LEO		Low LEO	High LEO
Antares	7000	3500	85	12,14	24,29
Atlas V	18123	8123	230	12,69	28,31
Falcon 9	13150	13150	61,2	4,65	4,65
Minotaur-C	1458	1278	50	34,29	39,12
Pegasus XL	450	450	40	88,89	88,89

Commercialization factor

Mean cost to the provider (USD thousand per Kg)	$30,53	$37,05
Price third party (1U ~ 1kg)	$85,00	$110,00
Commercial additional cost	$2,78	$2,97

Height scale

LEO Altitude (km)	
Low LEO (km)	200
High LEO (km)	900
Range	700

Cost per km (altitude)

Increase by Km (provider)	$9,31
Increase by km (commercial)	$35,71

Orbit Costs	
Orbit A (410 km)	$92.500,00
Orbit B (460 km)	$94.285,71
Orbit C (460 km)	$94.285,71

Figure E.1. Calculation of launch cost foe specific altitudes

Table E.2 and figure E.1 are used to estimate launch costs of a nanosatellite per mass. Table E.2 list known prices per kg from the Annual Compendium of commercial Space Transportation, 2018 [68]. Furthermore, an actual quote from Innovative Solutions in Space [69] was used to determine the commercialization factor to add to final costs. Figure E.1. shows the results. The calculation uses a range of altitude to determine the final launch cost for a particular altitude using the commercial adjusting factor.

Table E.3. Direct operational cost (flight) supplementary information for the nanosatellite

Cost Component	Orbit A	Orbit B	Orbit C
Manhour cost			
Hourly rate (engineer) (USD)	$5,88	$5,88	$5,88
Number of contact windows in year (#)	373	985	5237
Average duration of contact window (min)	4,58	6,12	7,42
program monitoring time, contact windows (min)	1709,27	6031,81	38840,21
Additional monitoring time, 20 min per contact orbit (min)	7460,00	19700,00	104740,00
Total monitoring time (min)	9169,27	25731,81	143580,21
Analysis engineer, one hour per day (hours)	365	365	365
Total manhour (hours)	517,82	793,86	2758,00
Total man hour cost (2 engineers) (USD)	$3.044,79	$4.667,92	$16.217,06
Launch & deployment cost			
Launch & deployment	0*	$94.285,71	$94.285,71
Total flight operation cost	$3.044,79*	$98.953,63	$110.502,77

* Assuming free launch opportunity from the ISS

Table E.4. Direct operational cost (maintenance) supplementary information for the nanosatellite

Cost Component	All Orbits
Hourly rate (engineer) (USD)	$5,88
Maintenance time per anomaly (hours)	4
52% of the year (number of anomalies)	190
Manhour cost to fix anomalies (2 engineers) (USD)	$8.937,60

ANNEX G

FIXED WING UAV SUPPLEMENTARY COST INFORMATION

Table F.1. Nanosatellite components and materials cost

	UAV A	UAV B	UAV C
Main component			
Avionics	$380,00	$380,00	$380,00
PIXHAWK 4	$475,00	$475,00	$475,00
Propellers	$28,50	$28,50	$38,00
Electric motor	$95,00	$95,00	$95,00
ESC	$114,00	$114,00	$114,00
Battery	$129,20	$91,20	$106,40
Material			
Balsa wood (30%) ($350/kg)	$123,50	$150,42	$162,38
EPS (65%) ($110/kg)	$84,10	$102,43	$110,57
Fabric (5%) ($50/kg)	$2,94	$3,58	$3,87
Epoxy, screws, etc.	$9,50	$9,50	$9,50

Table F.2. Direct operational cost (flight) supplementary information for the nanosatellite

Cost Component	UAV A	UAV B	UAV C	ALL UAVs
Hourly rate (engineer) (USD)	$5,88	$5,88	$5,88	$5,88
Flight time (hours)	3,23	3,74	3,56	10,52
preparation and recovery (hours)	6,23	6,74	6,56	19,52
tracking and monitoring (hours)	3,56	4,07	3,89	11,52
Total manhour (3 engineers) (hours)	13,01	14,55	14,01	41,57
Total program manhour, 122 flights per UAV (hours)	1587,02	1775,51	1708,81	5071,34
Total manhour cost, 122 flights per UAV (USD)	$9.331,66	$10.439,98	$10.047,82	$29.819,45

Table F.3. Direct operational cost (maintenance) supplementary information for the nanosatellite

Cost Component	UAV A	UAV B	UAV C	ALL UAVs
Hourly rate (engineer) (USD)	$5,88	$5,88	$5,88	$5,88
Maintenance time (hours)	2	2	2	2
52 weeks in a year (USD)	$611,52	$611,52	$611,52	$611,52
1% material cost per flight (USD)	$2,20	$2,66	$2,86	$7,72
Total cost 122 flights per UAV (USD)	$268,45	$324,44	$349,31	$942,20
Value to calculate component cost (USD)	$879,97	$935,96	$960,83	$2.776,76
10% component cost (USD)	$88,00	$93,60	$96,08	$277,68
TOTAL	$967,97	$1.029,55	$1.056,91	$3.054,43